

STUDY OF THE RARE DECAY  $K_L \longrightarrow \pi^0 \gamma \gamma$  AT KTEV

by

Jianbo Wang

---

A Dissertation Submitted to the Faculty of the  
DEPARTMENT OF PHYSICS  
In Partial Fulfillment of the Requirements  
For the Degree of  
DOCTOR OF PHILOSOPHY  
In the Graduate College  
THE UNIVERSITY OF ARIZONA

2 0 0 7

THE UNIVERSITY OF ARIZONA  
GRADUATE COLLEGE

As members of the Dissertation Committee, we certify that we have read the dissertation  
prepared by Jianbo Wang

entitled STUDY OF THE RARE DECAY  $K_L \rightarrow \pi^0 \gamma \gamma$  AT KTEV

and recommend that it be accepted as fulfilling the dissertation requirement for the  
Degree of Doctor of Philosophy

\_\_\_\_\_  
Dissertation Director: Elliott Cheu      Date: August 6, 2007

\_\_\_\_\_  
Committee Member: Michael Shupe      Date: August 6, 2007

\_\_\_\_\_  
Committee Member: Li-Zhi Fang      Date: August 6, 2007

\_\_\_\_\_  
Committee Member: Robert Thews      Date: August 6, 2007

Final approval and acceptance of this dissertation is contingent upon the candidate's  
submission of the final copies of the dissertation to the Graduate College.

I hereby certify that I have read this dissertation prepared under my direction and  
recommend that it be accepted as fulfilling the dissertation requirement.

\_\_\_\_\_  
Dissertation Director: Elliott Cheu      Date: August 6, 2007

## STATEMENT BY AUTHOR

This dissertation has been submitted in partial fulfillment of requirements for an advanced degree at The University of Arizona and is deposited in the University Library to be made available to borrowers under rules of the Library.

Brief quotations from this dissertation are allowable without special permission, provided that accurate acknowledgment of source is made. Requests for permission for extended quotation from or reproduction of this manuscript in whole or in part may be granted by the head of the major department or the Dean of the Graduate College when in his or her judgment the proposed use of the material is in the interests of scholarship. In all other instances, however, permission must be obtained from the author.

SIGNED: \_\_\_\_\_

Jianbo Wang

## ACKNOWLEDGEMENTS

Once a teacher, forever a teacher. –A Chinese proverb. During the eleven years' study, not only physics, but also much more than that I learn from my adviser, Elliott Cheu. We talked about life, work, and family. You are a good adviser, a good listener, a good helper, a good friend. In the recent six years, meeting once a week is not just time consuming, but patience, support, help, encouragement. Besides thanks, I should give respect to you.

Dr. Shupe, my committee member, a graduate director, gave me the opportunity to come to UA, spent time for my oral exam. In my impression, I always get a satisfied answer when I turn to you. I will never forget that. Thank you, Dr. Fang, Dr. Thews, Iris, Lisa, and Bryan! Thank you, UA EEPP group.

I was lucky to work for the KTeV. Friendly, knowledgeable, cooperative, diligent, that's KTeV. I give thanks to Bob.T, Bob.H, Ed, Peter, Elizabeth, Sasha.G, Rick.K, Wah, Bruce, Julie, Pat, Leo and many others who graduated or left KTeV already. Sydney and Jason may not see this, still I appreciate their help.

If a study or a life is just a task or to reach a goal, then it turns to be a burden. If it is a training, then nothing is meaningless. We may not understand the meaning in the training, but sooner or later, we will see. We may not enjoy things in the training, someday we will see all the things work together to make us good, not what we have but what we are being. That's what I have learned and what I am learning.

My parents, Yongqun and Jinyue, always give me their solid support. Their encouragement, their prayer are with me all the time. Thank you!

In eleven years, how much family time I own my family? How much fun and love you give to me? Countless. Thank you, my family, my wife, Hui Yuan, my daughter Martha and my son Joseph. Your love supports me. Those precious days not just made me feel warm, but gave me the opportunity to show my love to you.

Finally, most of all, how can a person sleep five to six hours, occasionally three hours daily for six years? who is my shepherd? who gives me the strength, who protects me, who guides me, who forms me? My thanks and praise to You.

## TABLE OF CONTENTS

LIST OF FIGURES . . . . .	8
LIST OF TABLES . . . . .	12
ABSTRACT . . . . .	13
CHAPTER 1 INTRODUCTION . . . . .	14
1.1 Search for CP violation in $K^0$ decay . . . . .	14
1.2 The decay $K_L \longrightarrow \pi^0 \gamma \gamma$ . . . . .	17
1.3 Measurements of $K_L \longrightarrow \pi^0 \gamma \gamma$ . . . . .	19
1.4 Overview of this dissertation . . . . .	20
CHAPTER 2 EXPERIMENT . . . . .	21
2.1 Overview . . . . .	21
2.2 Detector . . . . .	22
2.2.1 Drift chamber . . . . .	25
2.2.2 CsI . . . . .	26
2.2.3 Photon vetoes . . . . .	28
2.2.4 The regenerator . . . . .	30
2.2.5 Other detectors . . . . .	31
2.3 Trigger . . . . .	32
2.3.1 Level 1 trigger . . . . .	33
2.3.2 Level 2 trigger . . . . .	33
2.3.3 Level 3 trigger . . . . .	34
2.4 Hardware cluster counter . . . . .	35
2.4.1 HCC algorithm . . . . .	36
2.4.2 Online monitor . . . . .	36
2.5 Data acquisition . . . . .	39
2.5.1 AzTEC . . . . .	40
CHAPTER 3 DATA SELECTION AND RECONSTRUCTION . . . . .	45
3.1 Reconstruction overview . . . . .	45
3.2 Data selection . . . . .	46
3.2.1 1996 and 1997 data . . . . .	46
3.2.2 1999 data . . . . .	47
3.3 Clustering . . . . .	48
3.3.1 Hardware clustering . . . . .	49
3.3.2 Software clustering . . . . .	50
3.3.3 Position determination . . . . .	50

3.3.4	Clustering corrections . . . . .	51
3.4	Reconstruction of signal mode $K_L \rightarrow \pi^0 \gamma \gamma$ . . . . .	52
3.5	Reconstruction of $K_L \rightarrow \pi^0 \pi^0$ . . . . .	56
CHAPTER 4 DATA ANALYSIS . . . . .		57
4.1	Data quality cuts . . . . .	57
4.2	The drift chamber in-time hit (NHIT) cut . . . . .	58
4.3	Vacuum windows cut . . . . .	60
4.4	The ellipse cut . . . . .	60
4.5	Calorimeter cuts . . . . .	64
4.6	Z vertex cut . . . . .	66
4.7	The photon veto cuts . . . . .	67
4.8	The fusion shape $\chi^2$ cut . . . . .	71
4.9	Estimation of the background level . . . . .	74
4.10	Final data sample . . . . .	82
CHAPTER 5 MONTE CARLO SIMULATION . . . . .		87
5.1	General monte carlo simulation . . . . .	87
5.2	The simulation of the CsI calorimeter . . . . .	88
5.3	Trigger simulation . . . . .	90
5.4	Accidental overlay . . . . .	90
5.5	$K_L \rightarrow \pi^0 \gamma \gamma$ Monte Carlo . . . . .	91
5.6	Simulation of the fusion $\chi^2$ variable . . . . .	94
5.7	Data shower library . . . . .	97
5.8	Verification of the data shower library . . . . .	98
CHAPTER 6 BRANCHING RATIO RESULT AND $a_V$ FIT . . . . .		101
6.1	$K_L \rightarrow \pi^0 \gamma \gamma$ branching ratio . . . . .	101
6.2	Estimate of the systematic uncertainties on the branching ratio . . . . .	102
6.2.1	Reweighting to study the systematic errors . . . . .	103
6.2.2	The kaon energy . . . . .	105
6.2.3	Vertex position . . . . .	105
6.2.4	Photon veto cut . . . . .	107
6.2.5	The drift chamber in-time hits (NHIT) . . . . .	108
6.2.6	Shape $\chi^2$ . . . . .	110
6.2.7	Error from estimation of background . . . . .	112
6.2.8	Relative normalization using the shape $\chi^2$ . . . . .	112
6.2.9	Absolute normalization . . . . .	114
6.2.10	Second relative normalization check . . . . .	115
6.2.11	Using the $M_{\pi^0}$ to check our methods . . . . .	115

6.2.12	From $a_V$ . . . . .	116
6.2.13	From the MC acceptance ratio . . . . .	116
6.2.14	Summary . . . . .	118
6.3	Determination of $a_V$ . . . . .	119
6.3.1	Testing the fitter . . . . .	119
6.3.2	Fitting $a_V$ . . . . .	120
6.3.3	Systematic error study . . . . .	122
6.4	Summary . . . . .	127
CHAPTER 7 CONCLUSION . . . . .		128
REFERENCES . . . . .		131

## LIST OF FIGURES

2.1	The schematic of the collimator system. . . . .	22
2.2	Top view of KTeV E832 detector . . . . .	23
2.3	Drift chamber wire . . . . .	24
2.4	CsI detector. The center region consists of $2.5\text{ cm} \times 2.5\text{ cm}$ small blocks, the outer region consists of $5\text{ cm} \times 5\text{ cm}$ big blocks. There are 3100 CsI crystal blocks in total. . . . .	27
2.5	E/p for electron in $K_{e3}$ where E denotes an energy measured at the calorimeter, and p represents a momentum measured by a spectrometer. . . . .	29
2.6	Ring Counter . . . . .	29
2.7	Using $2 \times 2$ array block to calculate the cluster number. This algorithm can implement processing the finding cluster parallel. . . . .	37
2.8	The online monitor of the HCC inefficiency. The strips indicate the hardware failure. . . . .	38
2.9	Timing diagram for CTI state machine 1. Width of busy is 400 ns. . . . .	41
2.10	Timing diagram for CTI state machine 2. Timing elapsed between REN and WST is 175 ns (it takes 125 ns for a word to show up on the data line from the FIFO). Width of WST is 50 ns, and WST period is 100 ns. Width of All_Done is 100 ns . . . . .	42
3.1	The $\gamma\gamma$ invariant mass distribution from data after all cuts. The normalization mode ( $K_L \rightarrow \pi^0\pi^0$ ) is indicated by the two solid vertical lines, and the $\pi^0\gamma\gamma$ candidates are marked by the arrow and the dashed lines. . . . .	54
3.2	An event display for a $K_L \rightarrow \pi^0\gamma\gamma$ candidate. The top display shows the response of the calorimeter to the four photons. The bottom display shows an $x$ view of the whole detector with the reconstructed paths of each of the four photons. The four photons are neutral, so they are not deflected when traversing the analysis magnet. . . . .	55
4.1	The number of in-time drift chamber hits for $2\pi^0$ data (dot) and Monte Carlo (histogram). The second plot is the ratio of the data over the Monte Carlo and shows a slight slope. There are also a number of small peaks in the data that correspond to tracks. A single track produces 16 hits in the drift chamber system. . . . .	59
4.2	Mass versus decay position for four cluster events. Enhancements at the $\eta$ and $\pi^0$ mass are evident. . . . .	61
4.3	$M_{\pi^0}$ versus $M_{\gamma\gamma}$ , top: the second best $\pi^0$ combination, bottom: the third best $\pi^0$ combination . . . . .	62
4.4	$M_{\gamma\gamma}$ for $2\pi^0$ after all cuts . . . . .	63

4.5	The comparison of the center of energy data to Monte Carlo for $3\pi^0$ events . . . . .	65
4.6	The decay vertex for all events and $2\pi^0$ (green). Two vertical lines indicate the position of the cuts. . . . .	66
4.7	The Monte Carlo reconstructed Z vertex. a) $\pi^0\gamma\gamma$ , b) $3\pi^0$ single fusion and c) $3\pi^0$ double fusion. Vertical lines and arrows show the accepted region. This cut rejects most of the $3\pi^0$ single fusion events. The arrows indicate the accepted region. . . . .	67
4.8	The photon veto cuts. The upper plot shows the energy in the Mask Anti, and the lower plot shows the minimum energy in any of the ring counters. The ring counters include ERC6, ERC7, ERC8, ERC9 and ERC10. The solid histogram is from $2\pi^0$ events, and the dashed histogram is the scaled $3\pi^0$ distribution. The vertical line indicates the position of the cut. The arrows indicate the accepted region. . . . .	68
4.9	The energy in the photon vetoes. The upper plot is minimum energy in the Spectrometer Anti and CsI Anti, while the lower plot shows the Collar Anti. The Spectrometer Anti includes SA2, SA3, and SA4. The solid histogram is for $2\pi^0$ events, and the dashed histogram is for the scaled $3\pi^0$ distribution. The vertical line indicates the accepted region. . . . .	69
4.10	The energy in the BAs. The solid histogram is from $2\pi^0$ events, and the dashed histogram is from scaled $3\pi^0$ distribution. The vertical line indicates the position of the cut. The arrows indicate the accepted region. . . . .	70
4.11	a) The two-photon invariant mass, $M_{\gamma\gamma}$ after all cuts except for the photon shape cut. The dots are the combined 1996 and 1997 data and the histogram is the combined $2\pi^0$ and $3\pi^0$ Monte Carlo. b) The two-photon invariant mass, $M_{\gamma\gamma}$ after all cuts except for the photon shape cut. The solid histogram represents the data. The dashed histogram is the Monte Carlo contribution from double fusions, the dotted histogram is from single fusions and the dot-dash histogram is from no-fusion events. . . . .	72
4.12	The fusion $\chi^2$ variable for all events (histogram) and for the events outside the $2\pi^0$ mass region (dashed). The variable is cut at 1.8. Vertical lines and arrows show the accepted region. . . . .	73
4.13	$M_{\pi^0}$ and $M_{\gamma\gamma}$ distributions for single and double fusion $3\pi^0$ Monte Carlo events. The left plots are from double fusion, and the right side is the single fusion. The top 4 plots are $M_{\pi^0}$ distribution, and the bottom 4 plots are $M_{\gamma\gamma}$ . Plot e) shows that double fusion events with the correct combination (2 photons are from the same $\pi^0$ in the event reconstruction) do not contribute to the low mass tail of $M_{\gamma\gamma}$ . . . . .	75
4.14	$M_{\pi^0}$ distribution after all cuts. The dots are data. The solid histogram is $3\pi^0$ and $\pi^0\gamma\gamma$ Monte Carlo, the dashed histogram (red) is $3\pi^0$ background MC. Vertical lines and arrows show the accepted region. . . . .	76

4.15	$M_{\pi^0}$ distribution of low mass tail, the histogram is $3\pi^0$ plus $\pi^0\gamma\gamma$ MC, the dots are the data, the dash line is the $3\pi^0$ background. a) default $3\pi^0$ b) separate single fusion and double fusion. . . . .	78
4.16	Final $M_{\gamma\gamma}$ distribution after all cuts applied. The dot is data, the histogram is $\pi^0\gamma\gamma$ and $3\pi^0$ MC. The dash line is $3\pi^0$ background MC. The background at the tail part is very high. . . . .	80
4.17	Y dalitz after all cuts. The dots are the data. The solid histogram is the sum of the $3\pi^0$ and $\pi^0\gamma\gamma$ Monte Carlo, the dark histogram (red) is $3\pi^0$ background MC . . . . .	81
4.18	The comparison of 96+97 data to Monte Carlo. The plot shows $2\pi^0$ Z decay vertex, kaon energy, $\pi^0$ mass, and shape $\chi^2$ Data/MC overlay. The right side plots are the two histograms ratio. The dot is data, and the histogram is $2\pi^0$ MC. . . . .	83
4.19	The comparison of 99 data to Monte Carlo. The plot shows $2\pi^0$ Z decay vertex, kaon energy, $\pi^0$ mass, and shape $\chi^2$ Data/MC overlay. The right side plots are the two histograms ratio. The dot is data, and the histogram is $2\pi^0$ MC. . . . .	84
4.20	The comparison of 96 +97 data to Monte Carlo. The plot shows $2\pi^0$ photon energy, x illumination y illumination Data/MC overlay. The right side plots are the two histograms ratio. The dot is data, and the histogram is $2\pi^0$ MC. . . . .	85
4.21	The comparison of 99 data to Monte Carlo. The plot shows $2\pi^0$ photon energy, x illumination y illumination Data/MC overlay. The right side plots are the two histograms ratio. The dot is data, and the histogram is $2\pi^0$ MC. . . . .	86
5.1	ChPT prediction of the $M_{\gamma\gamma}$ distribution. . . . .	92
5.2	The fusion $\chi^2$ variable after cuts. The dots are the data and the histogram is the $3\pi^0$ Monte Carlo. the insert shows the same distribution for the low mass tail of $M_{\gamma\gamma} < 0.240\text{GeV}/c^2$ . . . . .	95
5.3	Data to MC comparison of fusion $\chi^2$ for the data from 1999. the upper is with The default shower library was used from Monte Carlo in the upper plot, while the data shower library was used for the lower. . . . .	96
5.4	The shape $\chi^2$ distribution. a) The solid histogram is the data, the dashed histogram is the $K_L \rightarrow \pi^0\pi^0\pi^0$ Monte Carlo calculated using the data shower library, and the dotted histogram the $K_L \rightarrow \pi^0\pi^0\pi^0$ Monte Carlo using the reweighted default shower library. b) The same histogram as above except that the dotted histogram is the $K_L \rightarrow \pi^0\pi^0\pi^0$ Monte Carlo using the unweighted default shower library. . . . .	100
6.1	The reweighted kaon energy compared to data. The upper plots are not reweighted, after the variable is reweighted to data, the acceptance difference is calculated and counted as the systematic error. .	106

6.2	The unweighted Z decay vertex compared to data. After the variable is reweighted to data, the acceptance difference is calculated and counted as the systematic error. . . . .	107
6.3	The variable EMA of Monte Carlo compared to data. The variable is not reweighted, after the variable is reweighted to data, the acceptance difference is calculated and counted as the systematic error. . .	108
6.4	The comparison of ERC data to MC. The ERC includes ERC6, ERC7, ERC8, ERC9, and ERC10. The variable is not reweighted, after the variable is reweighted to data, the acceptance difference is calculated and counted as the systematic error. . . . .	109
6.5	The comparison of the drift chamber in-time hit data to MC. The variable is not reweighted, after the variable is reweighted to data, the acceptance difference is calculated and counted as the systematic error. . . . .	109
6.6	The reweighted fusion shape $\chi^2$ compared to data. The upper plots are not reweighted, after the variable is reweighted to data, the acceptance difference is calculated and counted as the systematic error. . . . .	111
6.7	This plot shows the $3\pi^0$ single fusion and double fusion fusion $\chi^2$ separately. In the range of 5-20 which is marked as normalization region, the number of the double fusion 6.5 times as much as the number of the single fusion. But in the low value region (0-2.0), the number of the single fusion is comparable to that of the double fusion. . . . .	113
6.8	The explanation of the relative normalization method. In fusion shape $\chi^2$ distribution, within the range of 5-20 are mostly $3\pi^0$ events. The uncertainty of this method is that the proportion of the single fusion and the double fusion may be different in data, and most of $3\pi^0$ fusion $\chi^2$ in the range of 5-20 are double fusion. . . . .	114
6.9	The ratio of the acceptance of $2\pi^0$ and of $\pi^0\gamma\gamma$ varies with $a_V$ . . .	117
6.10	The difference between the fitted and true $a_V$ divided by the true $a_V$ (left) and the reconstructed $a_V$ (right) for 142 Monte Carlo samples. The top plots are for $a_V = -0.65$ and the bottom plots are for $a_V = -0.31$ . The measured results are $a_V = -0.302$ and $a_V = -0.661$ respectively. The standard deviations are $1\sigma$ . . . . .	121
6.11	$a_V$ systematic study on the Z decay vertex . . . . .	123
6.12	$a_V$ systematic study on fusion $\chi^2$ . . . . .	124
6.13	$M_{\gamma\gamma}$ data MC overlay. The dot is DATA, the blank histogram is MC $3\pi^0$ and $\pi^0\gamma\gamma$ , the red histogram is $3\pi^0$ background. a) Using default $3\pi^0$ MC b) separate single and double fusion . . . . .	125
6.14	Using the background from Figure 6.13, a second-order polynomial fit provides $a_V = -0.32$ . . . . .	126
6.15	Using the background from Figure 6.13, a third-order polynomial fit provides $a_V = -0.34$ . . . . .	126
7.1	Comparison of results with KTeV 99 PRL and NA48 a) branching ratio and b) measured $a_V$ . . . . .	129

## LIST OF TABLES

2.1	An example of Level 3 filter cut for 1997 and 1999 run . . . . .	35
2.2	CTI data format . . . . .	41
2.3	CAMAC command . . . . .	42
3.1	1999 strip cuts . . . . .	48
3.2	Clustering unpack bit mask . . . . .	49
4.1	Comparison of $2\pi^0$ and $3\pi^0$ acceptance with each cut . . . . .	77
4.2	$K_L \rightarrow \pi^0\gamma\gamma$ Efficiencies . . . . .	79
6.1	Values used in branching ratio calculation . . . . .	102
6.2	List the variables of which the cut acceptance is below 90% . . . . .	104
6.3	Branching ratio systematic uncertainties . . . . .	118
6.4	$a_V$ fitting systematic uncertainty . . . . .	127

# ABSTRACT

We study on the rare decay  $K_L \rightarrow \pi^0 \gamma \gamma$ , measure  $a_V$ , and branching ratio by analysing 96, 97 and 99 data. The measurements were taken by KTeV at Fermi National Accelerator Laboratory. After all cuts, we have 1982  $K_L \rightarrow \pi^0 \gamma \gamma$  candidate. The background level is estimated as 30%.  $K_L \rightarrow \pi^0 \gamma \gamma$  branching ratio is measured as

$$(1.29 \pm 0.03(stat) \pm 0.04(sys)) \times 10^{-6}$$

By using D'Ambrosio's theory to fit  $a_V$ ,

$$a_V = -(-0.31 \pm 0.05(stat) \pm 0.07(sys))$$

## CHAPTER 1

### INTRODUCTION

#### 1.1 Search for CP violation in $K^0$ decay

Every symmetry of nature produces a conservation law. The search for symmetries in the particle physics helped people to understand more about elementary particles. There are three discrete symmetries : parity (P), charge conjugation (C), and time reversal (T). The operation of parity on a system changes the sign of all spatial coordinates. Parity is conserved if a process and its mirror image process behave the same. The operation of the charge operator on a particle changes it into its antiparticle. Symmetry under charge conjugation implies that a process and its charge conjugate process are the same. The effect of the time reversal operator causes a process to run backwards in time. If the rate for a time-reversed process is the same as that of the original process, that process conserves T.

Parity violation can be observed in pion decay

$$\pi^+ \rightarrow \mu^+ + \nu_\mu. \quad (1.1)$$

The spin vector  $\sigma$  and the momentum vector  $p$  define a handedness. Under parity the spin vector remains the same, while the momentum vector changes sign. So, we expect a left-handed neutrino to change into right-handed neutrino under parity transformation. However, in nature, only left-handed neutrinos (and right-handed

anti-neutrinos) are found, resulting in maximal parity violation in weak decays.

$C$  invariance is also broken in the weak interactions. As in the pion decay discussed above, under charge-conjugation one would expect that the charge conjugate decay would occur with the left-handed neutrino transformed into a left-handed anti-neutrino.

$$\pi^- \rightarrow \mu^- + \bar{\nu}_\mu \quad (1.2)$$

Again, we only find right-handed anti-neutrinos, and so charge is also maximally violated in weak decays.

Although the weak interactions are not eigenstates of the individual  $C$  and  $P$  operators, weak decays would appear to be invariant under the combined operation of  $C$  and  $P$ . Applying the combined  $CP$  operator to a left-handed neutrino transforms the particle into a right-handed anti-neutrino. The combined operation  $CP$  was assumed conserved until 1964 when Cronin and Fitch discovered  $CP$  violation in kaon decay.

The  $K^0$  and  $\bar{K}^0$  are not eigenstate of the  $CP$  operator. As one can see.

$$CP|K^0\rangle = |\bar{K}^0\rangle \quad (1.3)$$

$$CP|\bar{K}^0\rangle = |K^0\rangle \quad (1.4)$$

$CP$  eigenstates  $K_1$  and  $K_2$  can be formed from the combination of  $K^0$  and  $\bar{K}^0$ .

$$\begin{aligned} |K_1\rangle &= \frac{1}{\sqrt{2}} (|K^0\rangle + |\bar{K}^0\rangle) \\ |K_2\rangle &= \frac{1}{\sqrt{2}} (|K^0\rangle - |\bar{K}^0\rangle) . \end{aligned} \quad (1.5)$$

The  $K_1$  is  $CP$  even while the  $K_2$  is  $CP$  odd.

The neutral kaon can decay to both  $2\pi^0$  and  $3\pi^0$ . The  $2\pi^0$  final state is CP even, while the  $3\pi^0$  final state is CP odd. If CP is conserved, the  $K_2$  should decay to three neutral pions, and the  $K_1$  should produce  $2\pi^0$ . Because of the allowed phase space, the  $K_1$  has a much shorter lifetime than the  $K_2$ . The  $K_1$  lifetime is  $0.87 \times 10^{-10}$  s, and  $K_2$  lifetime is  $0.53 \times 10^{-7}$  s. Therefore, evidence that  $K_L$  decays to two pions would indicate that CP is violated. In 1964, Cronin, Fitch [1] found decays of  $K_L$  to two pions, and as a result C is violated in neutral kaon decays. The  $K_L$  can be described as a superposition of  $K_1$  and  $K_2$ .

$$\begin{aligned} |K_S\rangle &= \frac{1}{\sqrt{1+|\epsilon|^2}} (|K_1\rangle + \epsilon|K_2\rangle) \\ |K_L\rangle &= \frac{1}{\sqrt{1+|\epsilon|^2}} (|K_2\rangle + \epsilon|K_1\rangle). \end{aligned} \quad (1.6)$$

where  $\epsilon$  is of order  $2 \times 10^{-3}$ . The fact that  $\epsilon \neq 0$  means that the  $K_L$  contains a small admixture of the wrong CP. The weak eigenstates are not eigenstates of CP. This is called CP violation through mixing, or indirect CP violation.

Substituting Equation 1.5 into Equation 1.6, we obtain

$$\begin{aligned} |K_S\rangle &= \frac{1}{\sqrt{2(1+|\epsilon|^2)}} \left[ (1+\epsilon)|K^0\rangle + (1-\epsilon)|\overline{K^0}\rangle \right] \\ |K_L\rangle &= \frac{1}{\sqrt{2(1+|\epsilon|^2)}} \left[ (1+\epsilon)|K^0\rangle - (1-\epsilon)|\overline{K^0}\rangle \right]. \end{aligned} \quad (1.7)$$

Equation 1.7 shows what CP violation means in nature: matter and anti-matter are treated differently.

Since the finding of indirect CP-violation, people have searched for evidence of direct CP-violation. If direct CP violation exists, one would expect to observe  $K_2$  decaying directly into  $2\pi^0$ . The search for direct CP violation was the main goal of the E832 KTeV experiment.

## 1.2 The decay $K_L \longrightarrow \pi^0 \gamma \gamma$

The decay of  $K_L \longrightarrow \pi^0 \gamma \gamma$  is special because it is an important step in understanding CP violation in  $K_L \rightarrow \pi^0 e^+ e^-$ . In  $K_L \rightarrow \pi^0 e^+ e^-$ , the CP violating contribution is expected to be greater than CP conserving contribution. Observation of this decay would lead to the first measurement of direct CP violation in a decay.

There are three contributions to  $K_L \rightarrow \pi^0 e^+ e^-$

$$BR(K_L \rightarrow \pi^0 e^+ e^-) = 5 \times 10^{-12}, \quad (\text{Direct CP violation}) \quad (1.8)$$

$$BR(K_S \rightarrow \pi^0 e^+ e^-) = (1 - 5) \times 10^{-12}, \quad (\text{Indirect CP violation}) \quad (1.9)$$

$$BR(K_L \rightarrow \pi^0 e^+ e^-) \approx 10^{-13}, \quad (\text{CP conserving}) \quad (1.10)$$

To determine the direct CP violating component, it is important to understand the contributions from the CP conserving and indirect CP violating terms. The decay  $K_S \rightarrow \pi^0 \gamma \gamma$  can be used to understand the indirect CP violating piece. And, the decay  $K_L \longrightarrow \pi^0 \gamma \gamma$  can be used to understand the CP conserving amplitude. In chiral perturbation theory (ChPT), the  $O(p^4)$   $K_L \longrightarrow \pi^0 \gamma \gamma$  contributions to  $K_L \rightarrow \pi^0 e^+ e^-$  are helicity suppressed. This led people to believe that the CP conserving contributions to  $K_L \rightarrow \pi^0 e^+ e^-$  could be ignored. However, after further examination of the  $K_L \longrightarrow \pi^0 \gamma \gamma$  decay, many realized that vector meson exchange contributions could be large, and could increase the CP conserving contributions to  $K_L \rightarrow \pi^0 e^+ e^-$ . Therefore, to study CP violation in  $K_L \rightarrow \pi^0 e^+ e^-$ , measurements of  $K_L \rightarrow \pi^0 \gamma \gamma$  are important.

ChPT is a low energy expansion of QCD. At low energies (usually  $E \ll 1\text{GeV}$ ), it is difficult for QCD to describe hadronic interactions. Because the interactions among

the pseudoscalar mesons are weak at low energy, QCD can be treated in a perturbative way. Thus one can expand the QCD Lagrangian at low energy, breaking chiral symmetry. The lowest order prediction by ChPT is called the one-loop model. In this model  $K_L \longrightarrow \pi^0 \gamma \gamma$  proceeds through the intermediate state  $\pi^0 \pi^+ \pi^-$ , with the  $\pi^+ \pi^-$  coupling to  $\gamma \gamma$ . This lowest order model is known as  $O(p^4)$ . The predictions for the  $K_L \longrightarrow \pi^0 \gamma \gamma$  decay are free from arbitrary parameters and provide a good test of the ChPT. The one-loop level contributes  $0.68 \times 10^{-6}$  to the branching ratio [5]. The first measurements of  $K_L \longrightarrow \pi^0 \gamma \gamma$  observed the branching ratio to be 2-3 times bigger than the theory prediction [10][11]. In 1989, L.M.Sehgal proposed the vector meson dominance (VMD) theory. It extended the theory to  $O(p^6)$ . This theory predicted the  $K_L \longrightarrow \pi^0 \gamma \gamma$  branching ratio to be in the range  $1.79\text{-}3.9 \times 10^{-6}$ . But the predictions of the Dalitz variables from this model did not match the experiment observations. In 1990, G.Ecker added vector meson exchange terms to the one-loop model, and calculated the interference between  $O(p^4)$  and  $O(p^6)$ . The addition of the vector meson exchange contributions gives a better prediction of the branching ratio. These contribution can be parametrized by  $a_V$ . L.Cappiello and D'Ambrosio discussed the correction to  $K_L \longrightarrow \pi^0 \gamma \gamma$  from  $K_L \rightarrow 3\pi^0$ . This contribution increases the branching ratio by 30%. Then Heiliger, Cohen explained the  $K_L \longrightarrow \pi^0 \gamma \gamma$  branching ratio through vector-meson exchange and the introduction unitarity corrections at  $O(p^6)$  [3] [7].

The calculated amplitude of Ecker, Pich, and Rafael [3] is:

$$\begin{aligned}
 A(K(p) \rightarrow \pi(p')\gamma(q_1)\gamma(q_2)) = & \epsilon_\mu(q_1)\epsilon_\nu(q_2)\left[\frac{A(y,z)}{M_K^2}(q_2^\mu q_1^\nu - q_1 q_2 g^{\mu\nu}) \right. \\
 & \left. + \frac{2B(y,z)}{M_K^4}(-pq_1 p q_2 g^{\mu\nu} - q_1 q_2 p^\mu p^\nu + p q_1 q_2^\nu p^\nu + p q_2 p^\mu q_1^\nu)\right] \quad (1.11)
 \end{aligned}$$

the Dalitz variables are

$$y = |p(q_1 - q_2)|/M_K^2, z = (q_1 + q_2)^2/M_K^2, \quad (1.12)$$

with the dimensionless variables A and B:

$$A = \frac{G_8 M_K^2 \alpha}{\pi} \left[ F\left(\frac{z}{r_\pi^2}\right) \left(1 - \frac{r_\pi^2}{z}\right) + F(Z) \left(\frac{1 + r_\pi^2}{z} - 1\right) + a_V(3 - z + r_\pi^2) \right]$$

$$B = -2a_V \frac{G_8 M_K^2 \alpha}{\pi}, r_\pi = \frac{M_\pi}{M_K} \quad (1.13)$$

Here  $q_i$  and  $p$  are the momenta of the photons and the pion, respectively. The loop function  $F(z)$  is defined in reference[5] and is approaching  $-z/12$  when  $z$  is approaching zero. The contribution from vector meson exchange is characterized by  $a_V$ .

### 1.3 Measurements of $K_L \longrightarrow \pi^0 \gamma \gamma$

There have been a number of previous measurements of  $K_L \longrightarrow \pi^0 \gamma \gamma$ . In 1989, FNAL-E731 published the first limit on  $K_L \longrightarrow \pi^0 \gamma \gamma$  [10]

$$\text{B}(K_L \longrightarrow \pi^0 \gamma \gamma) < 2.7 \times 10^{-6} \quad (1.14)$$

Soon after, the NA31 experiment CERN-NA31 published the first observation of this decay[11].

$$\text{B}(K_L \longrightarrow \pi^0 \gamma \gamma, M_{\gamma\gamma} > 0.280 \text{ GeV}) = (2.1 \pm 0.6) \times 10^{-6} \quad (1.15)$$

This result was soon confirmed by the E731 experiment in 1991[12]:

$$\frac{\Gamma(K_L \longrightarrow \pi^0 \gamma \gamma, M_{\gamma\gamma} > 0.280 \text{ GeV})}{\Gamma(K_L \longrightarrow \text{all})} = (1.86 \pm 0.60 \pm 0.60) \times 10^{-6} \quad (1.16)$$

An improved measurement from NA31 resulted in the following result [13]

$$B(K_L \longrightarrow \pi^0 \gamma \gamma) = (1.7 \pm 0.3) \times 10^{-6} \quad (1.17)$$

In 1999 a new Fermilab experiment, KTeV, measured the  $K_L \longrightarrow \pi^0 \gamma \gamma$  decay. This result was a significant improvement over the previous results. The KTeV experiment published a new result with 881  $K_L \longrightarrow \pi^0 \gamma \gamma$  candidates in 1999 [2]:

$$B(K_L \longrightarrow \pi^0 \gamma \gamma) = (1.68 \pm 0.07 \pm 0.08) \times 10^{-6} \quad (1.18)$$

In 2002, the NA48 experiment published their result[14]:

$$B(K_L \longrightarrow \pi^0 \gamma \gamma) = (1.36 \pm 0.03 \pm 0.03 \pm 0.03) \times 10^{-6} \quad (1.19)$$

There is a nearly three sigma difference between the most recent measurements from the NA48 and the KTeV results. This thesis will attempt to resolve the differences between the two results.

## 1.4 Overview of this dissertation

This thesis describes the analysis of decay  $K_L \longrightarrow \pi^0 \gamma \gamma$  based on the KTeV 1996, 1997 and 1999 datasets. Chapter 1 describes the theory and the experiments measurement. Chapter 2 describes the KTeV E832 experiment. Event selection and reconstruction are discussed in chapter 3. Chapter 4 explains the data analysis and the background estimation. MC simulation the acceptance determination are discussed in chapter 5. The branching ratio systematic errors and the determination of  $a_V$  are discussed in chapter 6.

## CHAPTER 2

### EXPERIMENT

#### 2.1 Overview

This measurement was carried out as a part of experiment E832 which was built to measure the direct CP violation parameter  $\Re(\epsilon'/\epsilon)$ . The KTeV experiment was also configured as E799 to study in rare kaon decays. In E832 the two main decays studied are  $K_L \rightarrow \pi^0\pi^0$  and  $K_L \rightarrow \pi^+\pi^-$ . Since  $K_L \rightarrow \pi^0\pi^0$  has a similar topology to  $K_L \rightarrow \pi^0\gamma\gamma$ , the  $K_L \rightarrow \pi^0\gamma\gamma$  data were taken in E832.

Protons are accelerated to 800 GeV in the Fermilab Tevatron during a 19 second “spill”. For 1999 running this spill length was 23 seconds. The spill is followed by a period of 41 (60) seconds of “off-spill” time during the 1997 (1999) running. The spill itself is divided into many buckets, which is determined by a 53 MHz radio frequency (RF). This RF substructure provides the basic timing information. The buckets are separated by 19ns, and protons arrive in a 2 ns period at the beginning of each bucket. The flux of the protons is  $3\text{-}5 \times 10^{12}$  per spill. The 800 GeV proton beam hits the beryllium oxide target with a cross section of 3.0 mm×3.0 mm. The targetting angle is chosen to be 4.8 mrad with respect to the vertical which results in both a high kaon flux and a good kaon to neutron ratio. In order to produce two nearly parallel beams, to remove charged particles and to reduce photons in

the beam, a number of collimators, absorbers, and sweeping magnets are located downstream of the targets. The absorber made of 7.6 cm long lead is placed 18.5 m downstream of the target. The collimator system is shown in Figure 2.1

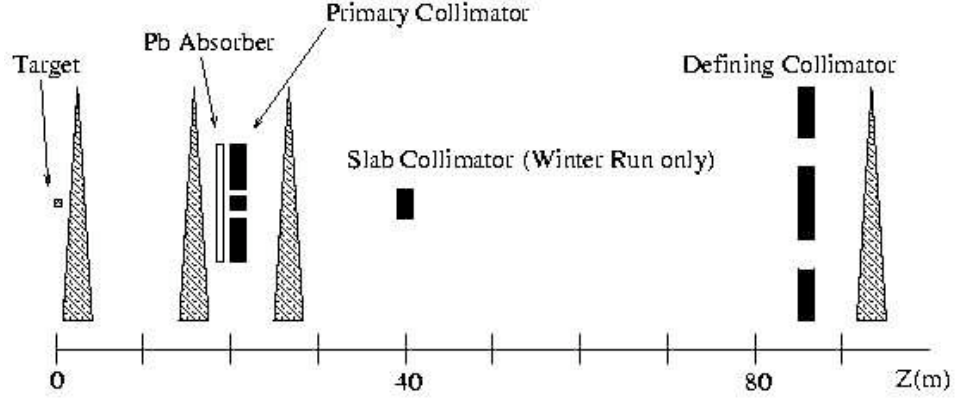


Figure 2.1: The schematic of the collimator system.

The collimator system is used to insure that no neutral particle scattered from the neutral beam itself can hit the calorimeter. The neutral collimation scheme includes a primary collimator and a defining collimator. The primary is 7.6 m downstream from the target, and the defining collimator at 85 m. The combination of the primary and secondary collimators defines the maximum deviation of a scattered neutral particle from beam axis at the z position of the CsI calorimeter.

## 2.2 Detector

Figure 2.2 shows the layout of the E832 detector. A detailed description of the detector can be found KTeV design report (reference [21]) and KTeV  $\epsilon'/\epsilon$  PRD

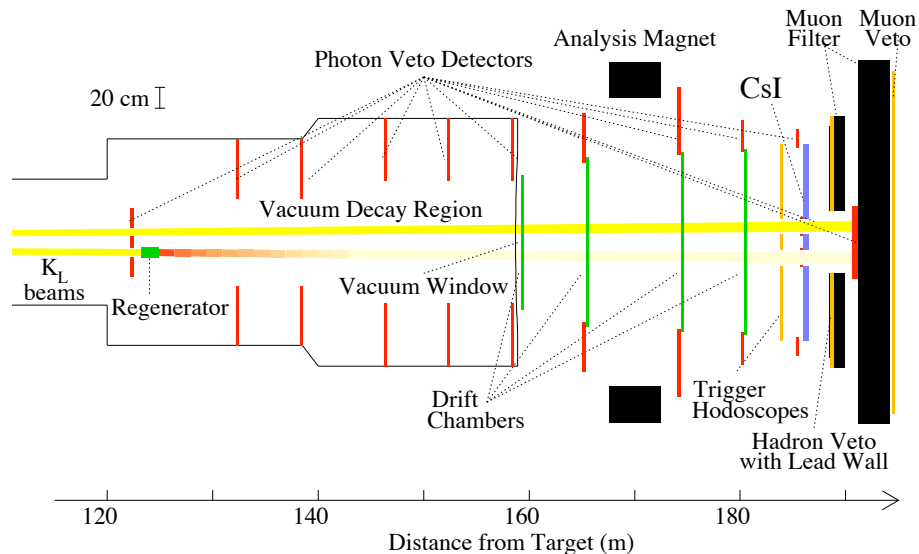


Figure 2.2: Top view of KTeV E832 detector

paper [25]. A regenerator is used to produce a  $K_S$  component in one of the two beams. The regenerator moves back and forth between the two beams after each spill.

The vacuum system starts with a bellows and gate valve where the neutral beam transport vacuum system transitions to the 24 inches diameter upstream vacuum pipe. This pipe expands to 36 inches and to the regenerator vacuum tank. The vacuum system continues with the vacuum vessels downstream of the regenerator tank. It includes the large diffusion pumps and backing pumps, and the lines to the pump-outs for the vacuum vetoes.

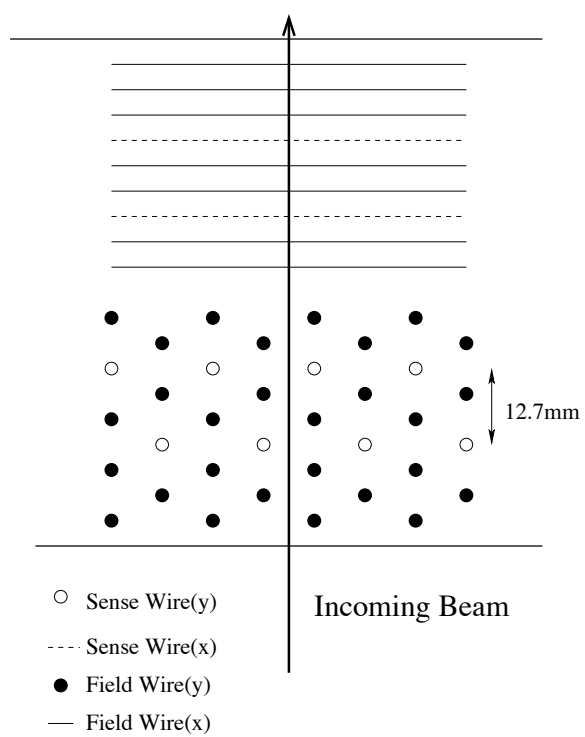


Figure 2.3: Drift chamber wire

### 2.2.1 Drift chamber

The drift chambers are used to reconstruct charged particles. There are 4 drift chambers, two upstream of the analysis magnet, and two downstream of the analysis magnet. The wires in a sense plane are separate by 12.7mm, and both x and y views of each chamber have two sense planes, referred to as  $x(y)$  and  $x'(y')$  plane. Each sense plane is offset from the next by 6.35mm. The configuration of the wires is shown in Fig. 2.3. The field shaping wires are made of 100  $\mu\text{m}$  diameter gold-plated aluminum sense (anode) wires and the sense wires are 25  $\mu\text{m}$  diameter gold-plated tungsten field (cathode) wires. This yields a drift distance of 6.35 mm perpendicular to a wire and results in an unambiguous determination of the side of the wire by which the particle passed. The size of the most upstream chamber(DC1) is 1.3 m  $\times$  1.3 m, and the most downstream drift chamber(DC4) is 1.9 m  $\times$  1.9 m. The gas in the drift chamber is mixture of Argon, Ethane and isopropyl alcohol. Charged particles cause ionization in the gas, producing a current pulse on the sense wires. At 2500V, the velocity of the drifting ions is 50  $\mu\text{m}/\text{ns}$ .

The pulses from the drift chambers are amplified and discriminated in front end cards mounted on the chambers. The discriminated signals with 40 ns width are then sensed by LeCroy 3377 time-to-signal converters(TDC) with a resolution of 0.5ns. The TDCs are operated “in common stop mode” where an incoming pulse will start a TDC channel and a later stop pulse from the first level trigger will stop all triggered channels.

TDC counts in drift chambers are translated in software to a distance from the

sense wire. This position is then used in the reconstruction to determine each tracks trajectory. The position resolution of each chamber is determined by the measurement of a sum of the two drift distance(SOD) in each view.

Between DC2 and DC3, the charged particles are given a transverse momentum kick by a dipole magnet with a vertical field of about 2 kG. The magnetic gap is 2.9 m  $\times$  2.0 m  $\times$  3.1 m. The transverse momentum kick transferred,  $\Delta p_t$ , was typically 0.41 GeV/ $c$ .

The momentum resolution of the drift chamber is

$$\frac{\sigma(P)}{P} = 0.38\% \oplus 0.016\%P \quad (2.1)$$

The first item is caused by the multiple scattering effects, and the second is from finite resolution of measured hit positions within the chambers.

### 2.2.2 CsI

The energies and positions of photons and electrons are determined by the CsI calorimeter located at the downstream end of the KTeV detector. The calorimeter is also useful for all charged tracks since the tracking system is unable to match the  $x$  and  $y$  components of tracks. So, matching of  $x$  and  $y$  tracks is done using information from the CsI calorimeter.

The calorimeter consists of 3100 pure CsI crystals as shown in Fig. 2.4. Each crystal is wrapped with mylar to optically isolate the crystal. The center region of the calorimeter consists of small blocks with a square 2.5cm $\times$ 2.5cm face. The outer area consists of large blocks of size 5cm $\times$ 5cm. The depth of each crystal

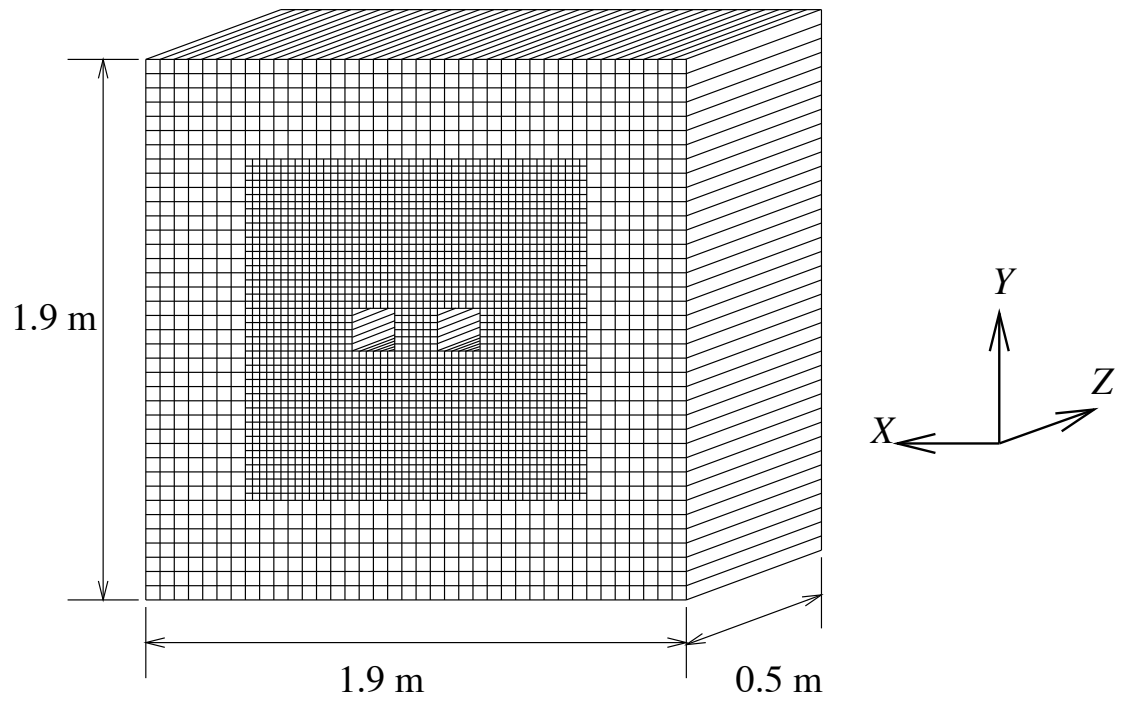


Figure 2.4: CsI detector. The center region consists of  $2.5 \text{ cm} \times 2.5 \text{ cm}$  small blocks, the outer region consists of  $5 \text{ cm} \times 5 \text{ cm}$  big blocks. There are 3100 CsI crystal blocks in total.

is 50cm. The CsI calorimeter has two beam holes to allow the passage of the neutral beams.

There 2232 small blocks ( $2.5 \text{ cm} \times 2.5 \text{ cm}$ ) in the interior region, and 868 large blocks ( $5 \text{ cm} \times 5 \text{ cm}$ ) outside of the small blocks array. The depth of each block is equal to 27 radiation lengths (1.852 cm) to ensure that most showers are contained in the calorimeter. The energy resolution can be formulated as:

$$\frac{\sigma(E)}{E} = 0.45\% \oplus \frac{2\%}{\sqrt{E}} \quad (2.2)$$

The constant term is related to an amalgam effect, for example, light leakage, noise.

The second term is the result of photostatistics of the scintillation light.

The calorimeter readout includes photomultiplier tubes (PMTs) that converts the light from the crystals to analog current pulses, an application-specific integrated circuit which digitizes the PMT current and a bus (VME) system that is used as a buffer. The data will be transferred th DAQ system, analyzed by the online computers and logged to the tapes. Figure 2.5 shows E/p for electron in  $K_{e3}$ . The relativistic electrons are expected to deposit all the energy in the calorimeter, and E/p should be 1. The figure 2.5 also shows the performance of the calorimeter.

### 2.2.3 Photon vetoes

One of the major backgrounds to this analysis comes from  $K_L \rightarrow \pi^0 \pi^0 \pi^0$ . This decay can contribute to the background if one or more of the photons misses the CsI calorimeter. The photon vetoes can reject the  $3\pi^0$  background if at least one of the missing photons hits one of the photon vetoes.

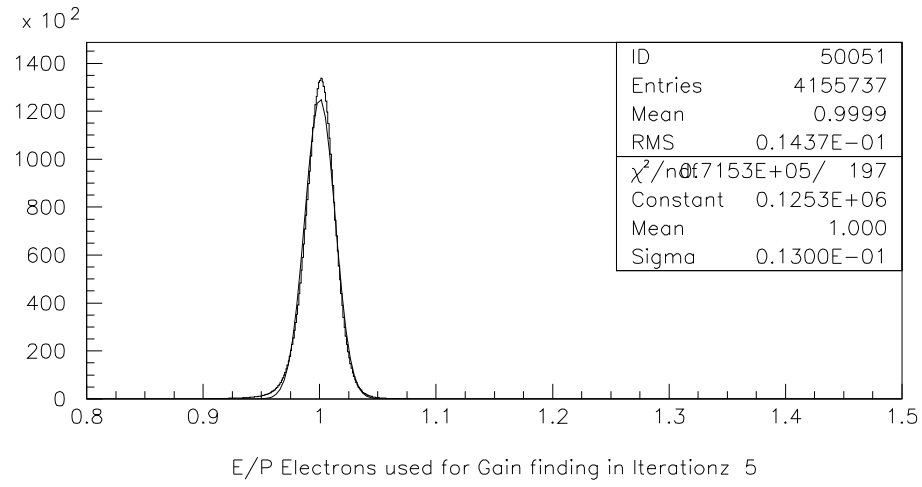


Figure 2.5:  $E/p$  for electron in  $K_{e3}$  where  $E$  denotes an energy measured at the calorimeter, and  $p$  represents a momentum measured by a spectrometer.

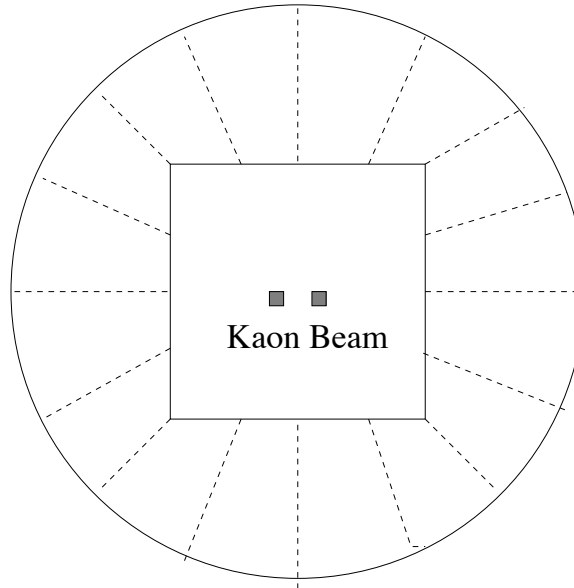


Figure 2.6: Ring Counter

There are 5 ring counters RC6-RC10 located from 130m to 150m along the vacuum decay region. The shape of each ring counter is round outside, with a square inner aperture. A schematic of a ring counter is shown in Fig. 2.6. There are 24 layer scintillator tiles in each ring counter.

Four Spectrometer Antis (SA), are located upstream each of the drift chambers. A CsI Anti (CIA), and the Back Antis (BA) are located downstream of CsI and used to catch the photons that miss the calorimeter. The CIA registers photons that miss the outer edge of the CsI calorimeter, while the BA catches photons that pass through either of the two beam holes. A Collar Anti(CA) is located in front of the CsI calorimeter and around the two beam holes.

#### 2.2.4 The regenerator

The regenerator is composed of a stack of 85 blocks of scintillator. The last block of the regenerator is composed of alternating layers of 5.6 mm of lead and 4 mm of scintillator. The purpose of the regenerator is to produce a source of  $K_S$  decays from one of the two  $K_L$  beams. A  $K_L$  is composed of both  $K^0$  and  $\bar{K}^0$  components. Since the  $K^0$  and  $\bar{K}^0$  interact differently with matter, the fraction of  $K^0$  and  $\bar{K}^0$  changes, which produces a  $K_S$  component in the beam. In our analysis, we only consider decays which originate in the vacuum beam. However, particles can scatter or interact in the regenerator. These events are rejected by vetoing events with any significant energy deposited in the regenerator scintillator.

### 2.2.5 Other detectors

- The mask anti

The mask anti (MA) is located 1.2 m upstream of the regenerator. The MA is used to prevent the decays upstream of the regenerator from crossing over one beam to another. The MA beam holes are larger than the beam size but smaller than the transverse dimensions of the regenerator, so kaons passing through the MA holes can not be scattered by the regenerator.

- V V' bank

A number of trigger hodoscopes are located in the KTeV detector to help trigger on charged tracks and muons. The first such hodoscope (VV') provides fast signals to form trigger logic for all charged particles. A rough count of the number of charged particles can be done at the trigger level using this detector. The VV' hodoscope has a dimension of  $1.9\text{m} \times 1.9\text{m}$ . The upstream hodoscope is called V bank, and the other is called the V' bank. Both V and V' bank consists of 1cm thick scintillators viewed by PMTs mounted on light guides. There are no overlaps between the counters in each bank to avoid a double counting by a single particle.

- Hadron Anti and Muon counters

The Hadron Anti (HA) is located downstream of the CsI calorimeter. Its purpose is to reduce the trigger rate by vetoing events involving charged pions or muons. The HA is located as far upstream of the BA as possible to minimize the rate due to backplash from beam neutrons hitting the BA. The HA has a  $34\text{cm} \times 64\text{cm}$  beam hole so that particles in the beam holes will not interact in the HA. The HA consists of a scintillator bank viewed by PMTs. An

analog sum from all the HA's counters provide information used in the first level trigger. In order to absorb leakage of electromagnetic showers out of the back of the CsI calorimeter, a wall of lead bricks is located just behind the calorimeter. This wall has a thickness of 15 cm. The combined thickness of the CsI calorimeter and the lead bricks corresponds to 2.3 nuclear interaction length. Downstream of the HA was 4 m of steel followed by a hermetic scintillator back used as a muon veto (Mu2). This muon veto consisted of a single plane of vertical, overlapping scintillator counters. The Mu2 veto was used at the trigger level and provided a count of greater than or equal to either one or two muon counts.

### 2.3 Trigger

There are 3 stages in the online trigger: Level 1, Level 2 and Level 3. The Level 1 and Level 2 triggers are hardware triggers, while level 3 is software trigger. These three levels of trigger have a hierarchy in their decision time: the first level takes 19ns without dead time; the second level takes approximately  $3\mu\text{s}$ ; the third level requires about 3ms.

In addition to the three trigger stages, there are two types of trigger in KTeV experiment: Beam and Calibration Triggers. All physics triggers belong to the Beam Triggers. Calibration Triggers are designed to collect data for pedestal measurements as well as other data required for calibrating the detector.

### 2.3.1 Level 1 trigger

The Level 1 trigger is formed using NIM logic. The frequency of Level 1 triggers is about 80KHz. The  $V V'$  bank, the number of drift chamber hits, photon vetoes,  $E_{tot}$  (the sum of the total in-time energy deposited in the CsI detector), HA, and muon counter are the sources of Level 1 trigger. These trigger sources are sent to a series of LeCroy 4508 Programmable Lookup Units (PLU) and Lecroy 4516 Programmable Logic (PL) modules. The Fermilab RF signal is passed in to the PLU and PL to strobe the trigger sources. The strobe is used as a time window; all signals within the window are accepted, and all signals outside the window are rejected. The logical ORs and ANDs of the Level 1 trigger sources is used by the PLUs and PLs to produce the output Level 1 trigger signal. This output is fed into the next stage of the trigger.

### 2.3.2 Level 2 trigger

A Level 1 trigger starts the digitization of ADCs and sends a stop signal for TDCs. This signal also initiates the Level 2 trigger processors. The Level 2 trigger is slower than the Level 1 trigger, requiring approximately 10 times more time than the Level 1 trigger. There are two input sources for the Level 2 trigger: the track processor (see reference [19]) and the Hardware Cluster Counter (see below). For the neutral triggers, only the HCC is used in the Level 2 trigger. The HCC sends the number of found clusters to the Level 2 trigger. The input signals from all Level 2 sources are sent to another series of PLUs with a level signal. The PLUs perform a pattern recognition of trigger sources, and determine whether to read out the event. When the event passes the Level 2 trigger, each PLU generates a number of outputs, which

are used to form a 16-bit trigger mask; the bitwise-AND of all the lookup units is the final 16 bit trigger mask. This means that we can have a maximum of 16 Beam triggers. If an event fails at this stage, that event will be aborted before finishing ADC digitization, which reduces the deadtime.

### 2.3.3 Level 3 trigger

The Level 3 trigger is a software trigger. While this trigger does not reduce the experiment deadtime, it does reduce the amount of data written to tape. The data acquisition system reads out events accepted by the Level 2 trigger, and UNIX workstations are used to reconstruct events and perform cuts on reconstructed variables of the data to filter the events. There are 4 online SGI computers used to process the events. Three of the computers were used for online filtering, while the fourth was used for monitoring and recording calibration events. Each of the three filter planes had eight processors, for a total of 24 dedicated filter processors. Each of the three filter planes used the same filtering software, which applied different filtering code depending upon the Level 2 trigger that fired. After the event passed the filter, a tag was written into the event to classify the event for the future data analysis. The  $K_L \rightarrow \pi^0 \gamma \gamma$  events were tagged with 'LPI0GG'. The software used in the Level 3 trigger shares much of the same code used in the offline analysis, but optimized to process the events faster. Events that pass at least one of the Level 3 filters are tagged and written to the output stream.

Table 2.1 lists 97 Level 3 cuts.

The  $\pi^0 \chi^2$  calculation is in the equation 3.3

Table 2.1: An example of Level 3 filter cut for 1997 and 1999 run

1997 run	1999 run
Best $\pi^0 \chi^2 < 500.0$	Best $\pi^0 \chi^2 < 500.0$
Second best $\pi^0 \chi^2 < 50.0$	Second best $\pi^0 \chi^2 < 80.0$
N/A	Third best $\pi^0 \chi^2 < 50.0$
$0.13 \text{ GeV} < m_{\pi^0} < 0.14 \text{ GeV}$	$0.13 \text{ GeV} < m_{\pi^0} < 0.14 \text{ GeV}$
$55 \text{ m} < \text{Z decay vertex} < 155 \text{ m}$	$50 \text{ m} < \text{Z decay vertex} < 140 \text{ m}$

## 2.4 Hardware cluster counter

The HCC is used in neutral mode Level 2 trigger, and counts the number of distinct clusters of energy in the array of 3100 CsI channels. The HCC consists of 4 parts: Front end electronics, Column Alignment Buffer (CAB) Boards, Cluster Counting Unit (CCU), and Cluster Counter Controller (CCC). The front end electronics process the signals from each of the 3100 CsI channels. These electronics discriminate the CsI dynode signals and fire whenever the signal crosses a fixed threshold. The thresholds were set to fire whenever approximately 1 GeV was deposited in a single crystal. These signals were latched in the front end electronics and the appropriate bits were sent to the HCC on a valid Level 1 trigger. The transmit strobe is generated by the cluster counter controller which is used to control the sequences for both CAB boards and the Cluster Counting Unit. After the CAB boards latched the data, the data was sorted into 64 individual columns and then sent to the CCU boards. Because there are rows (and columns) that contain both large and small blocks, each large block is counted twice for these rows (columns). The CCU executes the cluster counting algorithm and produces a 4-bit cluster count. The three lowest bits of this word are used to indicate a count from 0-7, while the highest bit indicates that 8 or more clusters were found. The HCC required approximately  $2\mu\text{s}$

to finish. However, because of the algorithm implemented, this processing time was fixed.

#### **2.4.1 HCC algorithm**

The HCC algorithm takes advantage of pattern recognition and parallel processing techniques to increase the speed relative to a more conventional algorithm. The idea is that an isolated cluster can be enclosed by a continuous perimeter. If one were to follow this perimeter in a clockwise fashion, the net number of right-hand turns made would be four. So, if one adds up all of the right-hand turns in the whole calorimeter and divides by four, one would find the total number of clusters.

All possible hit patterns for a  $2 \times 2$  array of blocks are shown in Figure 2.7. Right turns are given a weight of +1 while left turns are given a weight of -1. Patterns that do not correspond to a turn are given a weight of zero. Starting from one edge block, all right turns will be counted as +1, and left turn will be counted as -1. Since each block belongs to four different  $2 \times 2$  arrays, every block is used to calculate four different pattern values. The weights shown in 2.7 result in splitting clusters that are touching at corners. This algorithm also has the interesting effect that clusters with holes in them result in a weight of zero. However, such events occasionally occurred in the data, no real physics processes caused such events.

#### **2.4.2 Online monitor**

The purpose of the online monitor program is to monitor the performance of the detectors, trigger hardware, and the Level 3 trigger. In the 1999 run, I helped develop the code to improve the monitoring of the HCC inefficiency. In particular it

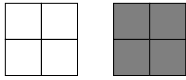
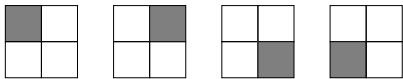
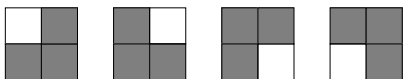
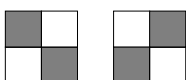

Hit block patterns	Pattern weight
	0: No turns
	+1: One right turn
	-1: One left turn
	+2: Two right turns
	0: No turns

Figure 2.7: Using  $2 \times 2$  array block to calculate the cluster number. This algorithm can implement processing the finding cluster parallel.

was important to keep track of “hot” HCC bits, where a bit fired when there was no associated energy in the CsI crystal. The definition of a hot bit is  $E_{CSI} \text{ (Energy in CsI)} < 0.001 \text{ GeV}$ ,  $NHCCSI \text{ (HCC fired channel)} < 200$  and  $hccbit$  is on. If the percent of hot bits was greater than 2%, a warning sign showed up on the online screen. Usually the percentage of hot bits should be well below 1%. The existence of hot bits resulted from problematic discriminators on the front end Energy Total (ET) boards. By monitoring the hot bit problem, we were able to quickly spot problems with the front end boards and replace them.

Another problem requiring monitoring was the HCC bit inefficiency. An inefficient HCC bit is defined as  $E_{HCC} > 1.5 \text{ GeV}$  and HCC bit is off. In order to be sure

that the bit should have fired, we also checked to see whether the energy in the CsI crystal was in-time. If the energy was in-time, we should get 100% efficiency when the HCC energy was above 2 GeV. The HCC inefficiency was usually well-below a percent. Figure 2.8 shows the strip and blocks of HCC inefficiency.

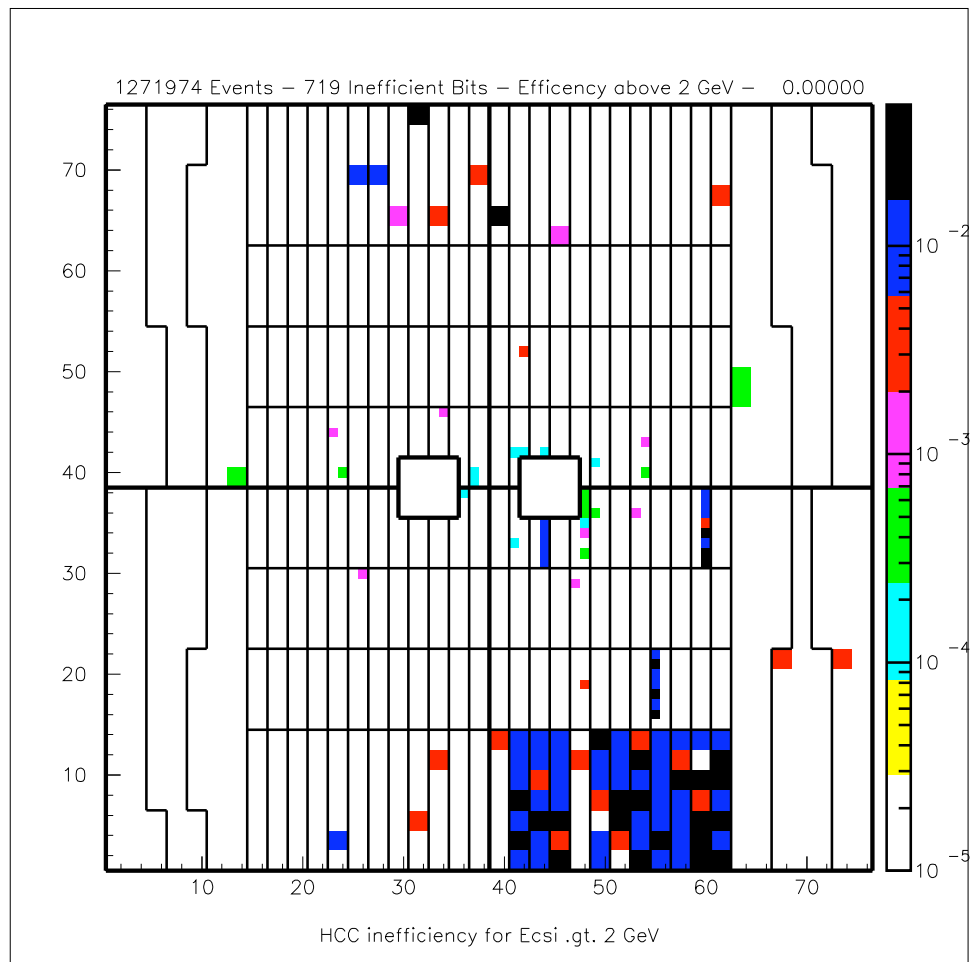


Figure 2.8: The online monitor of the HCC inefficiency. The strips indicate the hardware failure.

Besides the above problems, there are 10 errors caught by the online HCC monitoring:

- Sum of the quadrants not divided evenly by 4
- Boards sum is not equal to simulated board sum
- Latched value is not equal to simulated count
- First column of data not zero
- Last column of data not zero
- Next to last column of data not zero
- overlap column 1-2 in data
- overlap column 2-3 in data
- overlap column 3-4 in data
- Missing bits for large crystals

All these problems are related to hardware cluster counter(HCC) and Column Alignment Buffer (CAB) boards. The item 1 can be caused by item 5,6,7, or the edge or hole channels were not properly set to zero.

## 2.5 Data acquisition

The data acquisition system (DAQ) was used for online monitoring, the Level 3 trigger, and to record data to tape. The DAQ consisted of 6 data streams and 4 SGI computers forming a matrix. Four of the data streams were used to read out

the CsI data, while the other two streams were used for the other ADCs and TDCs in the experiment. A VME memory module was located at each of the 24 nodes in this matrix. The raw data are stored in these VME modules. In total the memories can store 4GB data, which is big enough to buffer data from an entire spill (about 2GByte). The front end crates and the DAQ are connected with RS485 buses whose bandwidth is 40 MBytes. The six streams have a bandwidth of 240 MBytes. The 6 sub-events each of the 6 streams are written into the asynchronous VME memory nodes on a given computer. Of the four computers, three are used for the Level 3 triggering. The other plane monitors the detector response and performed the online calibration. Each SGI computer can write out to 3 or 4 DLT tapes. The maximum number of data types is 16.

### 2.5.1 AzTEC

The readout crate for the HCC contained a crate controller (DYC) and a crate trigger interface module (CTI) which were connected in parallel with the HCC. The more detail of CTI can be found in reference [20]. The CTI module inserted some data words into the readout stream to identify the crate and the event number as shown in Table 2.5.1. The original CTI module stored only the data from a single event, and did not buffer the readout. However, the HCC did buffer the event data to reduce the deadtime incurred during the event readout. Since the CTI could not buffer the data, the HCC event buffer could not be used, resulting in additional deadtime.

The AzTEC module was built at the University of Arizona to act as a buffered CTI module. The AzTEC module was also used as a buffered latch to

store Level 2 information when it was realized that this module could also be used as a fast latch. This module was designed as a CAMAC module with all digital features implemented in an ALTERA programmable logic device (PLD). The hardware configuration is programmed in EPROM. After the installation of the AzTEC modules, the dead time was reduced from  $10\mu\text{S}$  to  $6\mu\text{S}$ .

Table 2.2: CTI data format

<i>Bit no.</i>	15	14	13	12	11	10	9	8	7	6	5	4	3	2	1	0
<i>ECL input</i>	ordinal no.				sparse code				XX (don't care)							
<i>FERA word 1 output</i>	F				F				F				F			
<i>FERA word 2 output</i>	sparse code				ordinal no.				crate ID							

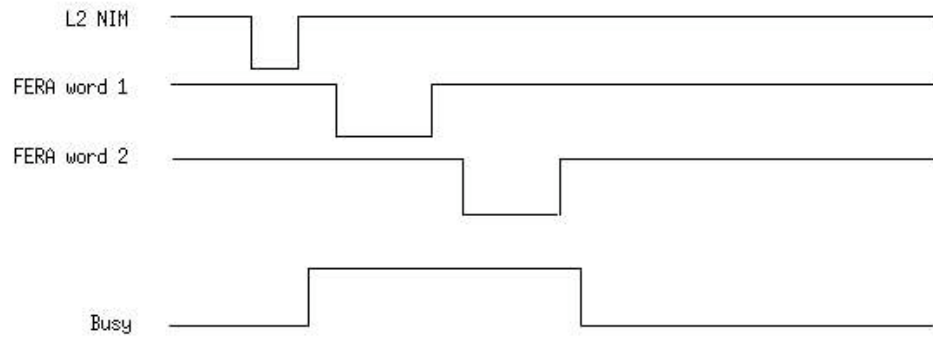


Figure 2.9: Timing diagram for CTI state machine 1. Width of busy is 400 ns.

The AzTEC module used a CAMAC interface that allowed it to be controlled, read, and written to via a computer. The following CAMAC commands were implemented:

Table 2.3: CAMAC command

<i>CAMAC command ...</i>	<i>of type ...</i>	<i>executes ...</i>
F0*A0	8-bit read	read CSR
F0*A1	8-bit read	read crate address
F0*A2	16-bit read	read ECL input
F0*A3	16-bit read	test word 2
F0*A4	8-bit read	read module ID
F0*A5	16-bit read	test word 1
F0*A6	4-bit hex display	display sparse code (dot on)
F0*A7	4-bit hex display	display ordinal no. (dot off)
F16*A0	8-bit write	write CSR
F16*A1	8-bit write	write crate address
F16*A2	16-bit write	test signal for L2 trigger input register
Z	control	clear busy and CSR
F9*A0	control	clear busy only
(F0+F9+F16)*An, n=0-7	control	Q & X response

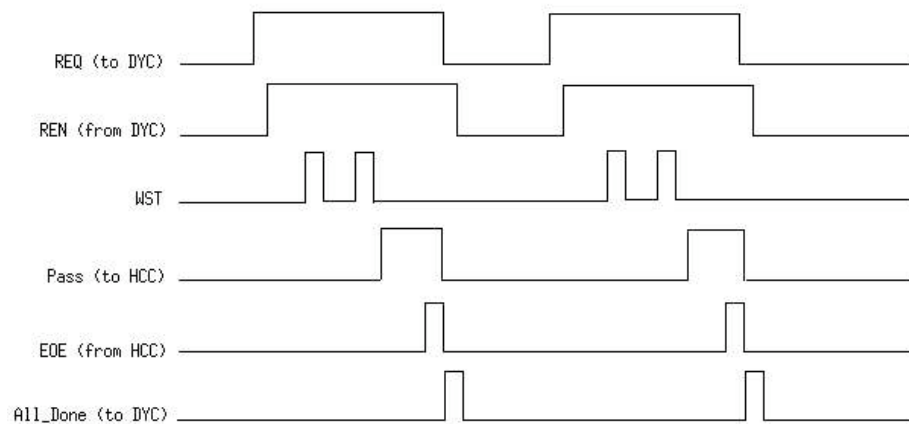


Figure 2.10: Timing diagram for CTI state machine 2. Timing elapsed between REN and WST is 175 ns (it takes 125 ns for a word to show up on the data line from the FIFO). Width of WST is 50 ns, and WST period is 100 ns. Width of All\_Done is 100 ns

- Get data from the front connector.
- Get the address from backplane.
- Get module number from a latch.
- Combine these to a data stream, and put them into a FIFO.
- Output the data stream from FIFO controlled by read strobe.

These commands are shown in Table 2.3. There are 2 state machines (read, write) and 2 decoders in the project.

I was responsible for this whole project including:

1. Altera PLD design and layout.
2. PC board design and layout (Power PCB).
3. Assembly of 20 boards and testing.
4. . Wrote driver for the test and data acquisition ( including writing a driver in assembly language (intel 8086) for the PC board)

During debugging the AzTEC boards, I was able to solve the following problems:

- Synchronize the two state machines.
- Remove a number of bounced signals on the board.
- Add 10 test points to allow one to view the intermediate state inside the PLD.

This project was finished in March 1999. The modules used during the KTeV 1999 run were very reliable and stable.

## CHAPTER 3

### DATA SELECTION AND RECONSTRUCTION

In this chapter, we discuss the event reconstruction used in this analysis. We have the following information about each data event: the position and energy deposited by the photon in each block of the CsI detector. What we need in the analysis is the kaon energy, decay vertex, the  $\gamma\gamma$  invariant mass  $M_{\gamma\gamma}$  and other calculated variables such as fusion shape  $\chi^2$ . This information can all be determined solely from the calorimeter information. Since  $K_L \rightarrow \pi^0\gamma\gamma$ ,  $K_L \rightarrow \pi^0\pi^0$ , and  $K_L \rightarrow \pi^0\pi^0\pi^0$  are neutral, we do not use the tracking information in the our analysis. We will discuss clustering and vertexing.

#### 3.1 Reconstruction overview

The event selection for the  $K_L \rightarrow \pi^0\gamma\gamma$  data proceeds in four stages: the hardware triggers (Level 1 and Level 2), the software trigger (Level 3), the split, and the final analysis. During the Level 3 trigger processing, each event is tagged with one or more tags based upon the results of the Level 3 output. Groups of tagged events are written to specific output tapes. To isolate the  $K_L \rightarrow \pi^0\gamma\gamma$  events, we stripped events from the QKN tapes for the 1999 data, KZZ for 1997 data and KQAZ for 1996 data. For the 1999 run, some data were corrupted, so we had to process the raw QKS data tapes in order to recover these data.

To determine the branching ratio for  $K_L \rightarrow \pi^0 \gamma \gamma$ , we need to normalize these events to a known branching ratio. We used the decay  $K_L \rightarrow \pi^0 \pi^0$  because it has a nearly identical topology to our signal mode. In fact, after a very basic event selection, our data sample is dominated by these decays. The  $K_L \rightarrow \pi^0 \pi^0$  events were collected with the same hardware and software triggers as the  $K_L \rightarrow \pi^0 \gamma \gamma$  events, and were written to the same output tapes. In our analysis, we were able to tune our cuts to retain high efficiency for  $2\pi^0$  events while reducing the background that resulted from  $K_L \rightarrow \pi^0 \pi^0 \pi^0$  decays.

## 3.2 Data selection

### 3.2.1 1996 and 1997 data

The data used in this analysis were collected during the 1996 and 1997 E832 running period using the B04 ( $\eta_{00}$ ) trigger. This trigger collects events with approximately 40-160 GeV of energy in the calorimeter at Level 1 and four or five hardware clusters in the CsI calorimeter at Level 2. For the 1996 data, this trigger was defined as

$$\text{B04} = \text{SPILL} \bullet \text{ET\_NEUT} \bullet \text{NOTVETO} \bullet \text{!CA} \bullet \text{!BAGAM} \bullet \text{HCC\_4OR5}$$

where the detail triggers are defined as

$$\text{ET\_NEUT} = \text{ET\_3BD} + \text{ET\_THR3}$$

$$\text{ET\_3BD} = (\geq 3 \text{ ET boards} > 3 \text{ GeV})$$

$$\text{ET\_THR3} = (\text{ET analog sum} > 27 \text{ GeV})$$

$$\text{NOTVETO} = \text{!SA2} \bullet \text{!SA4} \bullet \text{!CIA} \bullet \text{!MA} \bullet \text{!MU2} \bullet \text{!REG}$$

$$\text{BAGAM} = \text{BAGAM\_LEFT} + \text{BAGAM\_RIGHT}$$

$$\text{BAGAM\_LEFT (RIGHT)} = \text{BA\_EM12\_LEFT (RIGHT)} \bullet \text{!BA\_HAD\_LEFT (RIGHT)}$$

The  $\eta_{00}$  trigger also requires little activity in most of the photon vetoes. We set some photon veto thresholds in the Lever 1 trigger, and we also cut on those photon vetoes in offline analysis.

### 3.2.2 1999 data

In the 1999 run the  $\eta_{00}$  trigger was modified slightly. The trigger was defined as:

$$\text{B04} = \text{SPILL} \bullet \text{ET\_NEUT} \bullet \text{NOTVETO} \bullet \text{!CA} \bullet \text{!BAGAM} \bullet \text{4HCC}$$

The detail triggers are defined as:

$$\text{NOTVETO} = \text{!SA2} \bullet \text{!SA4} \bullet \text{!CIA} \bullet \text{!MA} \bullet \text{!MU2} \bullet \text{!REG}$$

We extracted the 1999  $K_L \rightarrow \pi^0 \gamma \gamma$  events from the 39 QKN DLT tapes, corresponding to runs from 13260 to 14523. During this stripping process we applied the cuts listed in the Table 3.1. These cuts are much looser than the cuts used in the analysis and were used to reduce the size of the data set to a manageable size. The size of the 1999 data set was comparable to the combined data from the 1996 and 1997 data sets.

We request the total in-time (during one event strobe) hit on the drift chamber is less than 100, and the decay vertex is less than 134 m. The total kaon energy is less than 200 GeV, and the energy stored at the first Back Anti is less

Table 3.1: 1999 strip cuts

$\text{NHIT} < 100$
$\text{ZDK} < 134 \text{ m}$
$\text{EK} < 200 \text{ GeV}$
$\text{EBA1} < 7 \text{ GeV}$

than 7 GeV.

### 3.3 Clustering

In order to reconstruct the  $K_L \rightarrow \pi^0 \gamma \gamma$  events, we have to first isolate events with exactly four photon candidates. We classify photons as isolated clusters of energy in the CsI calorimeter that have no associated tracks.

There are two types of clustering: hardware and software. A hardware cluster is one in which the highest energy block in the cluster has an associated HCC bit that has fired. Otherwise, when the HCC bit is off, the cluster is classified as a software cluster.

During the first pass of the clustering algorithm, a list of all hit blocks (blocks with energy above a specified threshold) is generated. We loop over this list of hit blocks, choosing one block as a seed block. If the seed block's energy is greater than its neighbors, it is flagged as a local maximum. For the list of all local maxima, clusters are formed. Initially, these clusters are assumed to be  $7 \times 7$  for small blocks and  $3 \times 3$  for large blocks. The “raw” energy of each of these clusters is determined by summing up the energy in these square arrays of crystals. Blocks that are shared by two (or more) clusters have their energy split between the clusters based upon

the ratio of the energies of the clusters.

The clustering algorithm is controlled by a bit mask shown in Table 3.2. Corrections to the energy of each cluster will be discussed below.

Table 3.2: Clustering unpack bit mask

Bit	Definition	On of Off
1	do not use default values	On
2	do hardware clustering	On
3	do software clustering	On
4	change number of time slices	On
5	change cluster threshold	On
6	change seed threshold	On
7	change number of small blocks	On
8	change number of large block cluster size	On
9	do overlap separation	On
10	do not do fusion finding	Off
11	unpack all slices	On
12	unpack around HCC bits (for L3)	Off
13	unpack around tracks (for L3)	Off
14	allow reclustering	Off
15	do final corrections	On

### 3.3.1 Hardware clustering

There are two clustering passes, a Hardware Cluster Counter (HCC) seeded pass and a software cluster pass. In the first pass, cluster seeds are defined as the blocks which passed the hardware HCC threshold and are local maximum. Then fixed size regions, 7x7 for small blocks and 3x3 for large blocks, are chosen around these seeds. These clusters can and do share blocks. The number of HCC seeded clusters is stored as the variable NHCLUS. Because these clusters include blocks with HCC

bits on, hardware clusters are in-time with the event.

### 3.3.2 Software clustering

When bit 3 of the clustering mask (Table 3.2) is ON, the analysis software will perform software clustering. This pass uses blocks which are above an energy of 100 MeV, are local maxima, and were not included in a previously found cluster as seeds. Clustering is done as above, with the number of software clusters stored as the variable NSCLUS. The variable NCLUS contains the total number of clusters, including the hardware and the software clusters. Information on both kinds of clusters are in the common block CSICLUS, with the HCC seeded clusters coming first. Since there is no timing cut on the software clusters, these clusters can occur both before and after the in-time event.

### 3.3.3 Position determination

Once the clusters have been found, the position of each cluster is determined. To determine the position in the  $x$  direction, the position algorithm sums up three columns of energy ( $C_1$ ,  $C_2$  and  $C_3$ ) in the  $3 \times 3$  array of blocks centered on the seed block, where  $C_2$  is the energy of the column containing the seed block. Then, the ratios  $R_1 = C_1/C_2$  and  $R_2 = C_3/C_2$  are calculated. The two ratios are used as input to a lookup table to determine the position of the cluster relative to the seed block. The lookup tables were determined from real data using  $K_L \rightarrow \pi^0\pi^0$  decays. The  $y$  position was determined in a similar fashion.

### 3.3.4 Clustering corrections

After all clusters have been found and their positions determined, a number of corrections are applied to the clusters.

- **Overlap correction:** When a cluster shares crystals with another cluster, a correction is applied to estimate the energy shared between the two clusters. This correction is based upon GEANT generated shower shapes.
- **Intrablock correction:** If the position of the cluster is near the edge of the seed block rather than the center, a correction was applied to the energy of the cluster. This correction was taken from data.
- **Threshold correction:** During normal running the smallest energy that could be read out by the CsI electronics was 7 MeV in a single crystal. Corrections for energy that was below this threshold were applied. These corrections were taken from special runs with no threshold applied.
- **Missing block correction:** When a cluster is near the outer edge of the calorimeter or one of the beam holes, some of the energy can be lost. We correct for this energy based upon shower shapes taken from GEANT simulations.
- **Run-by-run correction:** The response of crystals changed over time. Much of this change was due to radiation effects and were highest at the center of the CsI array. This correction was determined from data where a laser was pulsed at the back of each crystal.
- **Non-linearity correction:** After applying all of the corrections described above,

a small non-linear dependence of the ratio  $E/p$  on  $p$  remained. This non-linearity was of the order of 0.5%. The non-linearity was then used to linearize the response of the  $E/p$  distribution.

### 3.4 Reconstruction of signal mode $K_L \rightarrow \pi^0 \gamma \gamma$

After clustering has been done, we can begin the reconstruction of the signal events. We select events with exactly four hardware clusters and then calculate the kaon decay position. If we assume the mass of the four photon system is the kaon mass, we can use the following equation to determine the decay position  $Z$ .

$$m_K^2 = \left(\sum_{i=1}^4 E_i\right)^2 - \left(\sum_{i=1}^4 P_i\right)^2 \approx \sum_{i=1, j=1}^{4, j < i} \frac{E_i E_j r_{ij}^2}{Z^2},$$

$$Z_{normal}^2 \approx \sum \frac{E_i E_j r_{ij}^2}{m_K^2}. \quad (3.1)$$

where  $E_i$  is the cluster energy,  $r_{ij}$  is the distance between two clusters  $i$  and cluster  $j$ .  $Z_{normal}$  is the distance between the kaon decay position and the CsI detector. So, the decay position can be determined from:  $Z = Z_{csi} - Z_{normal}$ , where  $Z_{csi}$  is the distance between the target and the CsI calorimeter.

Once we know the kaon decay position, we want to calculate the  $\pi^0$  mass and the  $\gamma\gamma$  mass of the remaining two photons. If we assume that photons 1 and 2 come from the pion, we can use the decay position  $Z$  to determine both of these quantities. For four photons there are three possible unique combinations. We loop over all three combinations and keep the best combination as defined below. To determine the pion mass, we use the following relationship, where  $E_i$  and  $r_{ij}$  are

defined above, and  $Z$  is determined from Eq. 3.4.

$$m_{\gamma_i\gamma_j}^2 = \frac{E_i E_j r_{ij}^2}{Z^2} \quad (3.2)$$

We choose the best mass combination based upon the  $\chi^2$  for each combination shown in Eq 3.3.

$$\chi^2 = \frac{(\sqrt{E_1 E_2 r_{12}^2} - \sum \frac{m_{\pi^0}}{m_K} \sqrt{E_i E_j r_{ij}^2})^2}{(\sqrt{E_1 E_2 r_{12}^2} + \frac{m_{\pi^0}}{m_K} SIGTOT)^2} \quad (3.3)$$

SIGTOT is the total error on the product of  $Z$  times the reconstructed  $m_{\pi^0}$  for the three combinations.

The combination with the minimum  $\chi^2$  is selected as the best combination. We also record the second and third best combination in arrays for later use. The  $\gamma\gamma$  invariant mass of the remaining two photons,  $M_{\gamma\gamma}$ , can be determined from Eq. 3.2. Like  $M_{\pi^0}$ , we store the second and third best combination of  $M_{\gamma\gamma}$ . The reconstructed  $\gamma\gamma$  mass is shown in Figure 3.1

In the  $K_L \rightarrow \pi^0 \gamma\gamma$  decay two Dalitz variables can be determined from the photon energies and positions. The first,  $Z_{Dalitz}$ , is related to  $M_{\gamma\gamma}$  and its shape depends strongly upon the vector exchange parameter  $a_V$ . The second Dalitz parameter,  $Y_{Dalitz}$ , can be determined from the following:

$$Y_{Dalitz} = \frac{|E_3 - E_4|}{M_K}. \quad (3.4)$$

$E_3$  and  $E_4$  are the photon energy in the center of mass frame of the  $K_L$ .

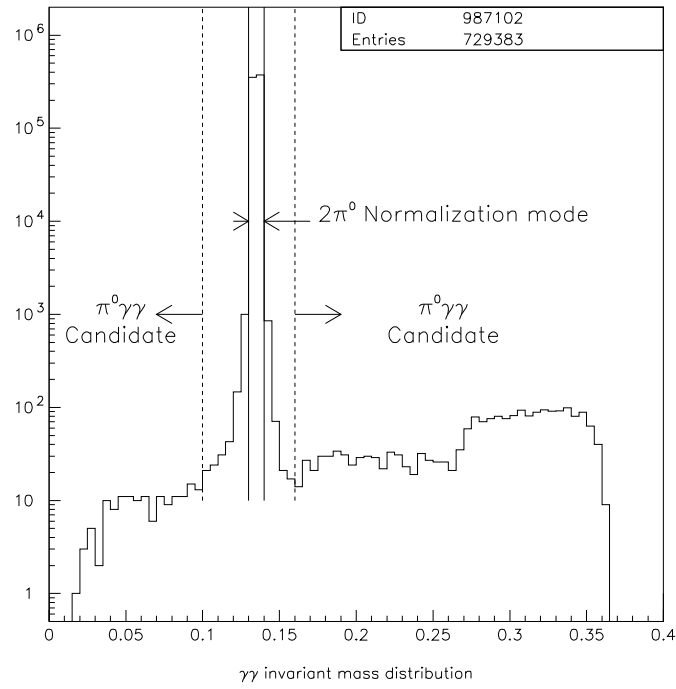


Figure 3.1: The  $\gamma\gamma$  invariant mass distribution from data after all cuts. The normalization mode ( $K_L \rightarrow \pi^0\pi^0$ ) is indicated by the two solid vertical lines, and the  $\pi^0\gamma\gamma$  candidates are marked by the arrow and the dashed lines.

KTEV Event Display  
/d0/jwang/99\_603/QKN010.dat

Run Number: 13847  
Spill Number: 101  
Event Number: 43138998  
Trigger Mask: 8  
All Slices

Track and Cluster Info  
HCC cluster count: 4  
ID Xcsi Ycsi P or E  
C 1: 0.2275 0.4982 10.89  
C 2: -0.4157 0.5524 13.73  
C 3: -0.1070 -0.4646 22.05  
C 4: -0.3120 -0.0257 12.05

Vertex: 4 clusters  
X Y Z  
-0.1092 0.0286 127.695  
Mass=0.4977  
Pairing chisq=0.00

- - Cluster
- - Track
- - 10.00 GeV
- - 1.00 GeV
- - 0.10 GeV
- - 0.01 GeV

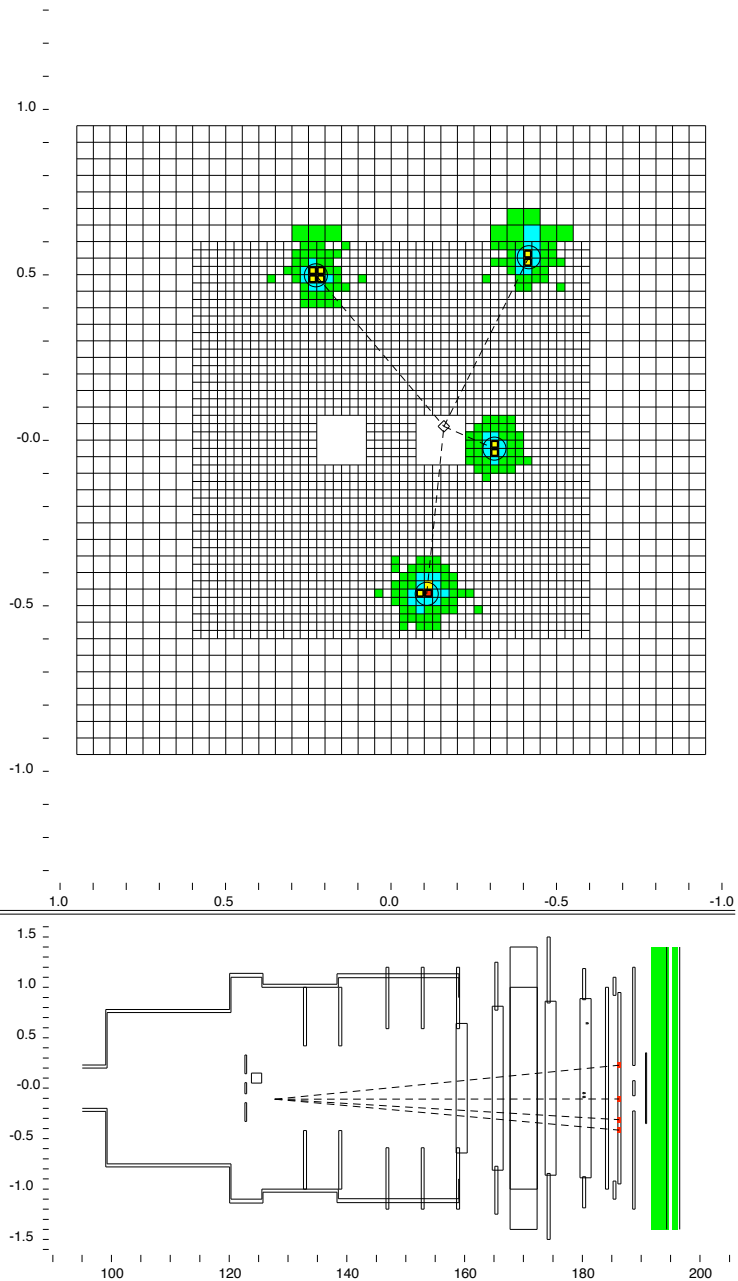


Figure 3.2: An event display for a  $K_L \rightarrow \pi^0 \gamma \gamma$  candidate. The top display shows the response of the calorimeter to the four photons. The bottom display shows an  $x$  view of the whole detector with the reconstructed paths of each of the four photons. The four photons are neutral, so they are not deflected when traversing the analysis magnet.

Figure 3.2 shows an event display for a fully reconstructed  $K_L \longrightarrow \pi^0 \gamma \gamma$  event from the data. The  $K_L$  decays at 126 m downstream of the target. Four hardware clusters are shown in the top display, while the paths of the photons are shown in the bottom display.

### 3.5 Reconstruction of $K_L \rightarrow \pi^0 \pi^0$

$K_L \rightarrow \pi^0 \pi^0$  is used to estimate the  $K_L$  flux since we can reconstruct clean  $K_L \rightarrow \pi^0 \pi^0$  events with less than 5% background. Also the branching ratio of  $K_L \rightarrow \pi^0 \pi^0$  is well known. Since there are a copious number of  $K_L \rightarrow \pi^0 \pi^0$  decays, we can also use these events to test how well the Monte Carlo reproduces the data.

The procedure to reconstruct  $2\pi^0$  is the same as in reconstructing  $K_L \rightarrow \pi^0 \gamma \gamma$ . The  $K_L \rightarrow \pi^0 \pi^0$  events are isolated from the  $K_L \rightarrow \pi^0 \pi^0$  events by a simple cut on the  $M_{\gamma\gamma}$  distribution. After all cuts, we select  $M_{\gamma\gamma}$  within 0.14 GeV and 0.16 GeV. As seen in Figure 3.1, the normalization clearly peaks near the  $\pi^0$  mass.

## CHAPTER 4

### DATA ANALYSIS

In this chapter, we will discuss the selection criteria used to isolate the  $K_L \rightarrow \pi^0 \gamma \gamma$  signal. The branching ratio of  $K_L \rightarrow \pi^0 \gamma \gamma$  is of order  $1 \times 10^{-6}$ , while the  $K_L \rightarrow 2\pi^0$  branching ratio is  $9 \times 10^{-4}$ , and  $K_L \rightarrow 3\pi^0$  is at the 0.21 level. So most of the events in the data are background at this point. To reduce these backgrounds, we have developed a number of cuts based upon kinematics and other detector signatures. We also need to remove a third type of background due to interaction of particles with the vacuum window.

#### 4.1 Data quality cuts

To ensure the quality of the data, we need to verify a number of quantities. These cuts get rid of events in which the detector may have had problems. They also help to get rid of unwanted events that may be hard to simulate in our Monte Carlo.

- Reject bad spill events
- Verify Level 3 'PI0GG' tag
- Verify Level 1 trigger
- Verify if the event is within the in-time window

- Verify the event is in the vacuum beam

The bad spill cut removes events that may have had hardware failures such as problems with the drift chambers, CsI readout problems, and DAQ problems. These problems were registered in a database on a spill-by-spill basis to be used in the offline analysis. The bad spill cut rejects approximately 7% of the total data. We also checked the Level 3 'PI0GG' tag to ensure that the event was flagged by Level 3 as a  $K_L \rightarrow \pi^0 \gamma \gamma$  event. The Level 1 trigger was verified to ensure that the particles from the  $K_L \rightarrow \pi^0 \gamma \gamma$  decay fired the trigger. This removes events where the Level 1 trigger elements were fired by accidental activity, which is difficult to simulate. Finally, we required that all of the decay particles occurred during the in-time window and that the event reconstructed in the vacuum beam, and not the regenerator beam.

## 4.2 The drift chamber in-time hit (NHIT) cut

Figure 4.1 shows the number of in-time drift chamber hits DATA/MC overlay for  $2\pi^0$ . The data is dotted histogram, and Monte Carlo is the solid lined histogram. The second plot shows the ratio of the data over the Monte Carlo and shows a slight slope. This cut is optimized to get the maximum signal to background ratio. We cut NHIT at 23, and reject 28%  $\pi^0 \gamma \gamma$  candidates.

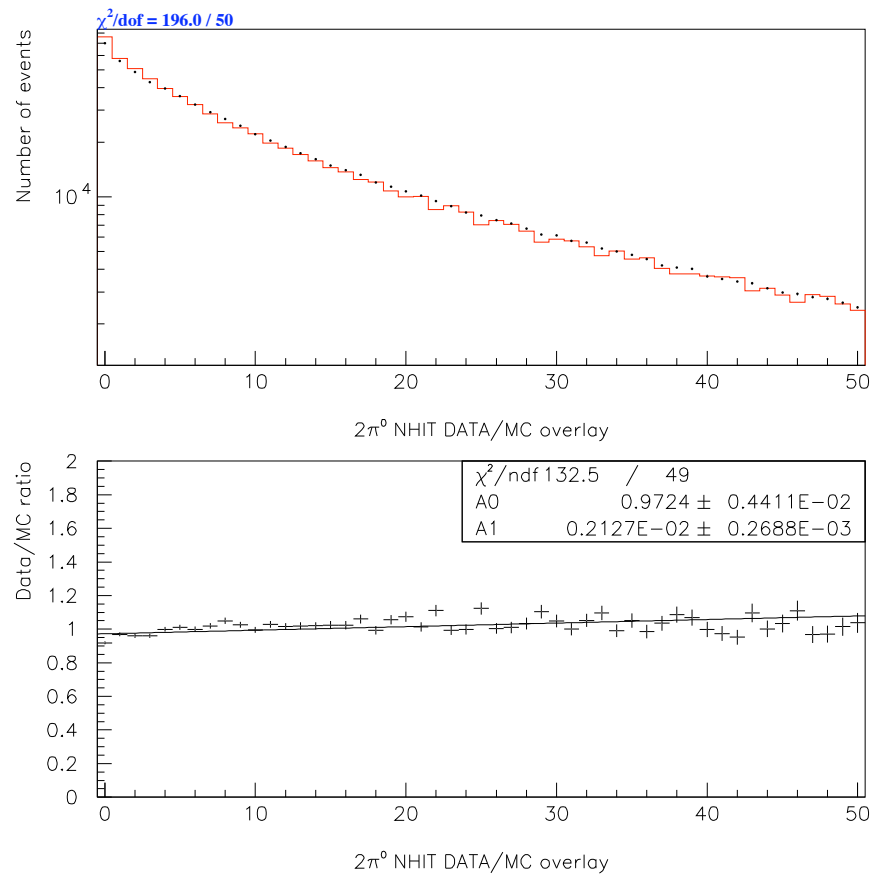


Figure 4.1: The number of in-time drift chamber hits for  $2\pi^0$  data (dot) and Monte Carlo (histogram). The second plot is the ratio of the data over the Monte Carlo and shows a slight slope. There are also a number of small peaks in the data that correspond to tracks. A single track produces 16 hits in the drift chamber system.

### 4.3 Vacuum windows cut

Neutron interactions in the vacuum window produce  $2\pi^0$  and  $\eta$  particles. To remove vacuum window interactions, we loop over all two-photon combinations and reconstruct the decay position of the pair assuming that it is a  $\pi^0$ . Using this  $Z$ -position, we then reconstruct the mass of the second pair of photons. In Figure 4.2 one sees that there are two enhancements at the  $\pi^0$  and  $\eta$  mass for decay vertices greater than 158 meters. We remove those events that have a mass between 0.120-0.150 GeV/c<sup>2</sup> and 0.530-0.560 GeV/c<sup>2</sup> with a vertex position greater than 158 m.

### 4.4 The ellipse cut

Most of the  $K_L \rightarrow \pi^0\pi^0$  events can be rejected by requiring the mass of the non- $\pi^0$  photon pair ( $M_{\gamma\gamma}$ ) to reconstruct away from the  $\pi^0$  mass. However, since our algorithm for choosing the correct photon pairing can sometimes choose the wrong combination, we have developed some cuts to remove mispaired events. We make a 2-dimensional plot of  $M_{\pi^0}$  versus  $M_{\gamma\gamma}$  for the second and third best combinations. As shown in Figure 4.3, our sample contains a small number of events where the best  $\pi^0$  mass combination did not correctly identify the correct  $2\pi^0$  combination. Any event where  $M_{\pi^0}$  and  $M_{\gamma\gamma}$  both are in the elliptical regions defined below is thrown away.

$$ELLIPX = (M_{\gamma\gamma} - 0.135) \times 0.96593 - (M_{\pi^0} - 0.135) \times 0.25882$$

$$ELLIPY = (M_{\gamma\gamma} - 0.135) \times 0.25882 + (M_{\pi^0} - 0.135) \times 0.96593$$

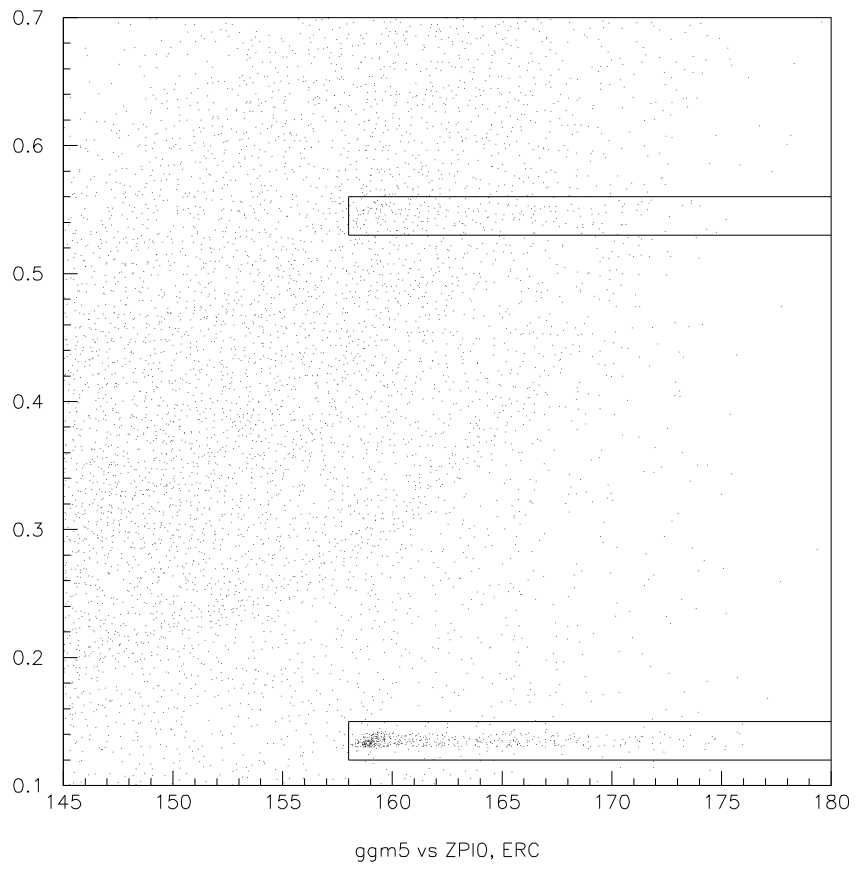


Figure 4.2: Mass versus decay position for four cluster events. Enhancements at the  $\eta$  and  $\pi^0$  mass are evident.

$M_{\gamma\gamma 2}$  and  $M_{\pi^0 2}$  are the second best combination of  $M_{\gamma\gamma}$  and  $M_{\pi^0}$  and ELLIPX and ELLIPY are the ellipse variables. We then require:

$$\left(\frac{ELLIPX}{0.035}\right)^2 + \left(\frac{ELLIPY}{0.010}\right)^2 > 1 \quad (4.1)$$

We do the same cut to the third best combination.

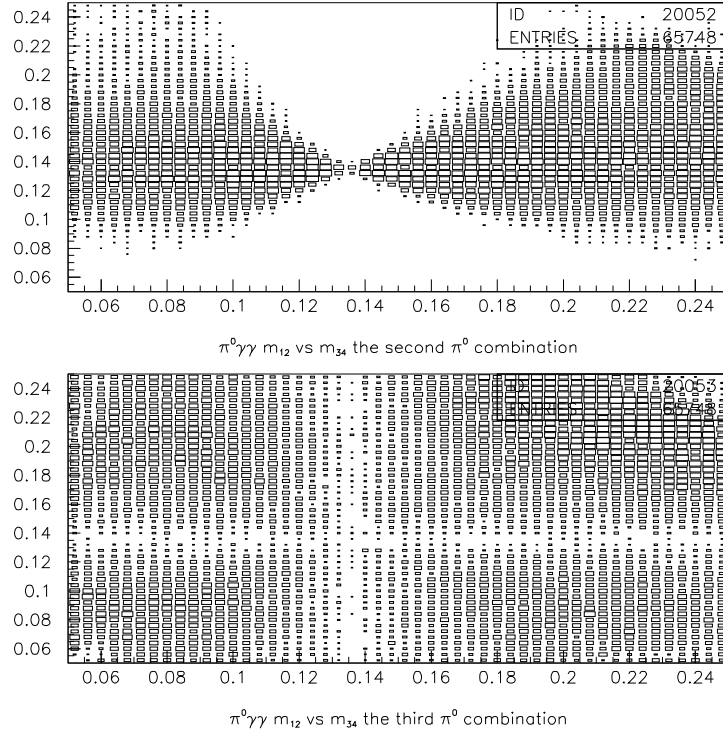


Figure 4.3:  $M_{\pi^0}$  versus  $M_{\gamma\gamma}$ , top: the second best  $\pi^0$  combination, bottom: the third best  $\pi^0$  combination

To further remove backgrounds from  $2\pi^0$  decays, we also require that events satisfy the LREGOK criteria. This requirement ensures that there is no activity in the regenerator which could produce  $K \rightarrow \pi^0\pi^0$  events that scatter from the regenerator beam into the vacuum beam.

Figure 4.4 shows the  $M_{\gamma\gamma}$  for  $2\pi^0$  Monte Carlo events after all analysis cuts. There are very few events that reconstruct away from the  $\pi^0$  mass. These bulk of the  $K_L \rightarrow \pi^0\pi^0$  events are removed by requiring  $M_{\gamma\gamma}$  be greater than 0.16 GeV/c<sup>2</sup> or less than 0.10 GeV/c<sup>2</sup>. In our final  $\pi^0\gamma\gamma$  sample, misreconstructed  $2\pi^0$  events comprise less than 1% of the total background.

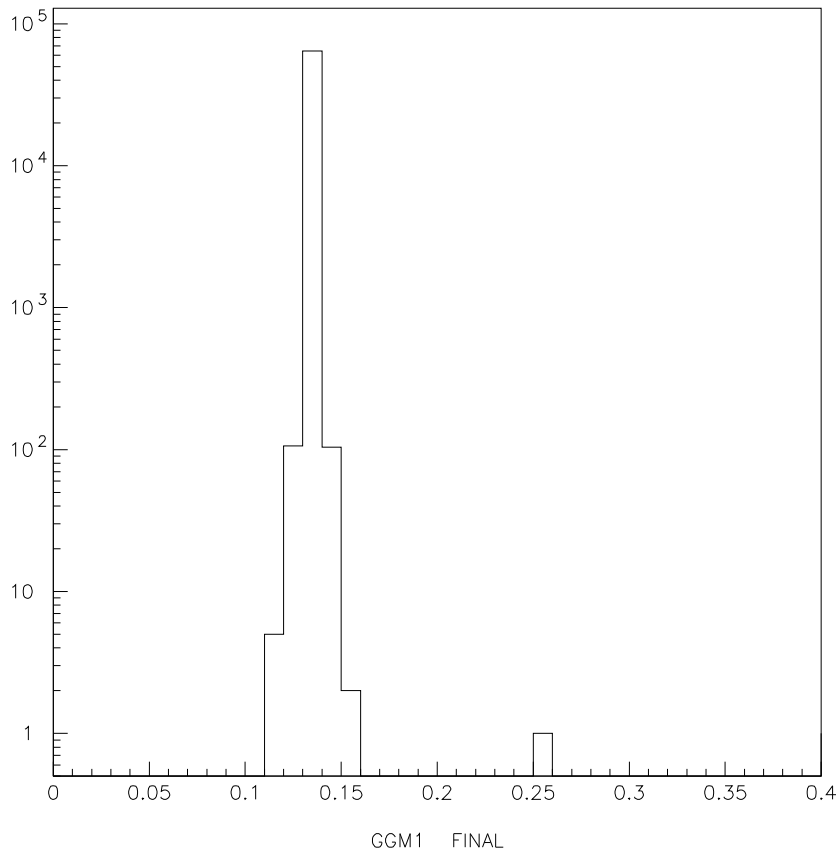


Figure 4.4:  $M_{\gamma\gamma}$  for  $2\pi^0$  after all cuts

## 4.5 Calorimeter cuts

At this point the remaining background is almost completely due to  $K_L \rightarrow \pi^0 \pi^0 \pi^0$  events. Much of this background has been removed by requiring only four hardware clusters in the calorimeter. However, the  $K_L \rightarrow \pi^0 \pi^0 \pi^0$  events can still contribute to the background in the following ways. 1) If two photons miss the calorimeter, then there will only be four clusters in the CsI. 2) One photon can miss the calorimeter, and two photons merge in the calorimeter to reconstruct as a single cluster. This is denoted as a single fusion event. 3) Four photons can merge into two clusters in the calorimeter, which we call a double fusion event. 4) Finally, it is possible for three photons to hit the same spot in the calorimeter and reconstruct as a single cluster. This is called a triple fusion event.

To remove  $3\pi^0$  decays, we first cut on the center of energy at the calorimeter. This cut removes  $K_L \rightarrow \pi^0 \pi^0 \pi^0$  events because any missing photons tends to produce a center of energy outside of the CsI beam holes. We multiplied XCENTE by the sign of the regenerator position so that XCENTE for vacuum events is negative. We require  $\text{ABS}(\text{YCENTE}) < 0.05\text{m}$  and XCENTE to within 0.05 m of the center of the vacuum beam. The comparison of data to MC for the  $3\pi^0$  center of energy is shown in Figure 4.5.

A small fraction of the  $3\pi^0$  background results from events in which more than four photons are resolved in the calorimeter, but at least one of the photons is below the HCC trigger threshold. These events will have one or more in-time software clusters. We remove these events by requiring no in-time software clusters above 0.6 GeV. To reduce our dependence upon the simulation of the ET and HCC

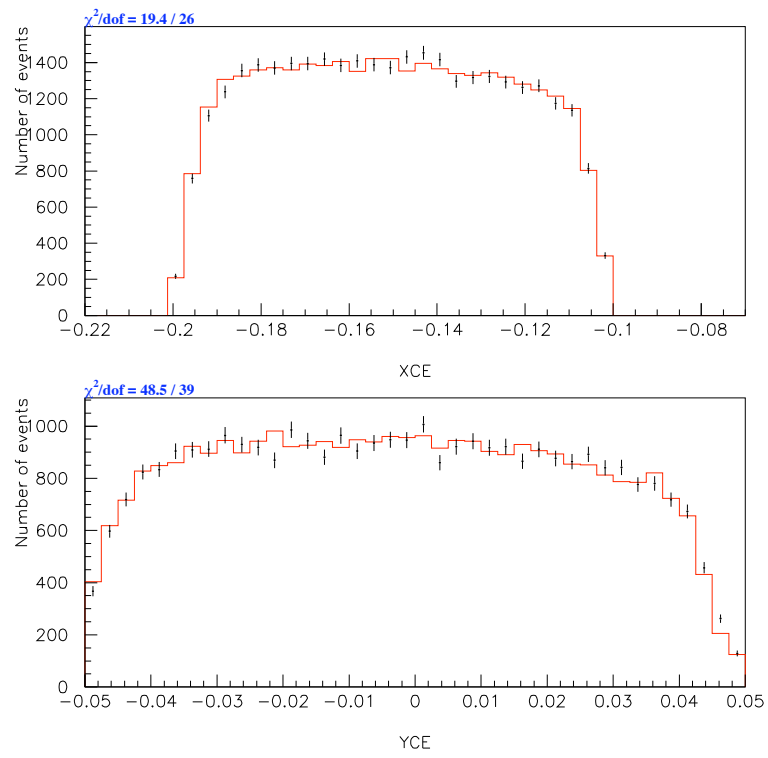


Figure 4.5: The comparison of the center of energy data to Monte Carlo for  $3\pi^0$  events

trigger thresholds we require the total energy of the event to exceed 40 GeV and that the individual cluster energies are above 2.0 GeV.

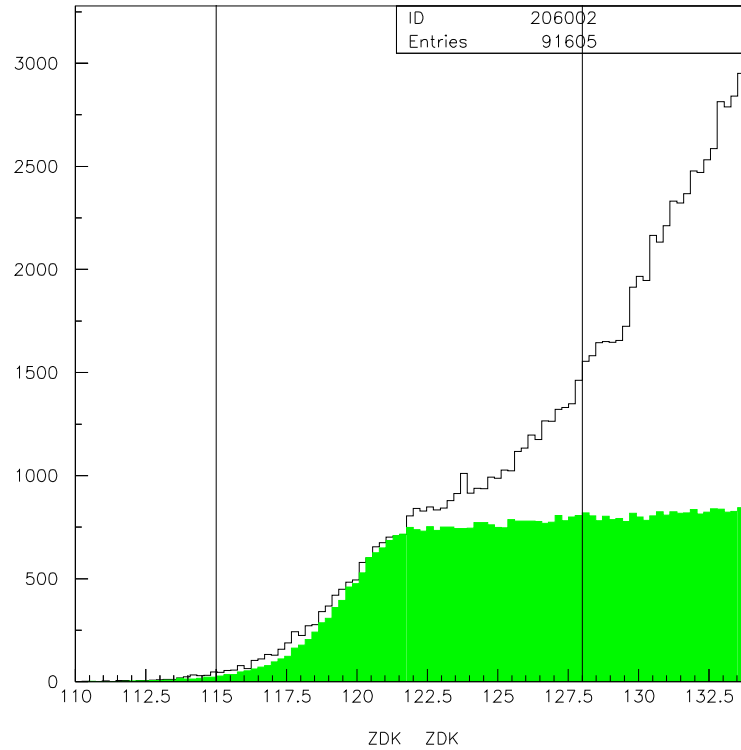


Figure 4.6: The decay vertex for all events and  $2\pi^0$  (green). Two vertical lines indicate the position of the cuts.

#### 4.6 Z vertex cut

By restricting the downstream end of the decay volume we can severely reduce the amount of  $3\pi^0$  background in which one or two photons miss the calorimeter. For such events the decay position reconstructs downstream of the true decay position.

As shown in Figure 4.6 the decay position distribution rises steeply after 128 meters. The vertex position for  $2\pi^0$  and  $\pi^0\gamma\gamma$  events is essentially flat. Figure 4.7 shows this cut rejects most of the  $3\pi^0$  single fusion events.

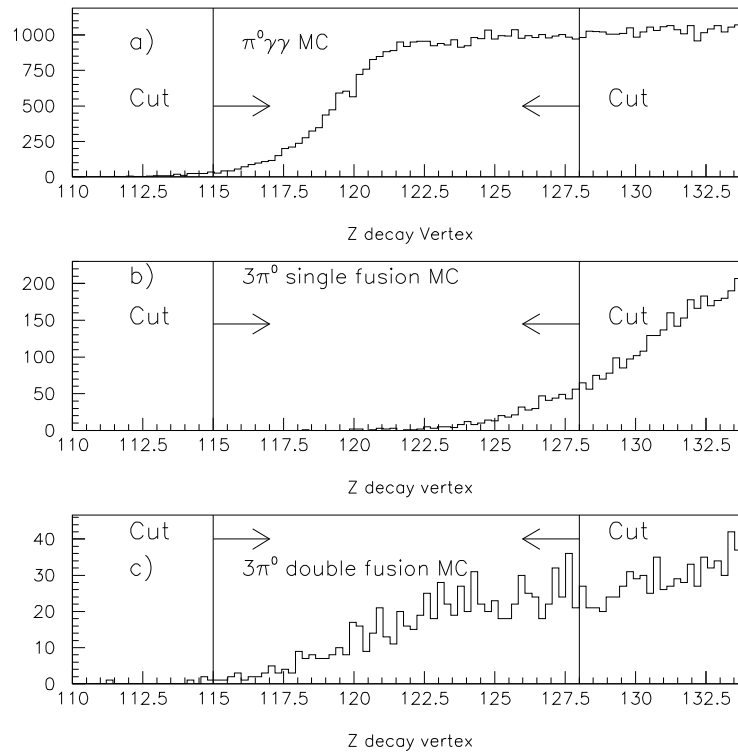


Figure 4.7: The Monte Carlo reconstructed Z vertex. a)  $\pi^0\gamma\gamma$ , b)  $3\pi^0$  single fusion and c)  $3\pi^0$  double fusion. Vertical lines and arrows show the accepted region. This cut rejects most of the  $3\pi^0$  single fusion events. The arrows indicate the accepted region.

#### 4.7 The photon veto cuts

The photon vetoes are very important in removing  $3\pi^0$  events which contain photons that miss the calorimeter.

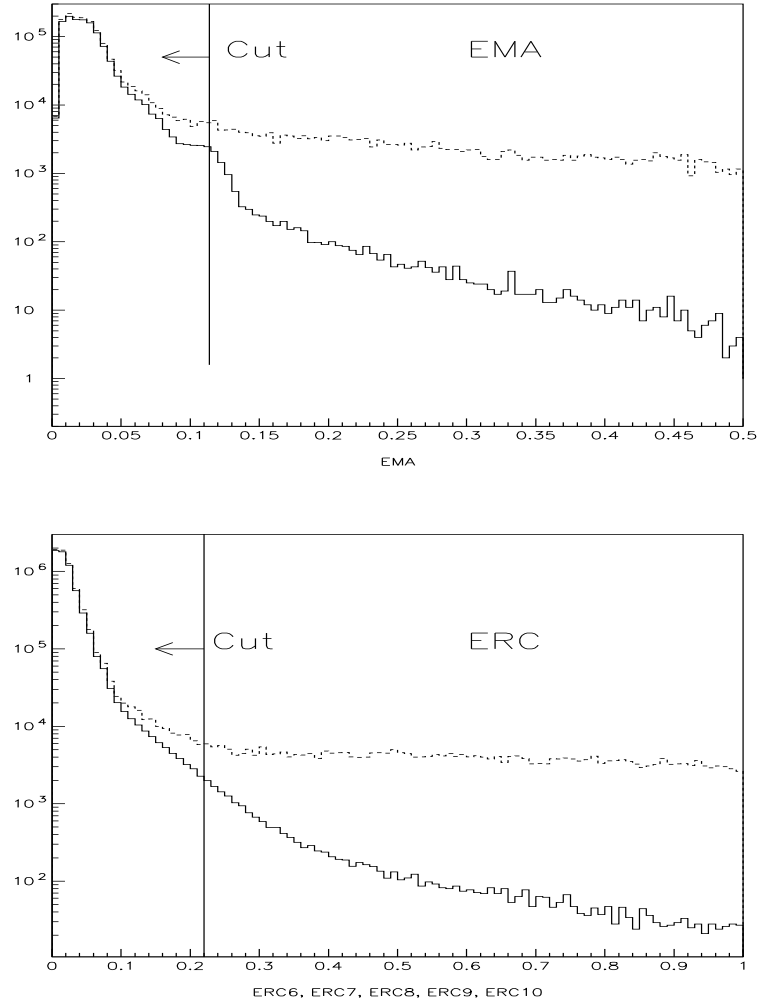


Figure 4.8: The photon veto cuts. The upper plot shows the energy in the Mask Anti, and the lower plot shows the minimum energy in any of the ring counters. The ring counters include ERC6, ERC7, ERC8, ERC9 and ERC10. The solid histogram is from  $2\pi^0$  events, and the dashed histogram is the scaled  $3\pi^0$  distribution. The vertical line indicates the position of the cut. The arrows indicate the accepted region.

We cut on the in-time energy for the ring counters, SA's and the CIA. The cuts on the ring counter energy (0.200 GeV) are looser than the cuts on the SA's and CIA (0.070 GeV) because of the higher activity due to the regenerator. The energy distributions for the various photon vetoes are shown in Figures 4.8-4.10.

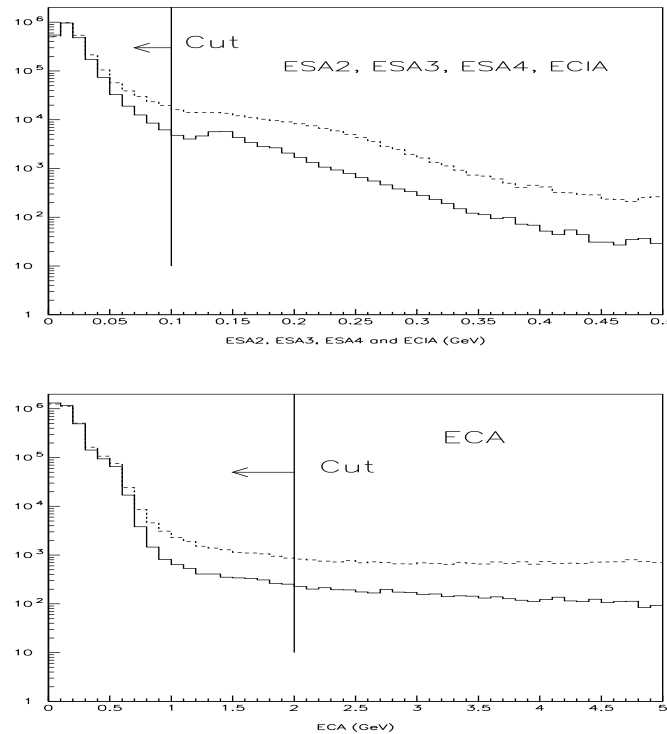


Figure 4.9: The energy in the photon vetoes. The upper plot is minimum energy in the Spectrometer Antis and CsI Anti, while the lower plot shows the Collar Anti. The Spectrometer Anti includes SA2, SA3, and SA4. The solid histogram is for  $2\pi^0$  events, and the dashed histogram is for the scaled  $3\pi^0$  distribution. The vertical line indicates the accepted region.

For a few runs in the 1996 data and for runs 9444-9665 in the 1997 data, cutting on the in-time energy in the mask is not very efficient. So we require that the mask trigger source bit be off in addition to an in-time energy requirement (0.080 GeV). For the BA we cut on the in-time energy for the maximum counter

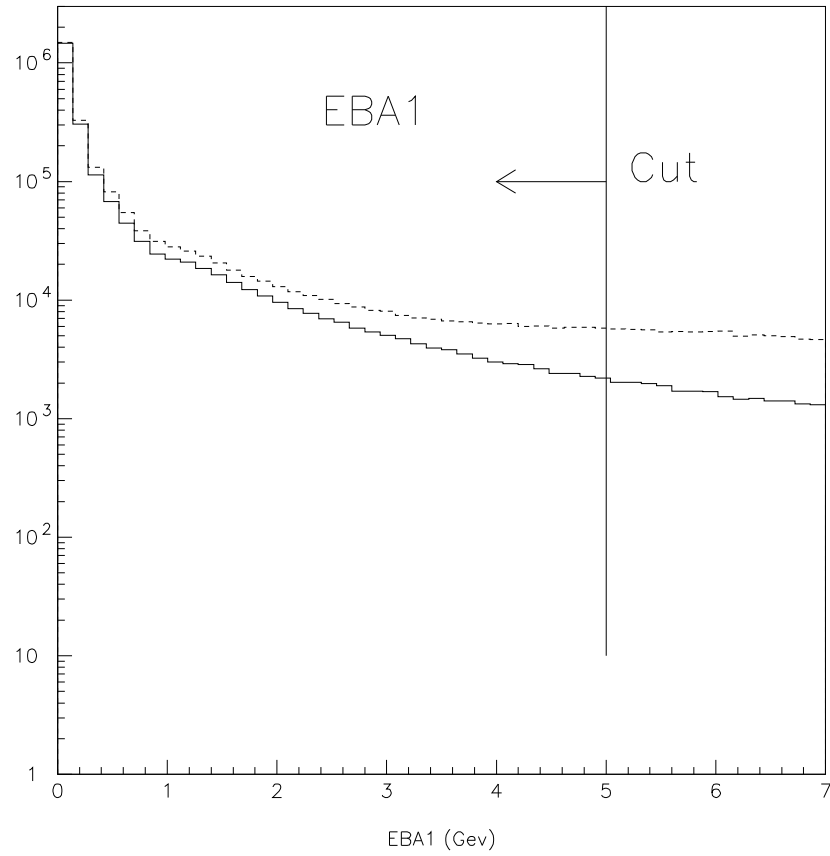


Figure 4.10: The energy in the BAs. The solid histogram is from  $2\pi^0$  events, and the dashed histogram is from scaled  $3\pi^0$  distribution. The vertical line indicates the position of the cut. The arrows indicate the accepted region.

plus its two neighbors. We require that this sum in BA1 be below 3 GeV for our event sample. For the CA we also use the in-time energy and cut at 1 GeV.

#### 4.8 The fusion shape $\chi^2$ cut

Figure 4.11 shows the  $M_{\gamma\gamma}$  mass distribution after all of the preceding cuts have been applied. As can be seen in the lower plot, the background is dominated by  $K_L \rightarrow \pi^0\pi^0\pi^0$  events. Most of these events come from either single or double fusion events, with the majority of the background due to double fusion events. The no-fusion and single fusion events are dramatically reduced by the cuts on  $Z$  and photon vetoes. The prominent peak at 0.270 GeV/c<sup>2</sup> (twice the  $\pi^0$  mass) is due to double fusion decays. However, much of the rest of the distribution is also due to double fusion decays where the  $\pi^0$  combination used two photons from different  $\pi^0$ s. The normalization between the Monte Carlo and the data is absolute after normalizing the Monte Carlo to the  $2\pi^0$  peak in the data.

To reduce the remaining background we define a shape  $\chi^2$  variable. This variable is calculated using the  $3 \times 3$  inner blocks of each cluster. For clusters located in the big block region this variable uses the 9 inner-most large blocks while for the small block region, it uses the 9 inner-most small blocks. At the boundary between big and small crystals, we take the crystals closest to the central block without regard to whether those crystals are large or small, *i.e.* we do not sum up four small blocks to be equivalent to a big block. The energy of each block is normalized and compared to the energy from a library of ideal showers. For an ideal photon,

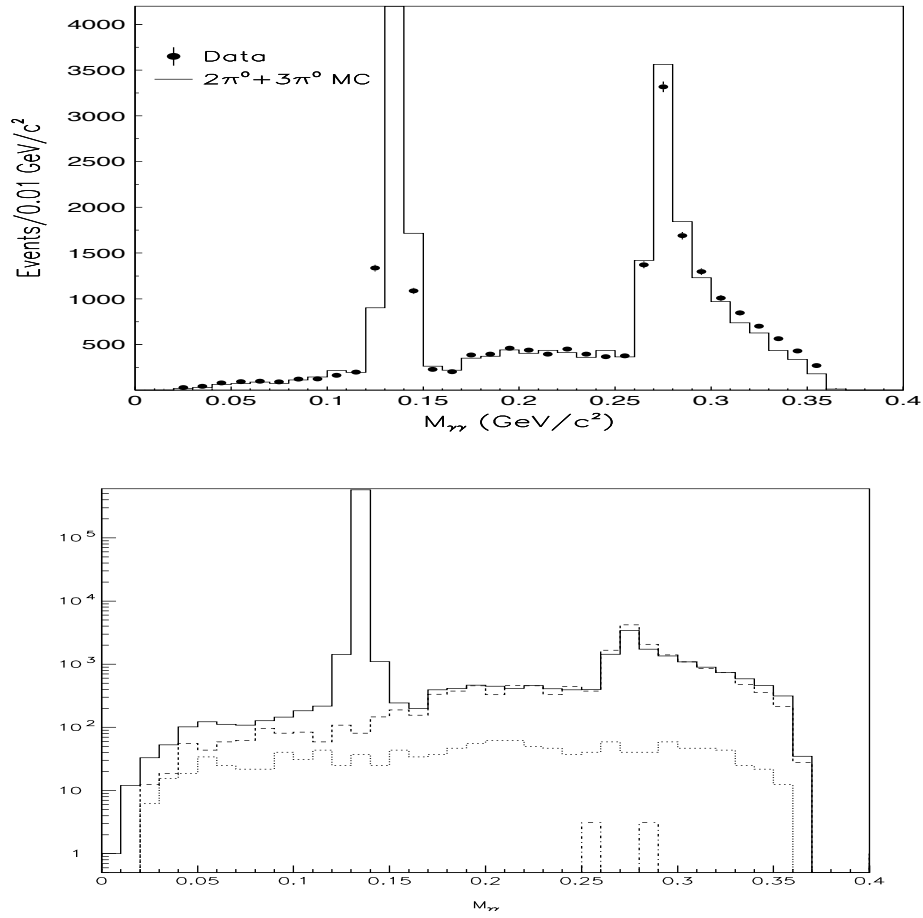


Figure 4.11: a) The two-photon invariant mass,  $M_{\gamma\gamma}$  after all cuts except for the photon shape cut. The dots are the combined 1996 and 1997 data and the histogram is the combined  $2\pi^0$  and  $3\pi^0$  Monte Carlo. b) The two-photon invariant mass,  $M_{\gamma\gamma}$  after all cuts except for the photon shape cut. The solid histogram represents the data. The dashed histogram is the Monte Carlo contribution from double fusions, the dotted histogram is from single fusions and the dot-dash histogram is from no-fusion events.

this shape  $\chi^2$  should be close to zero. For fused clusters, we expect this variable to be larger than one.

We require shape  $\chi^2 < 1.8$ . Figure 4.12 shows the shape  $\chi^2$  variable for all candidate events and for the  $3\pi^0$  background events. The cut on the shape  $\chi^2$  variable removes about 30% of our signal while reducing the background by a factor of about 50. This is the last cut applied to our data sample.

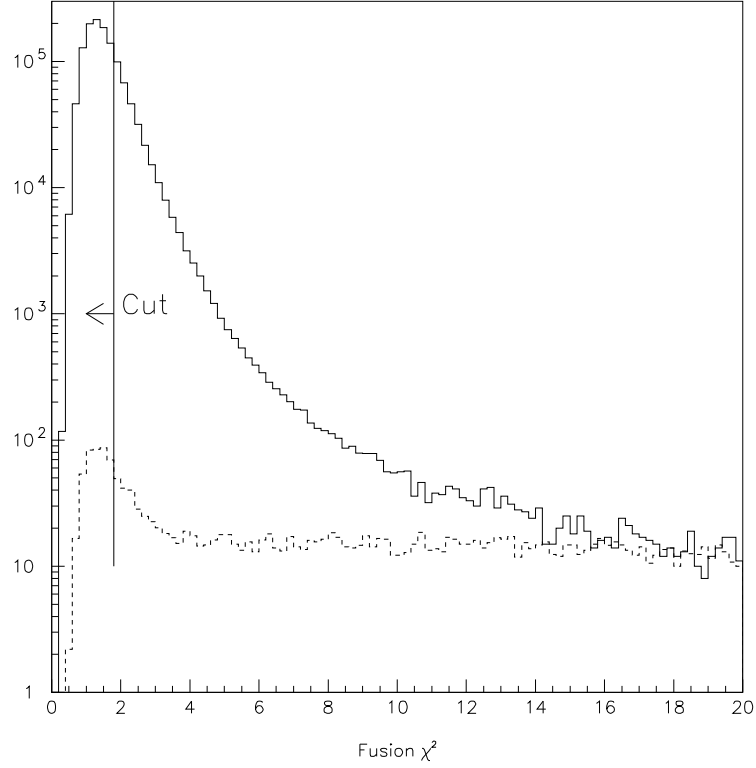


Figure 4.12: The fusion  $\chi^2$  variable for all events (histogram) and for the events outside the  $2\pi^0$  mass region (dashed). The variable is cut at 1.8. Vertical lines and arrows show the accepted region.

## 4.9 Estimation of the background level

After all cuts have been applied, we need to estimate the background level. We use the  $M_{\pi^0}$  mass distribution to estimate the level of background. We can also look at a number of other distributions to check our background estimation.

The remaining background consists mainly single and double fusion events, while the level of  $2\pi^0$  background events is small. The background distributions from single and double fusion events are very different. This can be seen in Figure 4.13 which shows the  $M_{\pi^0}$  and  $M_{\gamma\gamma}$  distributions for single and double fusion events, separately. In Figure 4.13 the correct combination corresponds to events where the two photons used to reconstruct  $M_{\pi^0}$  were both from the same  $\pi^0$ . The wrong combination used two photons originating from two different  $\pi^0$  decays. One can see that the double fusion events from the correct combination peak near the  $\pi^0$  mass in the  $M_{\pi^0}$  distribution.

To verify the  $3\pi^0$  background level, we fit the  $M_{\pi^0}$  data distribution to the sum of the signal plus background Monte Carlos. The result of this fit can be seen in Figure 4.14. One can see that the tails of the mass distribution seem to agree fairly well with the Monte Carlo. The number of  $3\pi^0$  events that result from the fit is consistent with our background expectation using an absolute normalization. To find the absolute normalization, we just scale the  $3\pi^0$  events by the ratio of branching ratios of  $2\pi^0$  to  $3\pi^0$  decays, and the  $2\pi^0$  events are scaled to the  $\pi^0$  peak in the  $M_{\gamma\gamma}$  distribution.

The background estimated in the low mass  $M_{\gamma\gamma}$  region ( $M_{\gamma\gamma} < 0.240$  GeV/ $c^2$ ) is important because this mass region has a significant impact on the

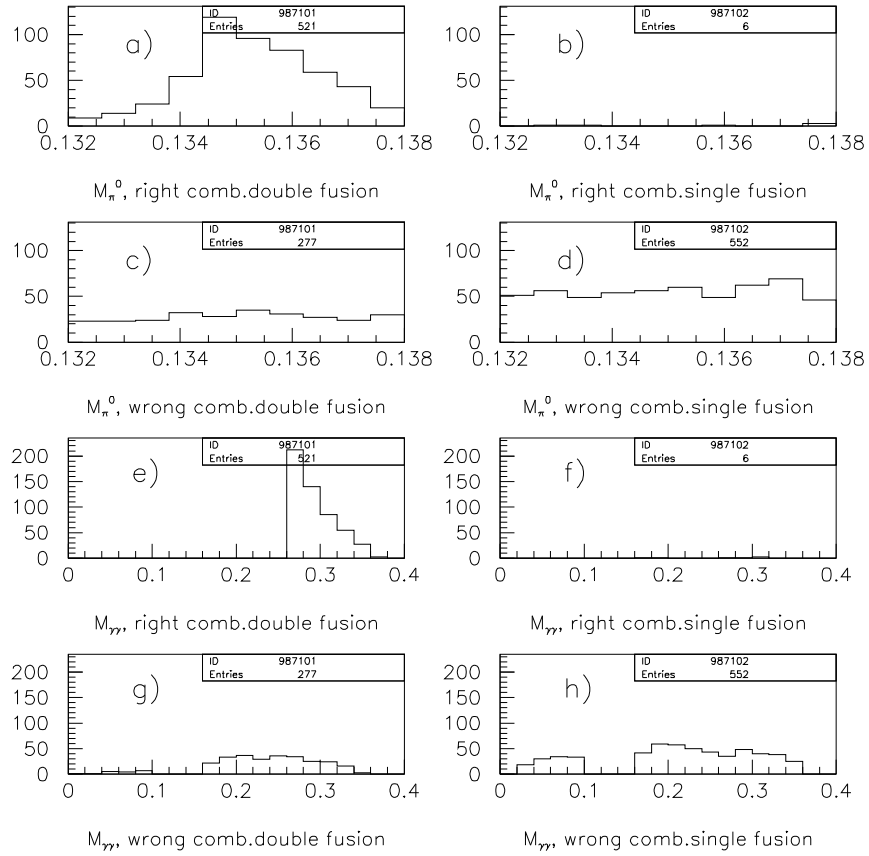


Figure 4.13:  $M_{\pi^0}$  and  $M_{\gamma\gamma}$  distributions for single and double fusion  $3\pi^0$  Monte Carlo events. The left plots are from double fusion, and the right side is the single fusion. The top 4 plots are  $M_{\pi^0}$  distribution, and the bottom 4 plots are  $M_{\gamma\gamma}$ . Plot e) shows that double fusion events with the correct combination (2 photons are from the same  $\pi^0$  in the event reconstruction) do not contribute to the low mass tail of  $M_{\gamma\gamma}$ .

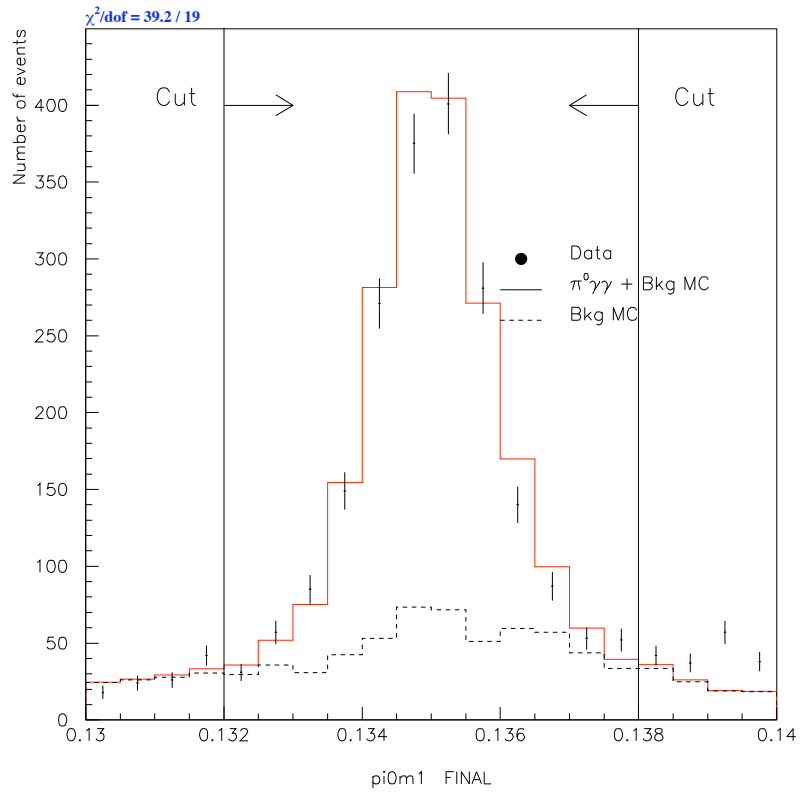


Figure 4.14:  $M_{\pi^0}$  distribution after all cuts. The dots are data. The solid histogram is  $3\pi^0$  and  $\pi^0\gamma\gamma$  Monte Carlo, the dashed histogram (red) is  $3\pi^0$  background MC. Vertical lines and arrows show the accepted region.

determination of  $a_V$ . Since it was not obvious that the Monte Carlo correctly predicted the ratio of the single to double fusion events, we fit the low mass region in two different ways. In the first method, we assumed that the ratio of single to double events was correct. With this fit, we found 72 single fusion events and 160 double fusion, with a C.L. of 72%. For the second fit, we allow the ratio of single to double fusion events to float. In this fit, we find 140 single fusion and 98 double fusion events, with a C.L. of 90%. The total background level in the low mass region does not change, but shape of  $M_{\pi^0}$  changes. We use the difference between these two results in our systematic error when we fit for  $a_V$ . The results of these two fits is shown in Figure 4.15.

After all cuts, we find the total  $3\pi^0$  background level is 30%. This background is about equally divided between double and single fusion events.

Table 4.1: Comparison of  $2\pi^0$  and  $3\pi^0$  acceptance with each cut

Cuts	$2\pi^0$ acceptance	$3\pi^0$ acceptance
NHIT	0.6789	0.5673
NSOFT	0.9993	0.9636
EK	0.9374	0.9161
EPHOT	0.9678	0.9936
ZDK	0.5834	0.1899
MA SR	0.9962	0.5559
ERC	0.9755	0.8406
ESA	0.9889	0.9810
ECA	0.9976	0.9793
EMA	0.9881	0.8808
EBA	0.9450	0.8839
Vacuum win	0.9968	0.9508
Fusion $\chi^2$	0.8129	0.0614

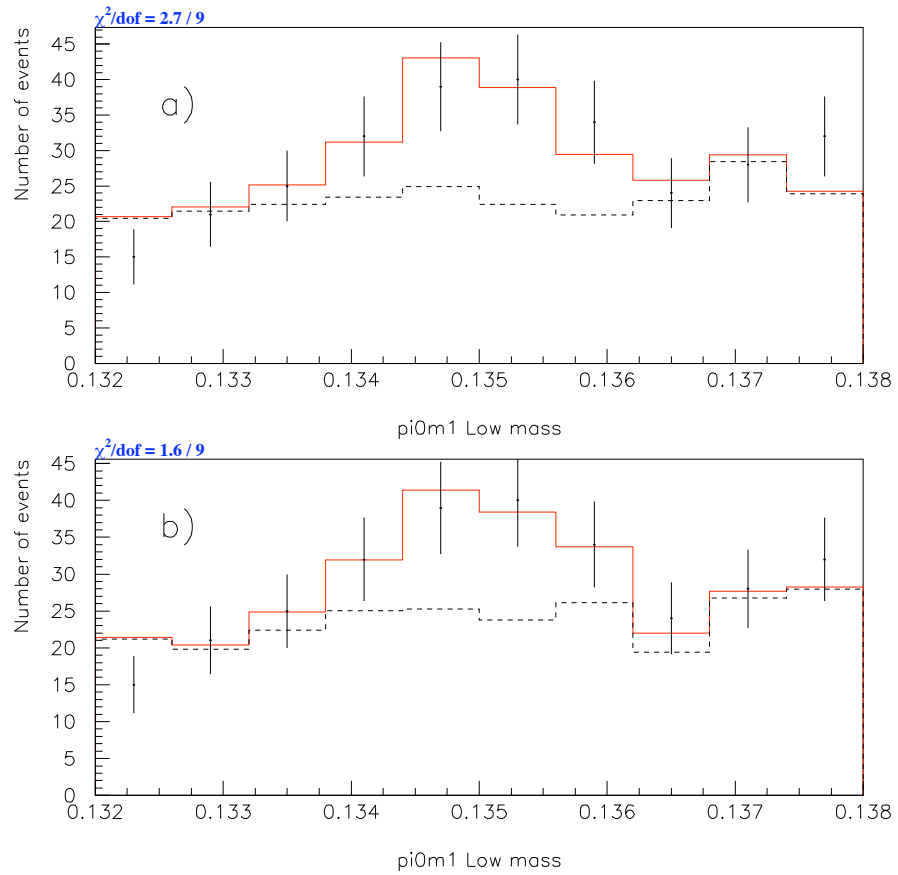


Figure 4.15:  $M_{\pi^0}$  distribution of low mass tail, the histogram is  $3\pi^0$  plus  $\pi^0\gamma\gamma$  MC, the dots are the data, the dash line is the  $3\pi^0$  background. a) default  $3\pi^0$  b) separate single fusion and double fusion.

Table 4.2:  $K_L \rightarrow \pi^0 \gamma \gamma$  Efficiencies

Cut	Efficiency	Number of non- $2\pi^0$ Events
Level 1	0.124	
Level 2	0.773	
Level 3	0.472	$92.3 \times 10^6$
ABS(Y center of energy) < 0.05 m	0.992	$87.3 \times 10^6$
LREGOK	0.946	$76.9 \times 10^6$
ABS( $M_{\pi^0} - 0.135$ ) < 0.003 GeV/c <sup>2</sup>	0.979	$46.2 \times 10^6$
Z < 134 m	0.605	$1.16 \times 10^6$
No events with two $\pi^0$ s	0.973	763958
NHIT (in-time) < 23	0.652	588415
No software clusters	1.000	568613
40 GeV < E < 160 GeV	0.955	521657
$E_{\text{clus}} > 2.0$ GeV	0.989	518283
115 m < Z < 128 m	0.579	96580
MA source bit OFF	1.000	54054
$E_{\text{RC}} < 0.22$ GeV	0.988	48300
$E_{\text{SA}} < 0.1$ GeV	0.995	47633
$E_{\text{CA}} < 2.0$ GeV	0.999	46767
$E_{\text{MA}} < 0.114$ GeV	0.998	39782
$E_{\text{BA1}} < 5.0$ GeV	0.929	36869
Cut on Vacuum window interactions	0.985	34968
Shape $\chi^2 < 1.8$	0.708	1982

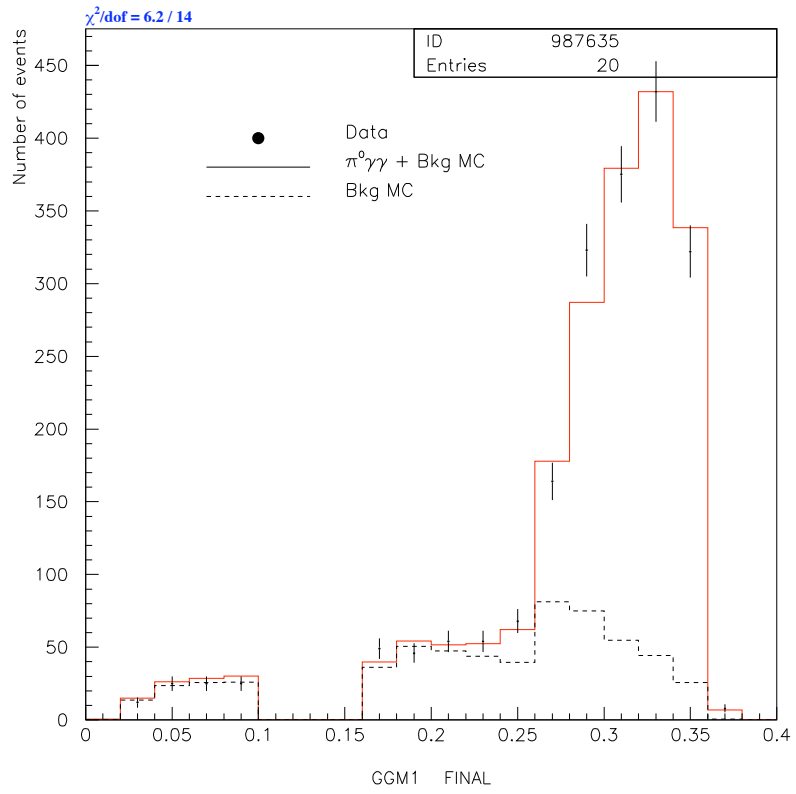


Figure 4.16: Final  $M_{\gamma\gamma}$  distribution after all cuts applied. The dot is data, the histogram is  $\pi^0\gamma\gamma$  and  $3\pi^0$  MC. The dash line is  $3\pi^0$  background MC. The background at the tail part is very high.

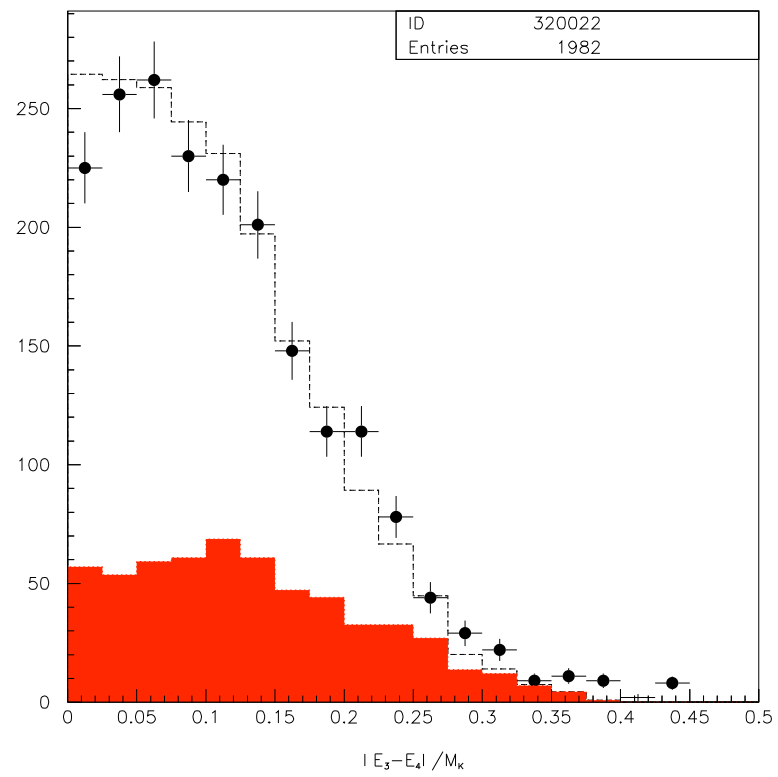


Figure 4.17: Y dalitz after all cuts. The dots are the data. The solid histogram is the sum of the  $3\pi^0$  and  $\pi^0\gamma\gamma$  Monte Carlo, the dark histogram (red) is  $3\pi^0$  background MC

#### 4.10 Final data sample

The cuts used to reduce the  $K_L \rightarrow \pi^0\pi^0\pi^0$  background can be seen in Table 4.1. As one can see, the cuts on the decay vertex and the shape  $\chi^2$  variables are the most effective at removing  $K_L \rightarrow \pi^0\pi^0\pi^0$  events. The cut on the RC energies also helps to remove some of this background, while the cut on the Mask Anti helps to significantly reduce  $3\pi^0$  decays upstream of the regenerator. The ring counter cut, mask anti source cut and Z vertex cut reduce single fusion  $3\pi^0$  background, while fusion  $3\pi^0$  removes mostly double fusion  $3\pi^0$  background. The efficiency for these cuts for  $K_L \rightarrow \pi^0\pi^0$  events is quite high. This is good since the  $K_L \rightarrow \pi^0\pi^0$  events have a similar topology to the  $K_L \rightarrow \pi^0\gamma\gamma$  events.

Table 4.2 lists all of the cuts used in this analysis. The second column lists the signal efficiency while the third column lists the number of events in the data outside of the  $K_L \rightarrow \pi^0\pi^0$  mass window. Much of the loss in signal at Level 1 is due to events that decay upstream of the mask. The acceptance loss in Level 2 results from events in which fewer than four photons hit the calorimeter and from events in which one or more photons are below the HCC threshold. In Level 3, the largest acceptance loss is due to the cut on  $Z$  at 141 m. Aside from the tight cut on shape  $\chi^2$  and the decay vertex, the largest acceptance loss in our analysis cuts comes from the cut on extra in-time drift chamber hits. While the mean number of drift chamber hits is below 10, the distribution has a long tail that extends to over 100 hits per event. However, the Monte Carlo reproduces the drift chamber hit distribution reasonably well as shown in Figure 4.1.

After applying all of the above cuts, the final  $M_{\gamma\gamma}$  mass distribution is shown

in Figure 4.16. In this figure the circles are the data and the histogram is the sum of the  $\pi^0\gamma\gamma$ , and  $3\pi^0$  Monte Carlo. The contribution from the background Monte Carlo is shown as the dashed histogram. The total number of events is  $1982 \pm 45$  over a background of  $601 \pm 25$   $3\pi^0$  events and  $5 \pm 3$   $2\pi^0$  events. The number of  $\pi^0\gamma\gamma$  events is  $1381 \pm 37$ . The good data/Monte Carlo agreement indicates that the background is understood. Figure 4.17 shows the  $Y_{Dalitz}$  distribution after all cuts. This plot also shows good agreement between the data and the Monte Carlo. This distribution will be used in our fits for  $a_V$ .

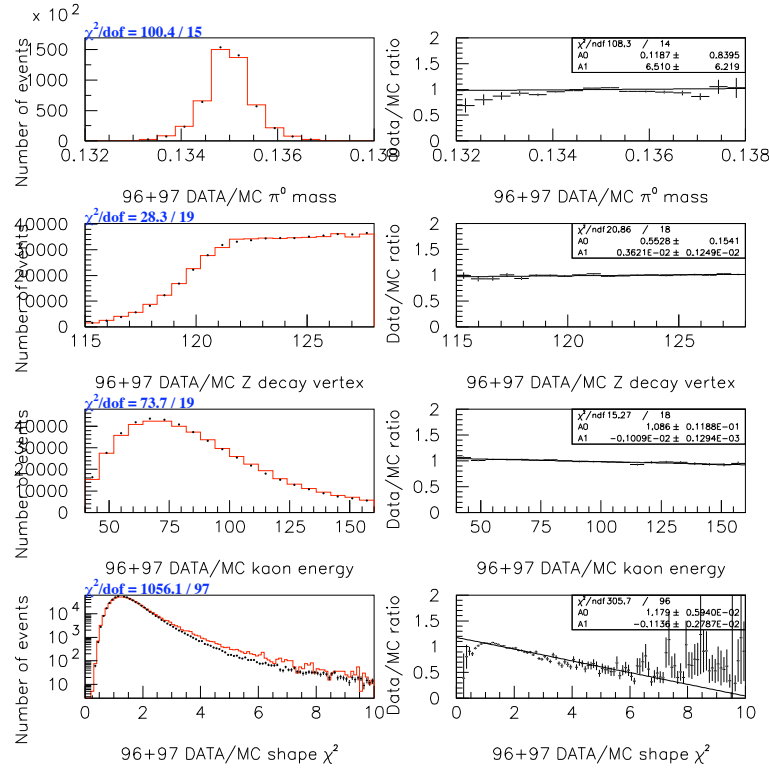


Figure 4.18: The comparison of 96+97 data to Monte Carlo. The plot shows  $2\pi^0$  Z decay vertex, kaon energy,  $\pi^0$  mass, and shape  $\chi^2$  Data/MC overlay. The right side plots are the two histograms ratio. The dot is data, and the histogram is  $2\pi^0$  MC.

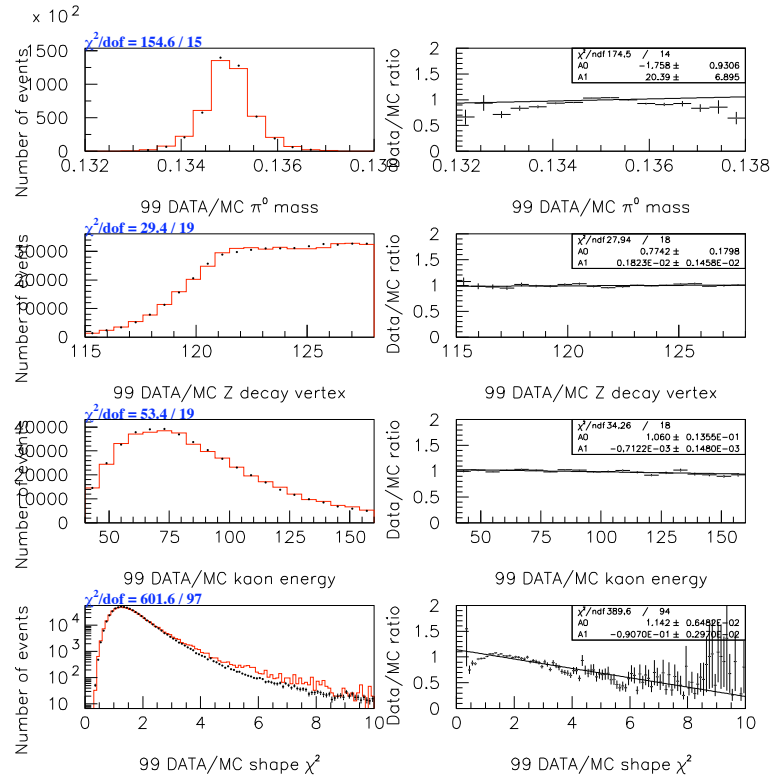


Figure 4.19: The comparison of 99 data to Monte Carlo. The plot shows  $2\pi^0$  Z decay vertex, kaon energy,  $\pi^0$  mass, and shape  $\chi^2$  Data/MC overlay. The right side plots are the two histograms ratio. The dot is data, and the histogram is  $2\pi^0$  MC.

Figure 4.18 (96 + 97) and figure 4.19 (99) show the  $Z$  decay vertex, the kaon energy,  $\pi^0$  mass, and shape  $\chi^2$  with the Monte Carlo overlaid with the data. The  $Z$  distribution is important since good agreement indicates that the calculation of the acceptance using the Monte Carlo will be reliable. In addition, the good agreement between data and Monte Carlo in Figure 4.20 (96 + 97) and figure 4.21 (99) are further evidence that the acceptance calculation using the Monte Carlo can be trusted.

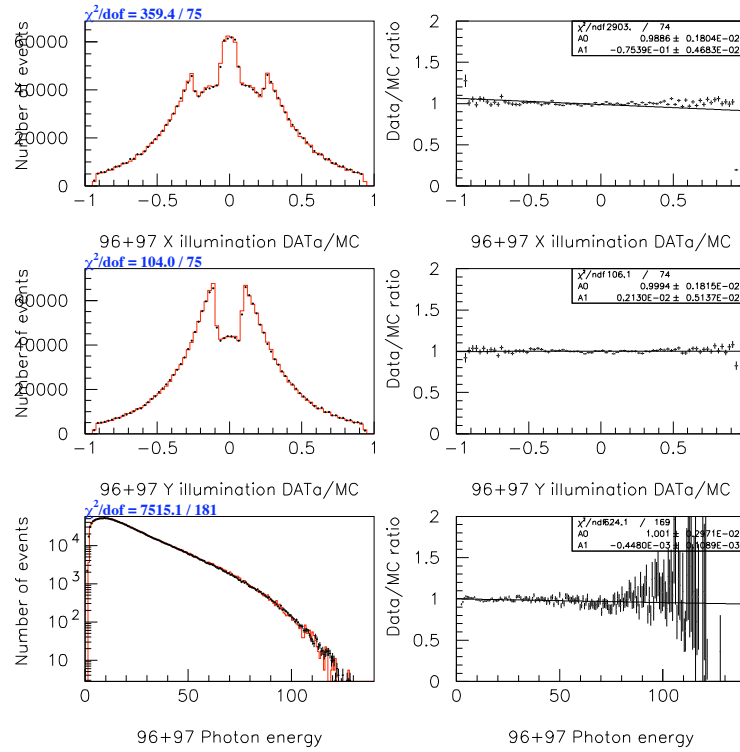


Figure 4.20: The comparison of 96 + 97 data to Monte Carlo. The plot shows  $2\pi^0$  photon energy, x illumination y illumination Data/MC overlay. The right side plots are the two histograms ratio. The dot is data, and the histogram is  $2\pi^0$  MC.

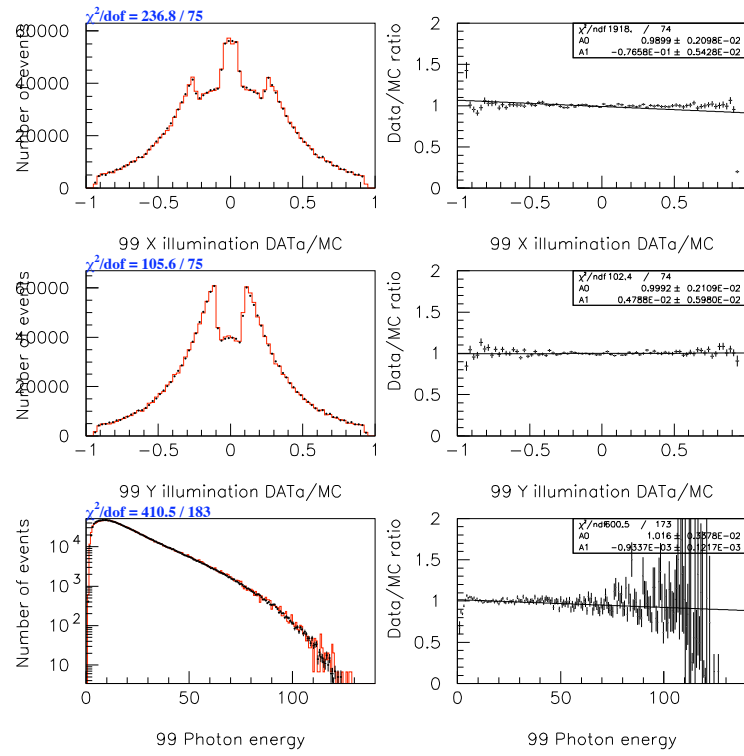


Figure 4.21: The comparison of 99 data to Monte Carlo. The plot shows  $2\pi^0$  photon energy, x illumination y illumination Data/MC overlay. The right side plots are the two histograms ratio. The dot is data, and the histogram is  $2\pi^0$  MC.

## CHAPTER 5

### MONTE CARLO SIMULATION

There are two reasons that we must do Monte Carlo simulation. First, we need to determine the acceptance for the signal and normalization modes. The ratio of these two acceptances is used to determine the branching ratio for  $K_L \rightarrow \pi^0 \gamma \gamma$ . Second, we need understand the background. This is done by fully simulating the decays expected to contribute to the background. In this chapter we will discuss the simulation of the kaon production, the kaon transport, the detectors, and  $K_L \rightarrow \pi^0 \gamma \gamma$  simulation. Then we will discuss what we did to improve default Monte Carlo to understand the  $3\pi^0$  background.

#### 5.1 General monte carlo simulation

The initial position of the kaon in the target was based on the proton interaction length in the BeO target and on the shape of the primary beam. The latter was used to determine the transverse position of the kaon in the target. The position and geometry of the absorbers and collimators were obtained from survey measurements. Both absorption and scattering in the absorbers were simulated.

The  $K^0$  or  $\overline{K}^0$  was generated at the BeO target, and evolved through the KTeV beam line. The kaon decay position is chosen to be between 90 m and 160 m downstream of the target. The full kaon amplitude is evolved through all of

the material in the detector and then allowed to decay at the appropriate location. Since the kaon energy range is between 20 GeV to 200 GeV, the state of the kaon is almost completely  $K_L$  in the vacuum beam. The decay  $z$  range and the initial kaon energy range are customized by the user when the Monte Carlo is generated.

Each type of kaon decay has a different decay generator. The neutral decay  $K \rightarrow \pi^0 \pi^0$  forces the  $\pi^0$  to decay immediately, either to  $\gamma\gamma$  or possibly to the Dalitz  $e^+e^-\gamma$  with full radiative corrections, or to other rare decay modes. After the decay mode is determined, the daughter particles are transformed to the lab frame and traced.

The kaon decay products are traced through the detector until they interact with some component of the detector. For photons the particles are just traced in a straight line until they encounter a detector element, or the particle escapes the fiducial volume of the detector. Particles that pass through the beam holes of the CsI detector are considered to be lost and are no longer traced. The pair-production of photons is simulated throughout the spectrometer region and the trigger counters. For charged particles scattering and bremsstrahlung is also simulated. The interactions of particles that strike the photon vetoes or trigger counters are simulated and the resulting energy depositions are digitized and stored.

## 5.2 The simulation of the CsI calorimeter

The simulation of the calorimeter includes describing the deposition of energy in the calorimeter, the conversion of the energy to charge by the photomultiplier tubes, and the digitization of the charge. To simulate electrons and photons in the calorimeter we used a shower library rather than fully simulating each interaction during the

Monte Carlo generation. There were two libraries: one for electrons and one for photons.

The showers in the libraries were generated by using the GEANT simulation package. For the shower library each shower was generated over a  $13 \times 13$  ( $32.5 \text{ cm} \times 32.5 \text{ cm}$ ) small block region and was generated in six logarithmic energy bins (2, 4, 8, 16, 32, and 64 GeV). In addition we divided the face of the central block into eight octants and generated showers uniformly across one of the octants. The octant was binned into 325  $500 \times 500 \mu\text{m}^2$  position bins. Five showers were generated for each position and energy bin for a total of 9750 showers in each of the two libraries. The GEANT showers were segmented in z direction.

In the Monte Carlo, when a photon hit the CsI calorimeter, the appropriate shower was picked from the library based upon its position and energy. Because of resolution effects in data, the energy of incoming particles was smeared to match the data. The amount of smearing is determined by the incoming particle energy. The shower was then transformed into the correct octant of the crystal, and the energy of the shower was rescaled to match the smeared energy of the photon. The longitudinal energy of each block was convoluted with the measured longitudinal response of each crystal, and the total energy in the appropriate crystals was incremented. The total energy in the calorimeter was stored to be used as the  $E_{tot}$  signal at Level 1.

After all particles have been traced, digitization of the crystals was simulated. The appropriate gain and pedestal constants were determined for each crystal, and a digitized signal for each crystal was simulated. At this point, the HCC bits for the Level 2 simulation were generated based upon the measured HCC

thresholds. The readout threshold for the calorimeter was also simulated and any block that exceeded the digitization threshold was written to the output stream.

### 5.3 Trigger simulation

A full simulation of the KTeV trigger was performed by our Monte Carlo. This simulation included all three levels of the trigger. To simulate the Level 1 and Level 2 triggers all of the input sources were generated and the appropriate lookup tables were used. The Level 1 and Level 2 trigger maps were identical to those used online in the hardware. For Level 3 the same code used by the online system was run during the Monte Carlo simulation, and all of the trigger words and Level 3 tags were written into the output stream. This ensures that the trigger definition is the same for the data and the Monte Carlo.

### 5.4 Accidental overlay

Because of the high rate of activity in the target, accidental activity in the form of neutrons and other neutral particles could be present in the KTeV detector. Until now, we have only discussed the particles or photons produced by the  $K_L$  decays. The other particles besides kaons produced at the target, and byproducts from their interactions and decays can lead to accidental activity in the detectors. This activity can cause the mismeasurement of cluster energies, or can fire some of the trigger sources.

We recorded accidental events using a specialized trigger during the experiment. This trigger consisted of a scintillator hodoscope that pointed at the KTeV

target, but was outside of the detector volume. The trigger rate from this apparatus scaled with the beam intensity. We recorded accidental events throughout the KTeV running and used them to overlay on top of Monte Carlo events to simulate the effects of accidental activity.

After the particles were traced in the KTeV Monte Carlo, but before the event was digitized, accidental activity was added to each event. Since accidental events can cause inefficient triggers, the overlay activity was added before evaluation of any trigger sources. The total event was then digitized, including both the simulated activity and the accidental activity. The Level 1 latches from the accidental activity were OR'd with the latches from the simulated data.

To ensure that we properly simulated the correct level of accidental activity, we overlaid the accidentals on a run-by-run basis. The number of events to generate for each run was determined by counting the number of reconstructed  $K_L \rightarrow \pi^0 \pi^0$  events. From these numbers we generated a text file containing the weight for each run, which was read in at the initialization stage of the Monte Carlo.

## 5.5 $K_L \rightarrow \pi^0 \gamma \gamma$ Monte Carlo

There are two contributions to the decay  $K_L \rightarrow \pi^0 \gamma \gamma$ : Pion-loop  $K_L \rightarrow \pi^0 \pi^+ \pi^- \rightarrow \pi^0 \gamma \gamma$ , and vector meson exchange  $K_L \rightarrow \rho \gamma \rightarrow \pi^0 \gamma \gamma$  or  $K_L \rightarrow \omega \gamma \rightarrow \pi^0 \gamma \gamma$ . The contribution of the vector meson exchange terms is characterized by the parameter  $a_V$ . The low mass tail of  $M_{\gamma\gamma}$  depends upon on the  $a_V$  in the signal MC. Nominally  $O(P^4)$  has no tail. For  $a_V=0$  there is a very small tail while for  $a_V=-0.9$  there is a large tail. Since the acceptance does not vary too much with changes in  $a_V$ , a different value of  $a_V$  will not affect the  $K_L \rightarrow \pi^0 \gamma \gamma$  branching

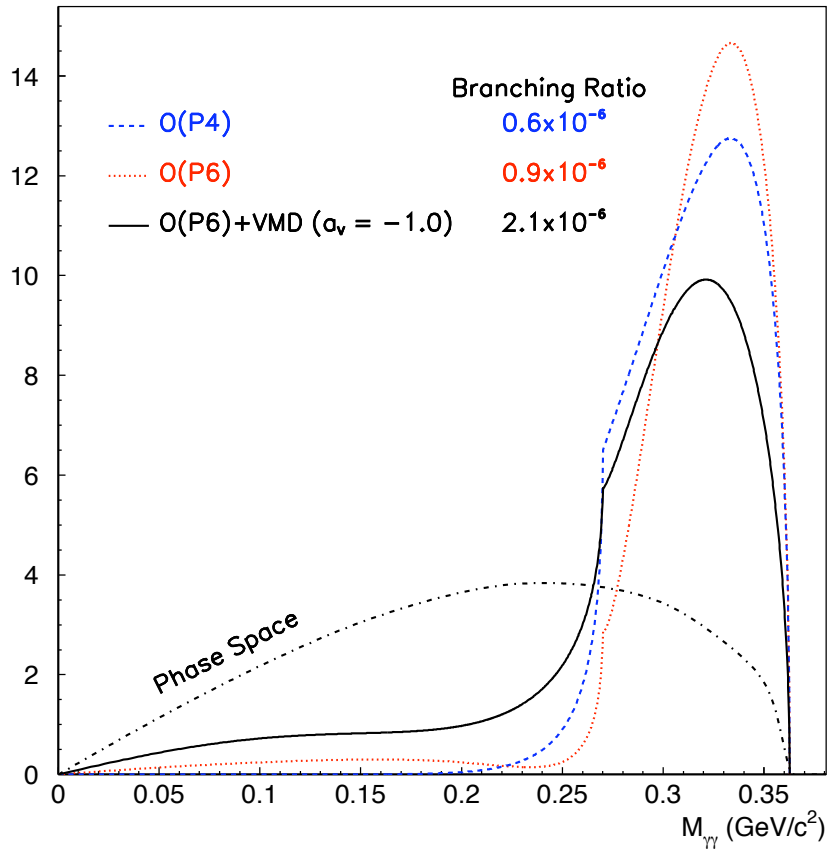


Figure 5.1: ChPT prediction of the  $M_{\gamma\gamma}$  distribution.

ratio measurement. However, it does have an impact on the parameters  $Z_{Dalitz}$  and  $Y_{Dalitz}$ . The  $O(P^4)$  theory prediction is the blue dash line on the Figure 5.1, and the dotted line is the  $O(P^6)$  without the vector meson exchange.

The Monte Carlo implemented two different generators sent to us by their authors: 1) F. Gabbiani and 2) D'Ambrosio and Portoles. We chose which generator to use at the Monte Carlo initialization time. To first approximation the result obtained was the same from each of the generators. These generators calculated the  $K_L \rightarrow \pi^0 \gamma \gamma$  matrix element as a function of the parameter  $a_V$ . The Monte Carlo used this matrix element to calculate the weight of a given event as a function of  $Z_{Dalitz}$  and  $Y_{Dalitz}$ . The matrix element took the form:

$$F(Y, Z) = \frac{\partial BR(K_L \rightarrow \pi^0 \gamma \gamma)}{\partial Z \partial Y}(Y, Z) \quad (5.1)$$

To generate an event, the value of  $Z_{Dalitz}$  was randomly chosen from a flat distribution, and  $Y_{Dalitz}$  was chosen between zero and its kinematic limit. The weight of the event was determined from the above matrix element. Then a random number was chosen between zero and a predetermined maximum. If this random number exceeded the calculated event weight, the generation was continued. Otherwise, new values of  $Z$  and  $Y$  were chosen, and the process continued until an event could be selected. The solid line in Figure 5.1 shows the  $M_{\gamma\gamma}$  distribution predicted by ChPT  $O(P^6)$  with the vector meson exchange  $a_V=-0.1$

Based upon the values of  $Z_{Dalitz}$  and  $Y_{Dalitz}$ , the energies of the  $\pi^0$  and the two photons could be determined. The daughter particles were then boosted to the lab frame, and in the case of the  $\pi^0$  were decayed into a  $\gamma\gamma$  pair. The final state particles were then traced according to the prescription above.

## 5.6 Simulation of the fusion $\chi^2$ variable

In our analysis the reduction of the  $K_L \rightarrow \pi^0\pi^0\pi^0$  background depends crucially on the  $\chi^2$  cut. This can be seen in Figure 5.2, which shows the shape  $\chi^2$  distribution for both data and the  $K_L \rightarrow \pi^0\pi^0\pi^0$  background Monte Carlo. This plot was taken from our combined 1996 and 1997 publication [2]. As can be seen, the Monte Carlo matches the data at large values of shape  $\chi^2$ . The excess above the Monte Carlo at low values corresponds to the  $K_L \rightarrow \pi^0\gamma\gamma$  signal. The main issue is whether or not the background Monte Carlo correctly predicts the shape of the  $\chi^2$  distribution at small values of shape  $\chi^2$ .

We found that the default shower library was unable to correctly reproduce the  $\chi^2$  distribution. This can be seen in Figure 5.3. In the top plot, we compare the shape  $\chi^2$  distribution of  $K_L \rightarrow \pi^0\pi^0$  data and Monte Carlo. As can be seen, there is a clear mismatch, especially around two, which is where we apply our cut. For  $2\pi^0$ , if the shape  $\chi^2$  is cut at 2.0, data acceptance is 82%, while Monte carlo acceptance is only 72%. This implies that the  $3\pi^0$  background level is underestimated by our Monte Carlo.

We do not know the exact cause of this mismatch. However, one possible explanation is that the Monte Carlo does not take into consideration the incident angle of the photon. All showers were generated with a fixed angle with respect to the face of the crystals. In principle, we could have used GEANT to generate each event, instead of using a shower library. However, the CPU time required for this would have been prohibitively high. Since we needed to generate billions of background events, this could not have been done in a reasonable amount of time.

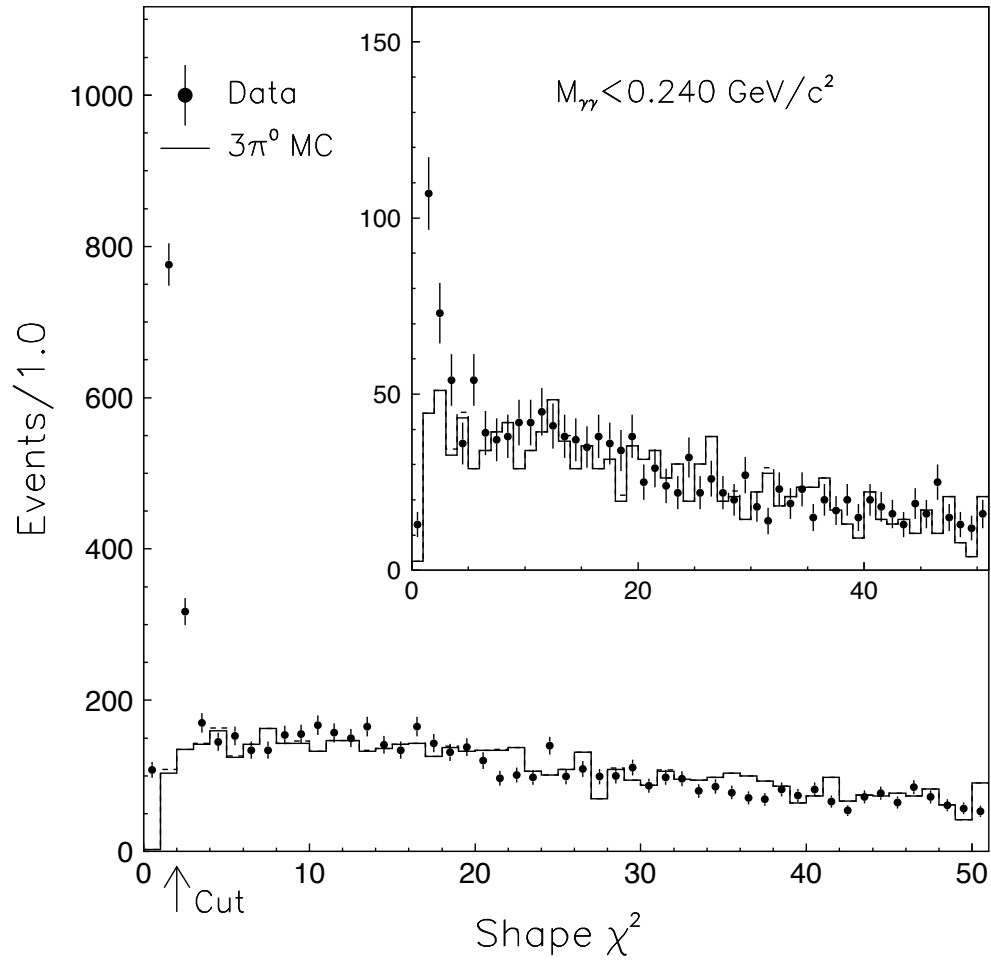


Figure 5.2: The fusion  $\chi^2$  variable after cuts. The dots are the data and the histogram is the  $3\pi^0$  Monte Carlo. the insert shows the same distribution for the low mass tail of  $M_{\gamma\gamma} < 0.240 \text{ GeV}/c^2$ .

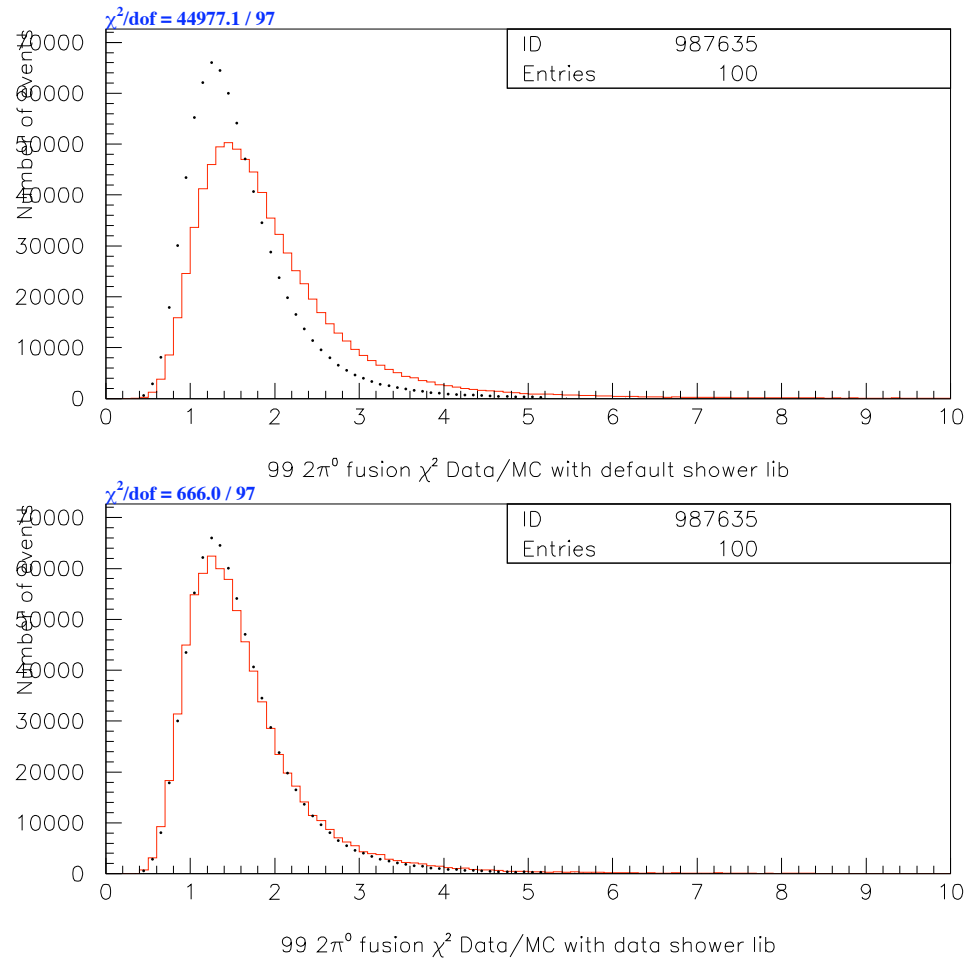


Figure 5.3: Data to MC comparison of fusion  $\chi^2$  for the data from 1999. the upper is with The default shower library was used from Monte Carlo in the upper plot, while the data shower library was used for the lower.

## 5.7 Data shower library

To improve the simulation of the shape  $\chi^2$ , we decided to use showers from the data. Using low intensity runs, we stripped off showers from  $K_L \rightarrow \pi^0\pi^0$  and  $K_L \rightarrow \pi^+e^-\nu$  events. These showers were taken only from the small block region and were required to be away from the beam holes. The showers were binned using the same position and energy binning as the default GEANT-based shower library. However, for obvious reasons, these showers were not segmented longitudinally. So, when a photon is simulated with these showers, we just determine the correct shower from the data shower library and add the energy from the library to the appropriate crystal. Accidental effects are handled the same as in the default Monte Carlo.

When the data shower library is used, the fusion  $\chi^2$  simulation is improved. The bottom plot of Figure 5.3 shows that the  $K_L \rightarrow 2\pi^0$  fusion  $\chi^2$  Monte Carlo matches the data well, especially over the small range, when the shape  $\chi^2$  is less than 1.8. While the main goal of improving the shape  $\chi^2$  was achieved using the data shower library, we found that the agreement between data and Monte Carlo for other variables got considerably worse. For example, the  $\pi^0$  mass resolution for the data shower library Monte Carlo was considerably worse than the data. This was probably due to the fact that we had not properly calibrated the data shower library Monte Carlo. As noted above, when a photon is simulated the energy is smeared before the shower library lookup is performed. This smearing function was tuned for the default shower library, but not for the data shower library.

The default Monte Carlo shower library matches the data very well in almost every

aspect, except for the shape  $\chi^2$ . So, rather than spend a significant time trying to recalibrate the data shower library Monte Carlo, we decided to use both the default shower library and the data shower library in our simulation. For each event, we stored the energies of each block determined both by the default and the data shower libraries. During reconstruction the clustering algorithm was performed on both arrays of energies, and the resulting photon variables were stored for both sets of showers. For all energy and position measurements, we used the default shower library. But, for the determination of the shape  $\chi^2$ , we used the data shower library.

## 5.8 Verification of the data shower library

As can be seen in the top plot of Figure 5.4, the shape  $\chi^2$  distribution for  $K_L \rightarrow \pi^0\pi^0\pi^0$  events is significantly different with the data shower library Monte Carlo. The new Monte Carlo produces a hump around 1.2 for the  $K_L \rightarrow \pi^0\pi^0\pi^0$ . Recall that the default Monte Carlo shows a slightly falling distribution for the shape  $\chi^2$  at small values. This hump increases the amount of background from  $K_L \rightarrow \pi^0\pi^0\pi^0$  events in our signal region by a significant amount, approximately a factor of two.

Since the shape  $\chi^2$  variable matches the  $K_L \rightarrow \pi^0\pi^0$  data well, we expect that it should match the  $K_L \rightarrow \pi^0\pi^0\pi^0$  data also. To check the shape of the  $\chi^2$  distribution from the data shower library Monte Carlo, we used a reweighting procedure. Since the  $M_{\pi^0}$  mass distribution is sensitive to the  $K_L \rightarrow \pi^0\pi^0\pi^0$  background level, we fit this distribution with Monte Carlo using the default shower library for different regions of the shape  $\chi^2$  variable. We chose the following regions of shape  $\chi^2$ :  $0 < \text{shape } \chi^2 < 1.35$ ,  $1.35 < \text{shape } \chi^2 < 1.8$ ,  $1.8 < \text{shape } \chi^2 < 3.5$ , and  $\text{shape } \chi^2 > 3.5$ . Based upon the level of background determined from the  $M_{\pi^0}$  mass distribution,

we reweighted the default shower library Monte Carlo in each bin of shape  $\chi^2$ . The resulting shape  $\chi^2$  distribution from the default shower library was then compared to the distribution found using the data shower libraries.

Figure 5.4a shows the fusion  $\chi^2$  calculated using the data shower library and the re-weighted fusion  $\chi^2$  from the default shower library. As can be seen, both distributions exhibit a hump in the region around 1.2. Figure 5.4b shows the data shower library and the unweighted default shower library. There is a clear discrepancy between the two distributions, with the default shower library indicating a significantly smaller amount of background. Therefore, we have reason to trust the results from the data shower library. Unfortunately, this indicates that the background level is significantly higher than we would expect using the default shower library.

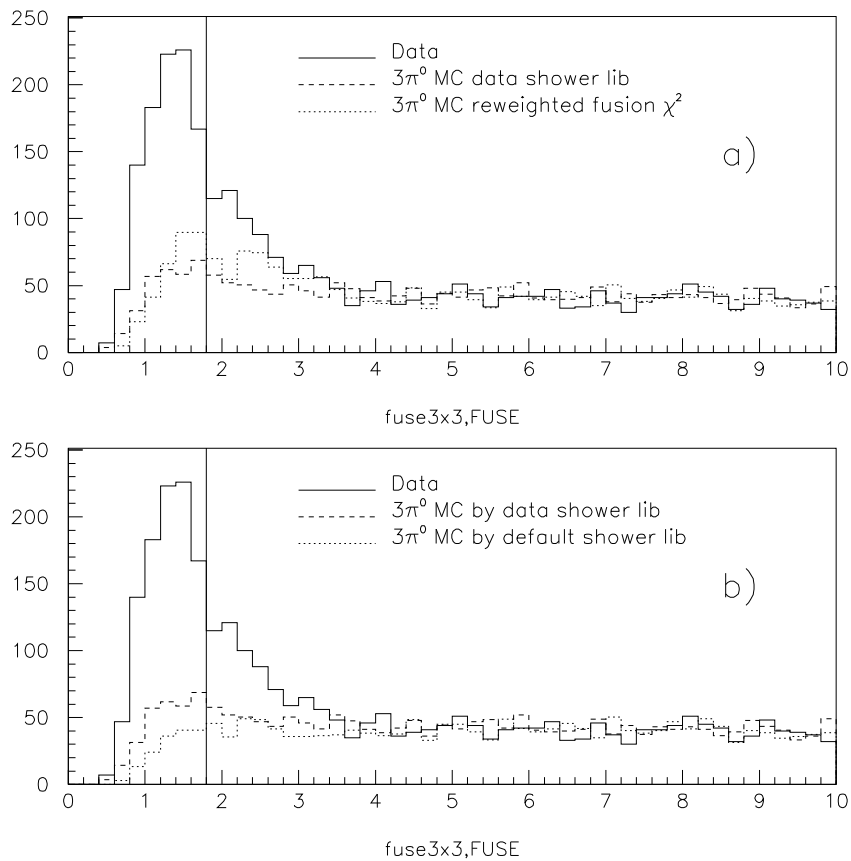


Figure 5.4: The shape  $\chi^2$  distribution. a) The solid histogram is the data, the dashed histogram is the  $K_L \rightarrow \pi^0\pi^0\pi^0$  Monte Carlo calculated using the data shower library, and the dotted histogram the  $K_L \rightarrow \pi^0\pi^0\pi^0$  Monte Carlo using the reweighted default shower library. b) The same histogram as above except that the dotted histogram is the  $K_L \rightarrow \pi^0\pi^0\pi^0$  Monte Carlo using the unweighted default shower library.

## CHAPTER 6

### BRANCHING RATIO RESULT AND $a_V$ FIT

We are now ready to determine the branching ratio for  $K_L \rightarrow \pi^0 \gamma \gamma$ . The value of the branching ratio is an important test of ChPT. In addition we can use the two Dalitz variables,  $Y_{Dalitz}$  and  $Z_{Dalitz}$  to fit for  $a_V$ . As discussed in chapter 1, the value of  $a_V$  can be used to estimate the CP conserving contribution to  $K_L \rightarrow \pi^0 e^+ e^-$ .

#### 6.1 $K_L \rightarrow \pi^0 \gamma \gamma$ branching ratio

After all cuts 1982  $K_L \rightarrow \pi^0 \gamma \gamma$  candidates remain. The  $3\pi^0$  background is estimated to be 601, and 919332  $2\pi^0$  normalization mode events survive all cuts. The branching ratio for  $K_L \rightarrow \pi^0 \gamma \gamma$  can be determined from the following equation.

$$\text{BR}(K_L \rightarrow \pi^0 \gamma \gamma) = \text{BR}(K_L \rightarrow \pi^0 \pi^0) \times \text{BR}(\pi^0 \rightarrow \gamma \gamma) \times \frac{N_{\pi^0 \gamma \gamma} - N_{bkg}}{N_{2\pi^0}} \times \frac{\epsilon_{2\pi^0}}{\epsilon_{\pi^0 \gamma \gamma}}. \quad (6.1)$$

Here  $N_{\pi^0 \gamma \gamma}$  is the number of candidate events before subtraction,  $N_{bkg}$  is the total number of background events estimated from Monte Carlo simulation, and  $N_{2\pi^0}$  is the number of reconstructed  $K_L \rightarrow \pi^0 \pi^0$  events.  $\epsilon_{\pi^0 \gamma \gamma}$  is the  $K_L \rightarrow \pi^0 \gamma \gamma$  acceptance and  $\epsilon_{2\pi^0}$  is the  $K_L \rightarrow \pi^0 \pi^0$  acceptance. To calculate the signal or the normalization mode acceptance, we generate MC with a fixed Z decay range and the fixed momentum range, the number of events after all cuts divided by the generated  $K_L$  is the acceptance. The acceptances and other numbers used to calculate the  $K_L \rightarrow \pi^0 \gamma \gamma$

	1996-1997	1999	Total
# Signal Events	989	993	1982
# Norm Events	482027	437305	919332
Signal Acceptance	0.03302	0.02613	0.02957
Norm Acceptance	0.03278	0.02573	0.02925
$K_L \rightarrow 3\pi^0$ Bkg	313	288	601
$K_L \rightarrow 2\pi^0$ Bkg	5.4	1.2	6.6

Table 6.1: Values used in branching ratio calculation

branching ratio are shown in Table 6.1. For 97 MC, the signal and normalization mode acceptance are 0.03302 and 0.03278 respectively, while for 99 MC, the signal and normalization mode acceptance are 0.02613 and 0.02573 respectively. To calculate the combined acceptance, the final number of events is weighted by the  $2\pi^0$  number divided by the same weight of the generated  $K_L$ . In the table 6.1, we can see the acceptance of normalization mode is close to that of the signal, that's why we use  $2\pi^0$  to determine the cut position.

The branching ratios for  $K_L \rightarrow \pi^0\pi^0$  is  $(8.89 \pm 0.04) \times 10^{-4}$ , while the  $\pi^0 \rightarrow \gamma\gamma$  branching ratio is  $(98.798 \pm 0.032)\%$  [22]. Using equation 6.1, we calculate the  $K_L \rightarrow \pi^0\gamma\gamma$  branching ratio to be:

$$\text{BR}(K_L \rightarrow \pi^0\gamma\gamma) = (1.29 \pm 0.03(\text{stat})) \times 10^{-6}$$

We calculate the branching ratio by relative normalization.

## 6.2 Estimate of the systematic uncertainties on the branching ratio

The number quoted above only includes the statistical uncertainty due to the number of reconstructed candidate events. There are many sources of systematic effects

that can affect our result. In particular, three kinds of systematic error contribute to the uncertainty: the acceptance error, the background estimation, and non-experimental effects such as theory or the  $K_L \rightarrow \pi^0\pi^0$  and  $\pi^0 \rightarrow \gamma\gamma$  branching ratios.

In the branching ratio calculation, only two numbers come directly from the data, the number of normalization mode  $2\pi^0$  events, and the number of the  $\pi^0\gamma\gamma$  candidates. The background level and the acceptance ratio of  $2\pi^0$  to  $\pi^0\gamma\gamma$  are calculated using our Monte Carlo. We would like to check both the ratio of acceptances used in our calculation and the sensitivity of the background estimate to our selection criteria. Because the  $K_L \rightarrow \pi^0\gamma\gamma$  and  $K_L \rightarrow \pi^0\pi^0$  events have a similar topology, we would expect that many effects will cancel in the ratio of acceptances. We expect that any discrepancies between the Monte Carlo and the data will have similar effects on both the signal and normalization mode. So, in the ratio, the discrepancy will tend to cancel. For example, we do not expect that the shape  $\chi^2$  cut will adversely affect one mode over the other. We first will study the systematic uncertainties in the acceptance ratio by examining the effects of the selection criteria.

### 6.2.1 Reweighting to study the systematic errors

One method for checking the effects of the selection criteria on the result is to look at the change in the final result as a function of the cuts. The drawback of this method is that the changes are subject to statistical fluctuations. To remove the statistical effects, we decided to reweight the Monte Carlo to match the data. Since we used the same Monte Carlo and data samples, the changes in the result before

and after the reweighting could be attributed to mismatches in the data/Monte Carlo agreement. We took the change in the branching ratio after reweighting as the systematic error. This reweighting method is sensitive to both the acceptance ratio and the background level. If we reweight the  $K_L \rightarrow \pi^0\pi^0$  events and the signal Monte Carlo, then we can check the acceptance ratio. If we reweight the  $K_L \rightarrow \pi^0\pi^0\pi^0$  Monte Carlo, then we can check the background level estimate.

In checking the systematic errors, we needed to ensure that the data sample that we compared to consisted mainly of a single type of event. For the  $K_L \rightarrow \pi^0\pi^0$  and  $K_L \rightarrow \pi^0\pi^0\pi^0$  samples, we were able to isolate samples with 95% purity. While all selection criteria could, in principle, contribute to a systematic effect, we determined that only cuts that had a significant impact on the signal (and normalization) acceptance could have a large impact on the systematic effects. So, we mainly checked the reweighting for cuts where the acceptance was below 90%. The variables selected to be reweighted are listed in the Table 6.2

Table 6.2: List the variables of which the cut acceptance is below 90%

Variable	Acceptance before fusion $\chi^2$	Acceptance after fusion $\chi^2$
NHIT	72.2%	71.3%
EK	93.2%	94.6%
ZDK	38.5%	41.2%
EMA	80%	51.3%
ECA	93.4%	78.9%
ERC	82%	40.7%
EBA	91.2%	77.8%

### 6.2.2 The kaon energy

Even though the kaon acceptance is above 90%, many other variables such the decay vertex, the  $\pi^0$  mass, the  $\gamma\gamma$  invariant mass are related to this variable. So, we decided to also check the dependence of the result on the kaon energy. From the  $K_L \rightarrow 2\pi^0$  kaon energy data Monte Carlo overlay, the Monte Carlo matches the data. But for  $K_L \rightarrow 3\pi^0$ , we are very sensitive to how well the Monte Carlo models the effects of both missing energy and fused photons. These effects can change the relative levels of single and double fusion backgrounds.

Before applying the shape  $\chi^2$  cut, the kaon energy of  $K_L \rightarrow 3\pi^0$  Monte Carlo events was reweighted to match the data. Figure 6.1 shows the Monte Carlo kaon energy compared to data. The upper plots are before reweighting. After reweighting, the  $3\pi^0$  acceptance changed by 2.29%. Multiplying this by the background level of 30%, we find a change of 0.69% in the branching ratio, and this is assigned as the kaon energy uncertainty.

### 6.2.3 Vertex position

Since the  $K_L \rightarrow \pi^0\pi^0\pi^0$  acceptance depends strongly on the decay vertex cut, we needed to check the effects of the Monte Carlo simulation of this variable. Recall that the vertex is determined solely by the photon energies and positions in the CsI calorimeter. So, to a large degree, this systematic check is a check of the energy calibration. The vertex of the single fusion events rises quickly as the  $Z$  vertex increases, while the double fusion vertex distribution is similar to that of  $K_L \rightarrow \pi^0\gamma\gamma$  and  $K_L \rightarrow 2\pi^0$  vertex. To reduce the error caused by  $\pi^0\gamma\gamma$  contamination, the

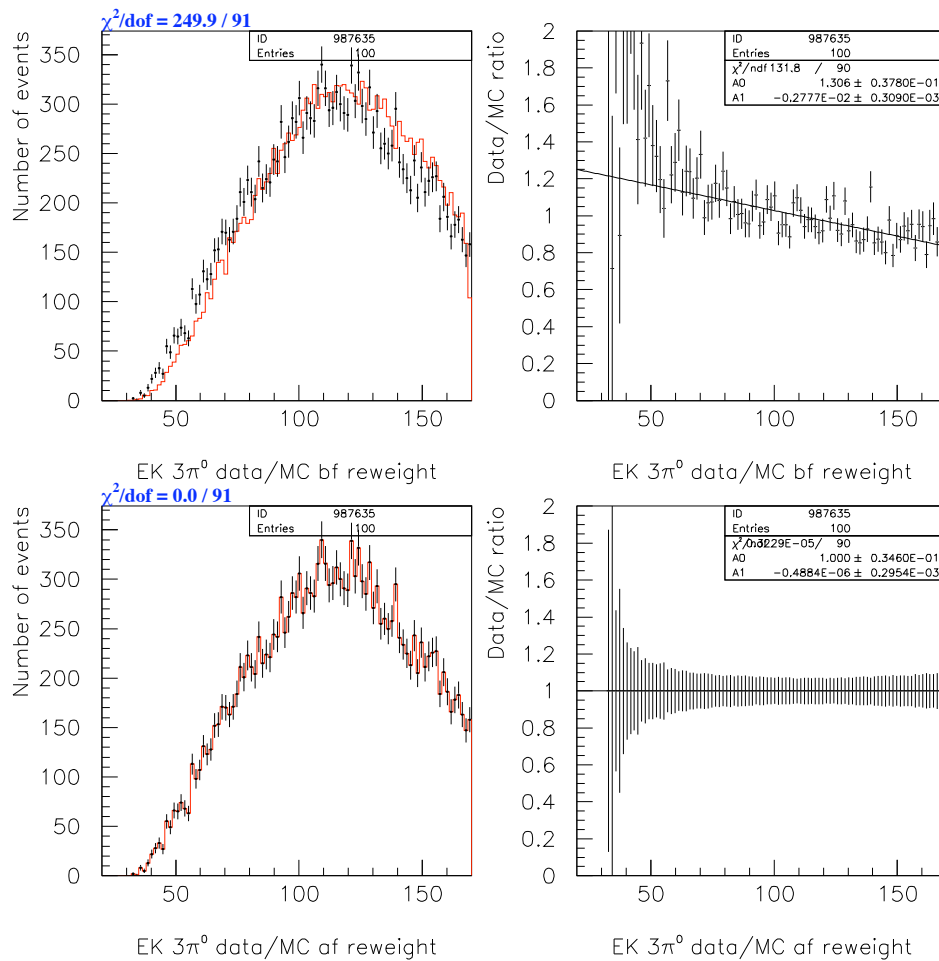


Figure 6.1: The reweighted kaon energy compared to data. The upper plots are not reweighted, after the variable is reweighted to data, the acceptance difference is calculated and counted as the systematic error.

reweighting is done before the shape  $\chi^2$  cut where the  $\pi^0\gamma\gamma$  level is about 2-5%. The  $Z$  decay vertex for  $K_L \rightarrow \pi^0\pi^0\pi^0$  Monte Carlo and the data is shown in Figure 6.2. After this variable is reweighted, and after applying the shape  $\chi^2$  cut, the acceptance difference changes by 1.27%. Scaled by the  $K_L \rightarrow 3\pi^0$  level background level, the difference is 0.38%. This is taken as the systematic error.

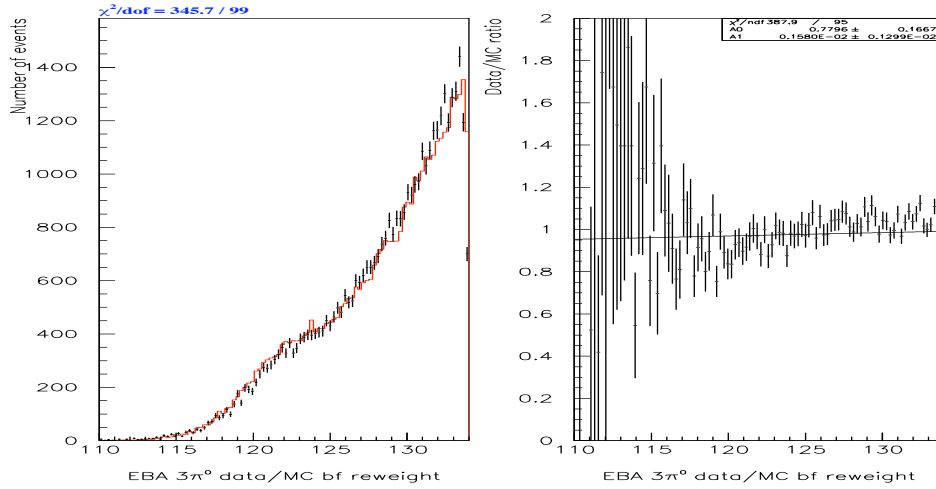


Figure 6.2: The unweighted  $Z$  decay vertex compared to data. After the variable is reweighted to data, the acceptance difference is calculated and counted as the systematic error.

#### 6.2.4 Photon veto cut

The photon vetoes are crucial in reducing the  $K_L \rightarrow \pi^0\pi^0\pi^0$  background. We cut on the total energy in the photon vetoes and use our reweighting method to check the effect of the energy simulation. Before the shape  $\chi^2$  variable cut, the  $K_L \rightarrow 3\pi^0$  Monte Carlo is reweighted to match the data, then we applied the fusion shape  $\chi^2$  cut. Figure 6.3 and Figure 6.4 show the EMA (Mask Anti) and ERC (Ring counter) data/MC overlay. The variables are not reweighted in these plots. After

the variable is reweighted to match the data, the acceptance difference is calculated and taken as the systematic error. The ring counter contributes the systematic error of 0.46%, and back anti contributes 0.31%, mask anti cuts introduces 0.69%. The collar anti has a relatively small systematic error of 0.15%.

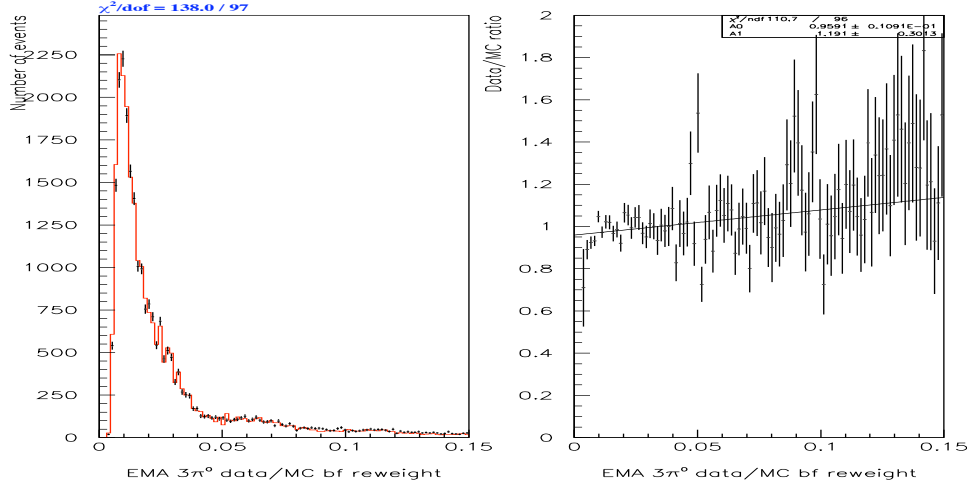


Figure 6.3: The variable EMA of Monte Carlo compared to data. The variable is not reweighted, after the variable is reweighted to data, the acceptance difference is calculated and counted as the systematic error.

### 6.2.5 The drift chamber in-time hits (NHIT)

Figure 6.5 shows the drift chamber in-time hit Data/MC overlay for  $K_L \rightarrow 3\pi^0$  events. The  $K_L \rightarrow 3\pi^0$  Monte Carlo NHIT is reweighted bin by bin to match the data. We again applied fuse3x3 cut, and found the the acceptance difference to be 3.06%. This difference multiplied by the background level is 1.07%, which we take as the systematic uncertainty contributed by the variable NHIT.

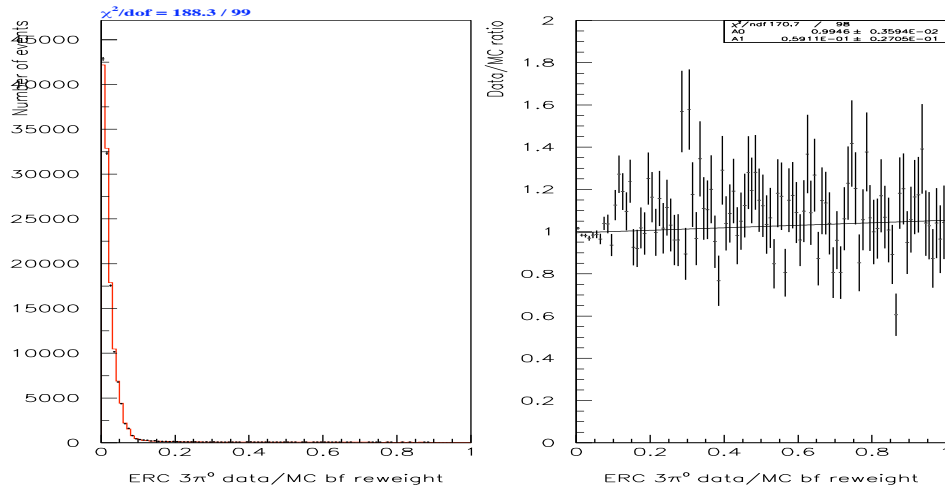


Figure 6.4: The comparison of ERC data to MC. The ERC includes ERC6, ERC7, ERC8, ERC9, and ERC10. The variable is not reweighted, after the variable is reweighted to data, the acceptance difference is calculated and counted as the systematic error.

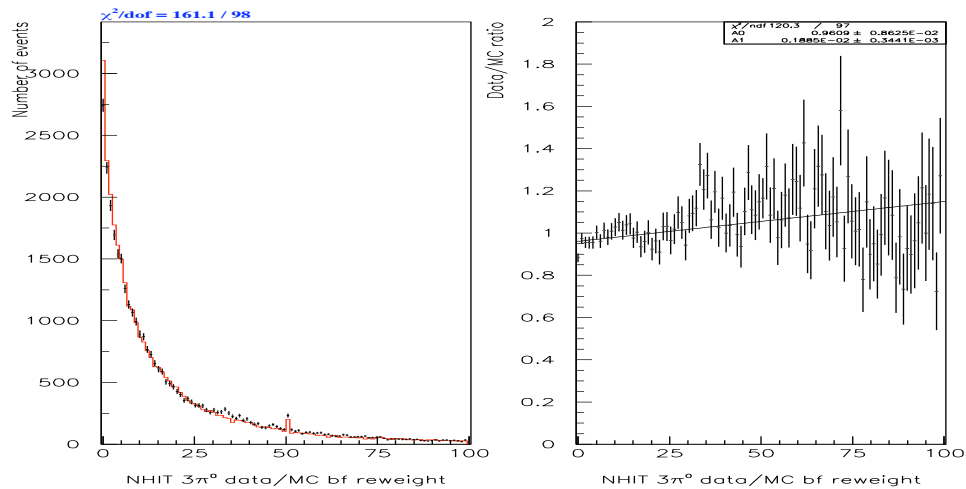


Figure 6.5: The comparison of the drift chamber in-time hit data to MC. The variable is not reweighted, after the variable is reweighted to data, the acceptance difference is calculated and counted as the systematic error.

### 6.2.6 Shape $\chi^2$

This variable is treated differently from the above variables. In the region of small shape  $\chi^2$ , the data is dominated by signal events. However, it is in this region that we need to know the shape  $\chi^2$  very well. Since we cannot isolate a good sample of  $K_L \rightarrow \pi^0\pi^0\pi^0$  events with low shape  $\chi^2$ , we added Monte Carlo samples of  $K_L \rightarrow \pi^0\pi^0\pi^0$  and  $K_L \rightarrow \pi^0\gamma\gamma$  together, and then weighted the background sample so that the combined signal plus background Monte Carlo matched the data. We determined the ratio of  $K_L \rightarrow \pi^0\gamma\gamma$  and  $K_L \rightarrow 3\pi^0$  from our fit of the  $M_{\pi^0}$  distribution. The Figure 6.6 shows the shape  $\chi^2$  distributions both before and after the reweighting process. After the variable is reweighted to data, the acceptance difference is calculated and counted as the systematic error. We find the difference in the  $K_L \rightarrow 3\pi^0$  acceptance is 3.57%. The effect on the branching ratio from the shape  $\chi^2$  variable is taken to be 1.07%.

The shape  $\chi^2$  cut also affects the ratio of single to double fusion events. Since this ratio can be affected by many subtle effects in the simulation, we varied this ratio in our Monte Carlo to better match the  $M_{\gamma\gamma}$  distribution. The difference between the default Monte Carlo and this reweighted Monte Carlo was also taken as a systematic error. The systematic error is calculated by background level times the difference in percent. The lower the background level, the smaller the systematic error contributed by background.

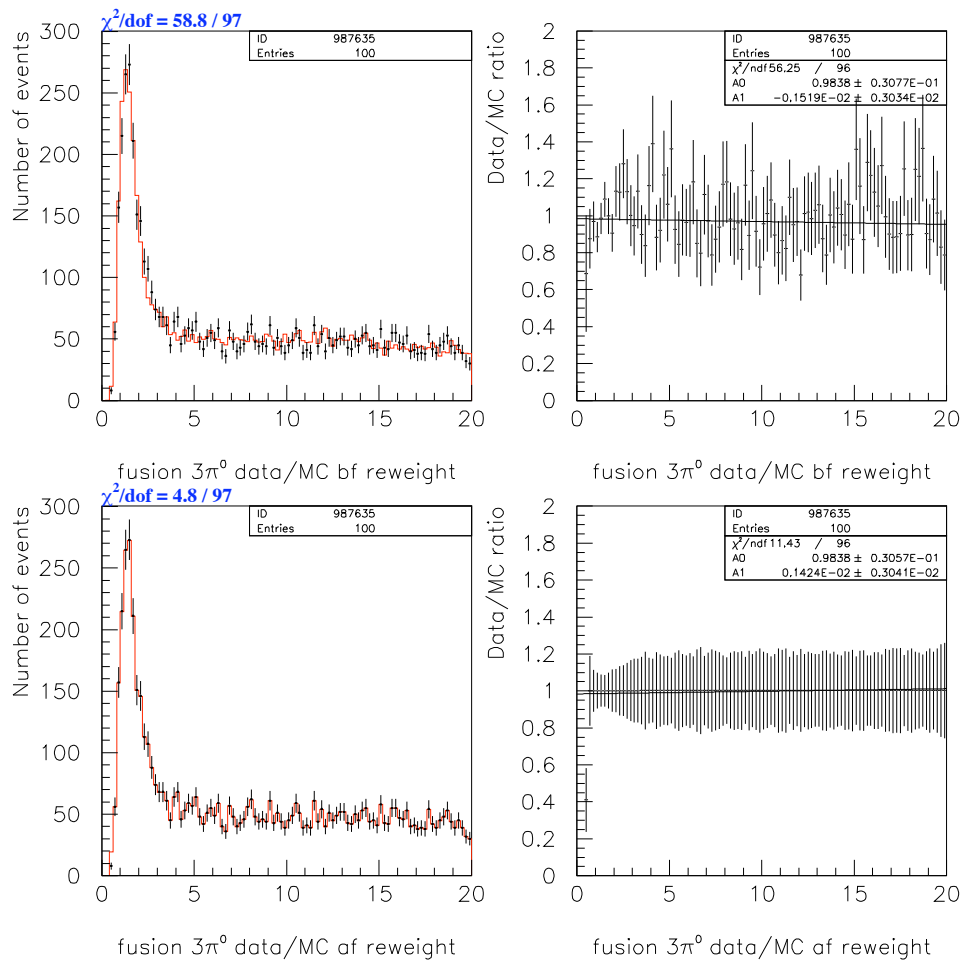


Figure 6.6: The reweighted fusion shape  $\chi^2$  compared to data. The upper plots are not reweighted, after the variable is reweighted to data, the acceptance difference is calculated and counted as the systematic error.

### 6.2.7 Error from estimation of background

The previous sections dealt mainly with understanding how well the Monte Carlo simulated the reconstructed variables. We also need to determine how well we understand the normalization between the  $K_L \rightarrow \pi^0\pi^0$  and the  $K_L \rightarrow \pi^0\pi^0\pi^0$  samples. This normalization helps to set the scale of the background from the  $K_L \rightarrow \pi^0\pi^0\pi^0$  events. This is also the largest source of systematic uncertainty.

We have several methods to estimate the  $K_L \rightarrow 3\pi^0$  level: relative normalization, absolute normalization, and combination of these methods. Each method is only sensitive to some part of the background so we take the difference between the various methods as our systematic uncertainty.

### 6.2.8 Relative normalization using the shape $\chi^2$

The shape  $\chi^2$  distribution can be used to determine the relative normalization. For values of the shape  $\chi^2$  distribution in the range of 5-20, most events are from  $K_L \rightarrow 3\pi^0$  events. By comparing the event number of data with the event of  $3\pi^0$  Monte Carlo, we can estimate background level. This method requires that the Monte Carlo describes fusion shape  $\chi^2$  variable well in this region. Figure 6.7 shows the  $K_L \rightarrow 3\pi^0$  Monte Carlo for single fusion and double fusion events, separately. In the region of shape  $\chi^2$  between 5-20, the number of the double fusion events is 6.5 times as high as the number of the single fusion. But in the low shape  $\chi^2$  region (0-2.0), the number of the single fusion events is comparable to that of the double fusion events. Figure 6.8 shows comparison of the data and Monte Carlo shape  $\chi^2$  distribution after normalizing the  $K_L \rightarrow \pi^0\pi^0\pi^0$  in the high shape  $\chi^2$  region. We

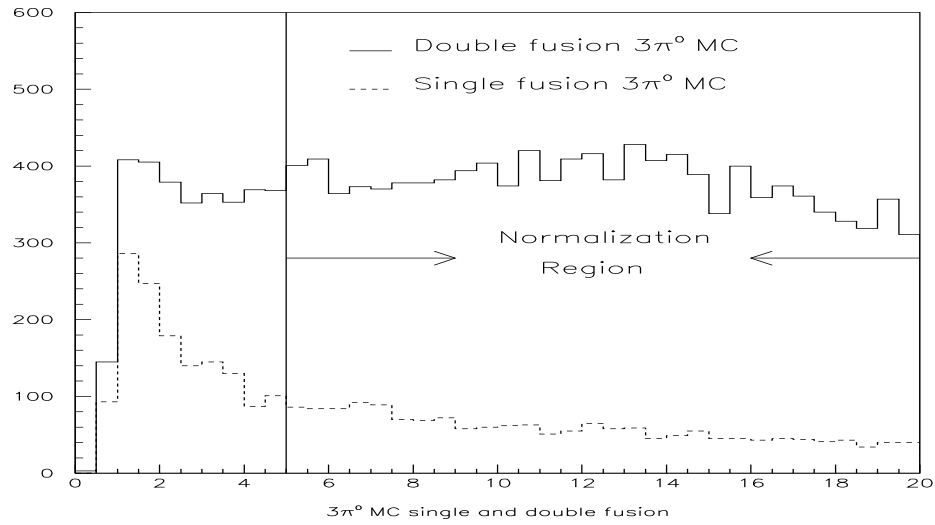


Figure 6.7: This plot shows the  $3\pi^0$  single fusion and double fusion fusion  $\chi^2$  separately. In the range of 5-20 which is marked as normalization region, the number of the double fusion 6.5 times as much as the number of the single fusion. But in the low value region (0-2.0), the number of the single fusion is comparable to that of the double fusion.

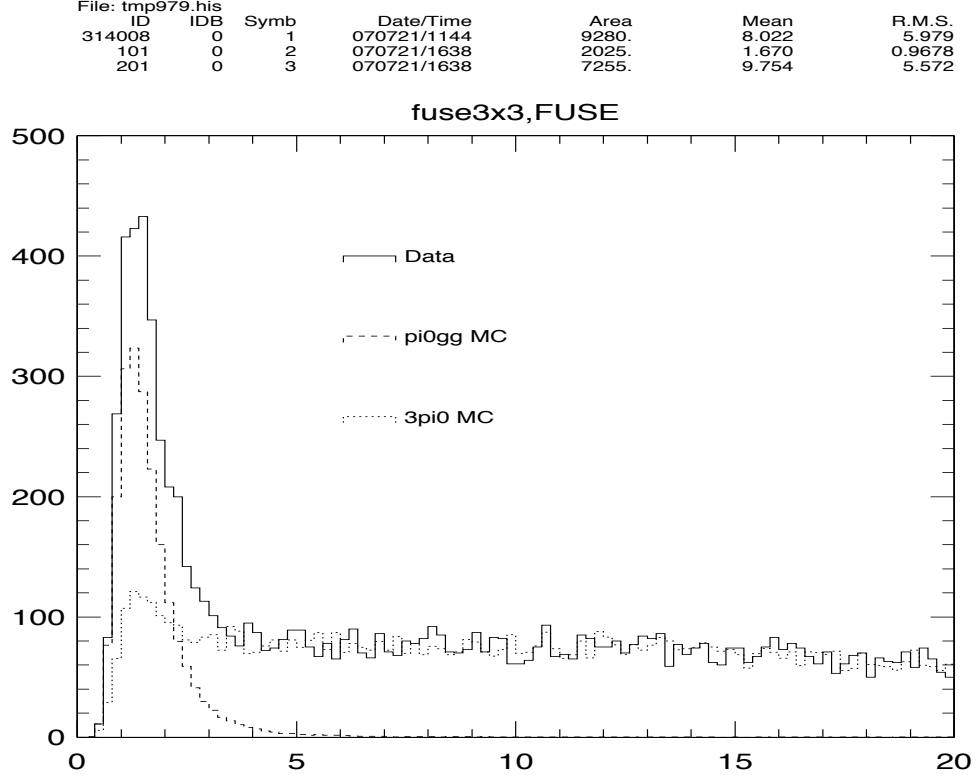


Figure 6.8: The explanation of the relative normalization method. In fusion shape  $\chi^2$  distribution, within the range of 5-20 are mostly  $3\pi^0$  events. The uncertainty of this method is that the proportion of the single fusion and the double fusion may be different in data, and most of  $3\pi^0$  fusion  $\chi^2$  in the range of 5-20 are double fusion.

find the normalization scale to be 0.4434.

### 6.2.9 Absolute normalization

The normalization mode  $K_L \rightarrow \pi^0\pi^0$  is used to estimate the  $K_L$  flux. The background level from the  $K_L \rightarrow \pi^0\pi^0\pi^0$  Monte Carlo is determined by scaling by the ratio of generated fluxes and the ratio of the  $K_L \rightarrow \pi^0\pi^0\pi^0$  and  $K_L \rightarrow \pi^0\pi^0$  branching ratios. This normalization method depends on the acceptance ratio of  $K_L \rightarrow 2\pi^0$  to  $K_L \rightarrow 3\pi^0$ . Using this method we find the normalization scale to be

0.4300. We take the difference 3%, scaled by the background 30%, which is 0.9% as the normalization systematic error.

### 6.2.10 Second relative normalization check

This method can best be described using Figure 6.8. We perform a fit of the shape  $\chi^2$  over the range of 0-20. This fit is done after all cuts but before the shape  $\chi^2$  cut. We float the ratio of  $K_L \rightarrow 3\pi^0$  Monte Carlo and  $K_L \rightarrow \pi^0\gamma\gamma$ , letting the fitter determine the ratio. This assumes that the Monte Carlo describes the shape  $\chi^2$  well which seems reasonable based upon Figure 5.3. After applying the shape  $\chi^2$  at 1.8, we calculate the branching ratio difference, which is 0.9%. But we do not count this as the extra systematic error, but use it to check the relative and absolute normalization.

### 6.2.11 Using the $M_{\pi^0}$ to check our methods

By fitting the  $\pi^0$  mass distribution, we can estimate  $3\pi^0$  level after all cuts. The advantage of this method is uses a different variable than the shape  $\chi^2$  distribution as is used in the previous method. However, it has one drawback in that it cannot be used to easily distinguish between single and double fusion events. While the single and double fusion events produce very different distributions in the  $\pi^0$  mass, the distribution for the signal events,  $K_L \rightarrow \pi^0\gamma\gamma$ , and the double fusion events is very similar. On the other hand, the single fusion events have a flat  $M_{\pi^0}$  distribution, while  $\pi^0\gamma\gamma$  has a very thin tail in  $M_{\pi^0}$  distribution, that makes  $3\pi^0$  single fusion events easily measured. So the number of  $3\pi^0$  double fusion events is fixed to the single fusion events in this method. We find the difference in the branching ratio

using this method differs from that found using the relative normalization by 0.9%. This method is only used as a reference to verify the error.

### 6.2.12 From $a_V$

The Monte Carlo was generated with a specific value of  $a_V$ . The effects of this parameter changes the mass distribution  $M_{\gamma\gamma}$ . Since this mass is sensitive to both the opening angle of the two photons, as well as their energies, the value of  $a_V$  must have some effect on the signal acceptance. This will change the relative acceptance between  $K_L \rightarrow \pi^0\pi^0$  and  $K_L \rightarrow \pi^0\gamma\gamma$ , since the first mode does not depend upon  $a_V$ . In our Monte Carlo we utilized two different  $K_L \rightarrow \pi^0\gamma\gamma$  models. However, we found that both of these models produced the same  $a_V$  dependence and so we do not introduce a specific uncertainty based upon the models. To check the dependence upon the value of  $a_V$ , we generated large Monte Carlo samples with  $a_V$  in the range from -1.0 to -0.3. We found that the acceptance changes by about 6.9% in Figure 6.9.  $a_V$  measured by NA48 is  $-0.46 \pm 0.03 \pm 0.04$ . We only count the error caused by the  $a_v$  difference between NA48 and KTeV, which is 1.5% as the systematic error.

### 6.2.13 From the MC acceptance ratio

This item is Monte Carlo  $2\pi^0$  to  $\pi^0\gamma\gamma$  acceptance ratio. We vary the cuts to find the systematic error from the MC acceptance ratio. The kaon energy cut contributes 1 contributes 0.6%, so total error of the acceptance is 1.16%.

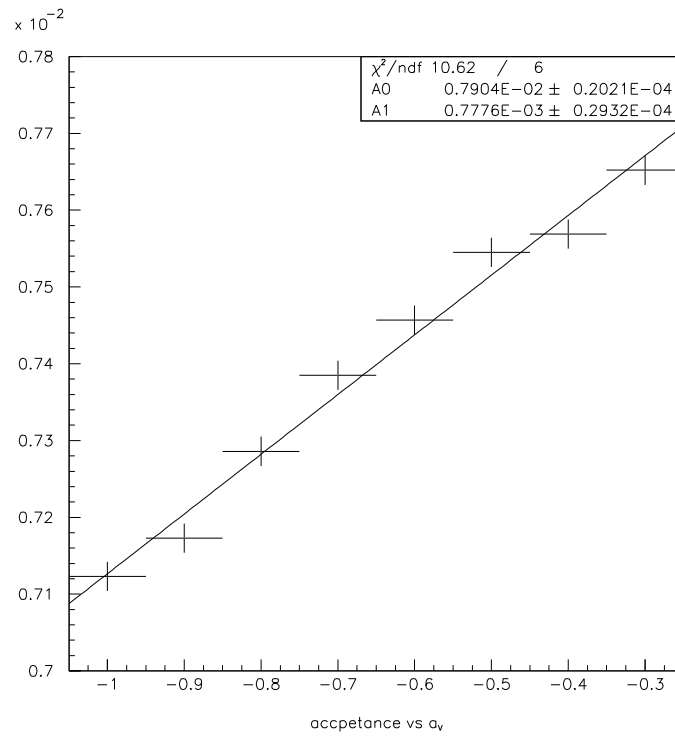


Figure 6.9: The ratio of the acceptance of  $2\pi^0$  and of  $\pi^0\gamma\gamma$  varies with  $a_V$

### 6.2.14 Summary

All of the systematic errors associated with the determination of the branching ratio are listed in Table 6.3. The largest error is due to the normalization of the  $K_L \rightarrow 3\pi^0$  background. Tightening the cuts might help to reduce the systematic error since the level of  $K_L \rightarrow \pi^0\pi^0\pi^0$  background would be reduced. However, this would lead to an increase in the statistical error. The total error is 3.0%, and corresponds to a systematic error in the branching ratio of  $0.02 \times 10^{-6}$ . Including the systematic uncertainties, we find  $\text{BR}(K_L \rightarrow \pi^0\gamma\gamma) (1.29 \pm 0.03(\text{stat}) \pm 0.04(\text{sys})) \times 10^{-6}$ .

Table 6.3: Branching ratio systematic uncertainties

Source of Uncertainty	Uncertainty (%)
FUSE3X3	1.07
Decay Vertex	0.38
Ring Counter	0.46
Back Anti 1	0.31
Mask Anti	0.69
Kaon Energy	0.69
Collar anti	0.15
Drift Chamber hit	0.92
$2\pi^0$ branching ratio	0.50
$3\pi^0$ background	1.30
MC statistics	1.0
Normalization	0.9
$a_V$ dependence	1.5
MC acceptance ratio	1.16
Total	3.0

### 6.3 Determination of $a_V$

We now turn to the determination of  $a_V$  from our data. To measure  $a_V$ , we fit the two-dimensional plot of  $M_{\gamma\gamma}$  and  $Y_{Dalitz}$  using the maximum log likelihood method. We define the log likelihood function  $L(a_V)$  as:

$$\log L(a_V) = \sum_{y, M_{\gamma\gamma}} [N(y, M_{\gamma\gamma}) \log MC(y, M_{\gamma\gamma}, a_V) - MC(y, M_{\gamma\gamma}, a_V)] \quad (6.2)$$

$N(y, M_{\gamma\gamma})$  is the number of events in the data in the  $y$  and  $M_{\gamma\gamma}$  bin of the 2D plot,  $y$  is the  $Y_{Dalitz}$  variable, and  $M_{\gamma\gamma}$  is the  $\gamma\gamma$  invariable mass,  $MC(y, M_{\gamma\gamma}, a_V)$  is the Monte Carlo prediction for the  $y$  and  $M_{\gamma\gamma}$  bin.  $MC$  is determined by the scaled  $K_L \rightarrow \pi^0 \gamma\gamma$  plus the  $K_L \rightarrow 3\pi^0$  Monte Carlo. To determine the most probable value for  $a_V$ , we generate several  $K_L \rightarrow \pi^0 \gamma\gamma$  MC sets with different values of  $a_V$ . We then calculate the log likelihood function, and plot the resulting values as a function of  $a_V$ . This distribution is fit to a curve and the point where the curve reaches a maximum is our fitted value for  $a_V$ . The errors on  $a_V$  are determined by the choosing the point where the log likelihood changes by 0.5

#### 6.3.1 Testing the fitter

To test the fitter, 140 samples of  $\pi^0 \gamma\gamma$  Monte Carlo with the same  $a_V$  are generated. Each sample is measured by the fitter to obtain  $a_V$  and the error. The error is calculated by

$$a_V err = \frac{(a_V(fit) - a_V(true))}{\sigma_{fit}} \quad (6.3)$$

The binning of the  $M_{\gamma\gamma}$  and  $Y_{Dalitz}$  variables have some effect on the distribution of fitted values and was investigated. Two points were tested:  $a_V = -0.31$  and  $a_V = -0.65$ . We chose these two points because  $a_V = -0.65$  is close to  $a_V$  of the 1999 KTeV

PRL paper, and  $a_V = -0.31$  is close to the recent results on  $a_V$ .

In Figure 6.10, one can see the results of our fitter tests at these points:  $a_V = -0.31$  and  $a_V = -0.65$ . The measured results for these two points are  $a_V = -0.30$  and  $a_V = -0.66$  respectively. The rms for each of these two distributions is consistent with one sigma. Based upon these results, we believe that the fitter can correctly determine the value of  $a_V$  from the  $M_{\gamma\gamma}$  and  $Y_{Dalitz}$  distributions.

### 6.3.2 Fitting $a_V$

We use the background level calculated in chapter 5, and generate  $a_V = -0.7, -0.6, -0.5, -0.4, -0.3, -0.2, -0.1$ . The fitter predicts the  $a_V = -0.278$ . Figure 6.13 shows the  $M_{\gamma\gamma}$  distribution for both data and Monte Carlo. We found that in the region of  $M_{\gamma\gamma} = 270 \text{ MeV}/c^2$ , there is a mismatch between the data and the Monte Carlo. Recall that in this region the double fusion events are dominant. We redid our fit after rescaling the single and double fusion background events. The single fusion events were doubled, while the double fusion events were halved. The total level of background remained the same, so the branching ratio result did not change. We found that  $a_V$  went up by 17% to  $a_V = -0.34$ . The result of this second fit is shown in Figure 6.15. The distribution of the data in Figure 6.15 is not symmetric, so a third-order polynomial is used in fitting instead of a second-order polynomial. If a second-order polynomial fit is used in the histogram,  $a_V = -0.32$ , the maximum shifts in the positive direction, about 7% higher than the true maximum point. The second-order polynomial fit is calculated using formula:

$$a_V = \frac{PAR(2)}{PAR(3) * 2}$$

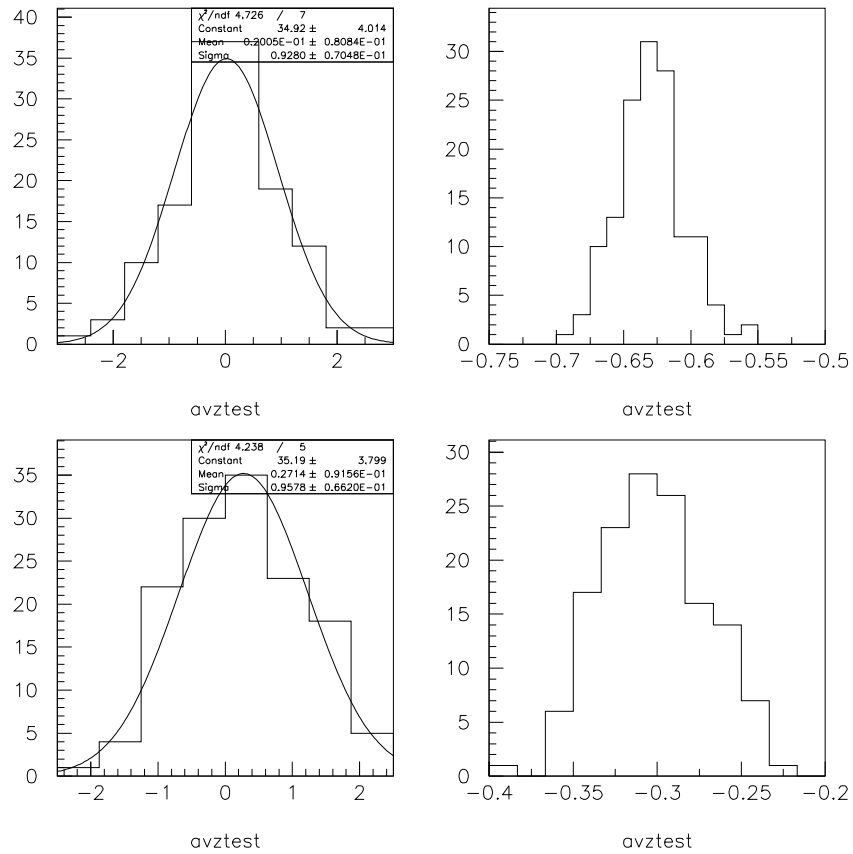


Figure 6.10: The difference between the fitted and true  $a_V$  divided by the true  $a_V$  (left) and the reconstructed  $a_V$  (right) for 142 Monte Carlo samples. The top plots are for  $a_V = -0.65$  and the bottom plots are for  $a_V = -0.31$ . The measured results are  $a_V = -0.302$  and  $a_V = -0.661$  respectively. The standard deviations are  $1\sigma$

. PAR(3) and PAR(2) are coefficients of the the second-order polynomial. The third-order polynomial is calculated using the formula:

$$a_V = \frac{-2 * PAR(3) - \sqrt{8 * PAR(3)^2 - 12 * PAR(4) * PAR(2)}}{6 * PAR(4)}$$

PAR(4), PAR(3), PAR(2) are coefficients of the third-order polynomial.

### 6.3.3 Systematic error study

The systematic effects that affect our fit for  $a_V$  only depend upon those things which can affect the shape of either the  $Z_{Dalitz}$  or  $Y_{Dalitz}$  distributions. So, many fewer of the selection criteria are important to the systematic studies of  $a_V$ . The cuts that can change either the shape of the  $\pi^0\gamma\gamma$  events or the  $K_L \rightarrow \pi^0\pi^0\pi^0$  events are listed below. We did not find that there was any significant effect from other selection criteria.

- Z vertex may affect the single fusion of  $3\pi^0$
- The photon veto cuts may affect the single fusion of  $3\pi^0$
- Fusion  $\chi^2$  variable may affect the double fusion of  $3\pi^0$  events.

We study the systematic error by cutting at several points around the nominal cut, and count the largest difference as the systematic error.

For the photon veto cuts, we varied all the photon veto cuts, ERC EBA, ECA, ECIA and refit for  $a_V$ . We measured  $a_V = -0.243 \pm 0.069$ . We attributed the systematic error from the photon veto cuts to be 12.6%.

Figure 6.11 shows the change in  $a_V$  as a function of the Z vertex. The nominal cut of the Z decay vertex is 128 m. When we varied the cut on Z from 126 m to 132 m, the largest difference in the extracted  $a_V$  was 0.043, or 15.5%. So, we take 15.5% as the systematic error from the Z vertex.

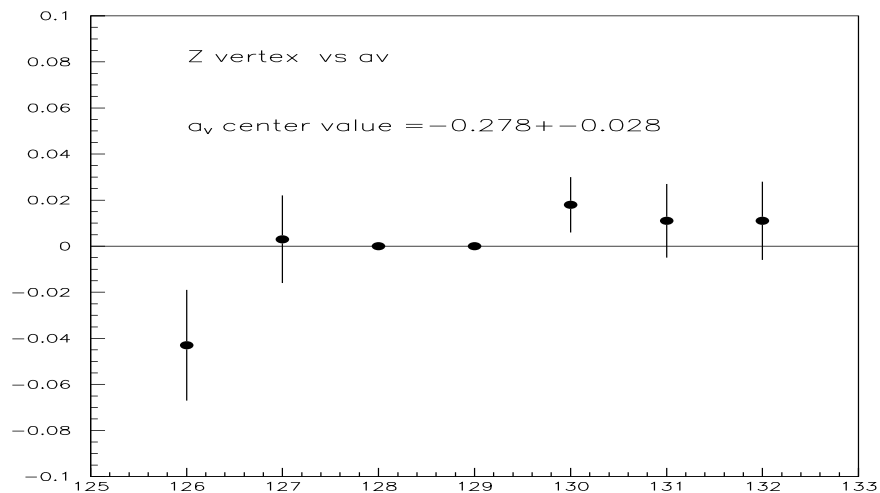


Figure 6.11:  $a_V$  systematic study on the Z decay vertex

Figure 6.12 shows the  $a_V$  systematic error study on the variation of the fusion shape  $\chi^2$ . The shape  $\chi^2$  is cut at 1.8. We varied the shape  $\chi^2$  cut from 1.6 to 2.6, the largest difference in  $a_V$  is 0.01, so we use 3.6% as the systematic error from the shape  $\chi^2$  cut.

The background level can affect the determination of  $a_V$  because the background

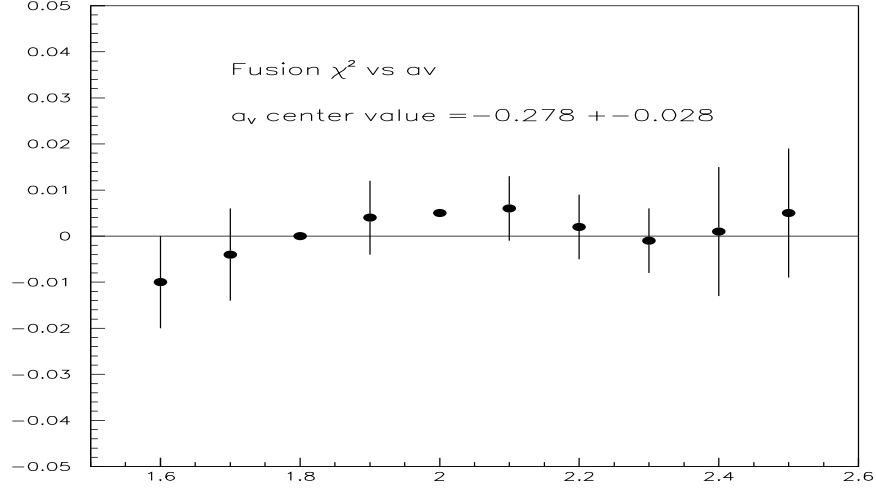


Figure 6.12:  $a_V$  systematic study on fusion  $\chi^2$

can affect the shape of the low mass  $M_{\gamma\gamma}$  tails. The vector exchange parameter effects the  $M_{\gamma\gamma}$  distribution quite a bit. To estimate the effects of the background level, we rescaled the background level by  $\pm 20\%$ , and refit for  $a_V$ . This difference in the background level is consistent with our earlier studies. The difference from our nominal fit  $+0.02/-0.03$ , so we assign 6.9% as the systematic error due to the uncertainty of the background level.

The fitter using the unscaled  $3\pi^0$  background predicts  $a_V=-0.278$ , and the fitter using the rescaled single fusion and double fusion background predicts  $a_V=-0.34$ . We assign the average of these two measurements as the result  $a_V=-0.31$ , and assign the half the difference 8.5% as the systematic error from these two.

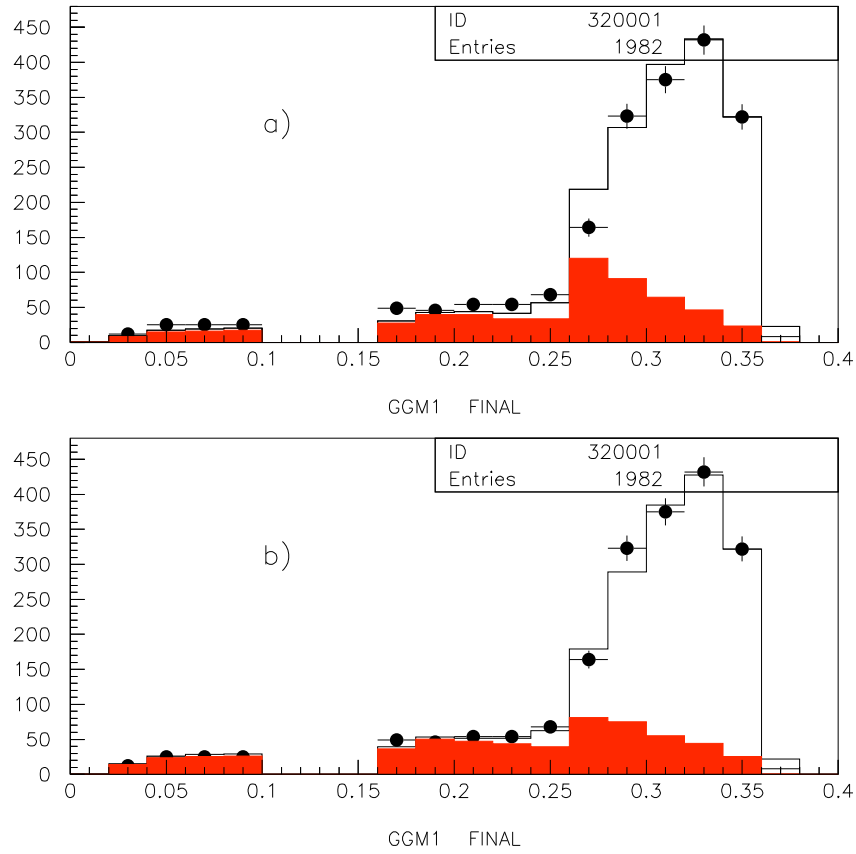


Figure 6.13:  $M_{\gamma\gamma}$  data MC overlay. The dot is DATA, the blank histogram is MC  $3\pi^0$  and  $\pi^0\gamma\gamma$ , the red histogram is  $3\pi^0$  background. a) Using default  $3\pi^0$  MC b) separate single and double fusion

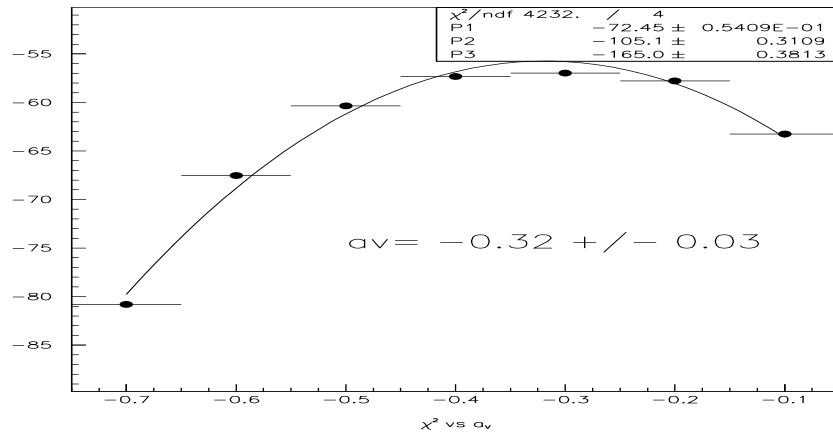


Figure 6.14: Using the background from Figure 6.13, a second-order polynomial fit provides  $a_V = -0.32$

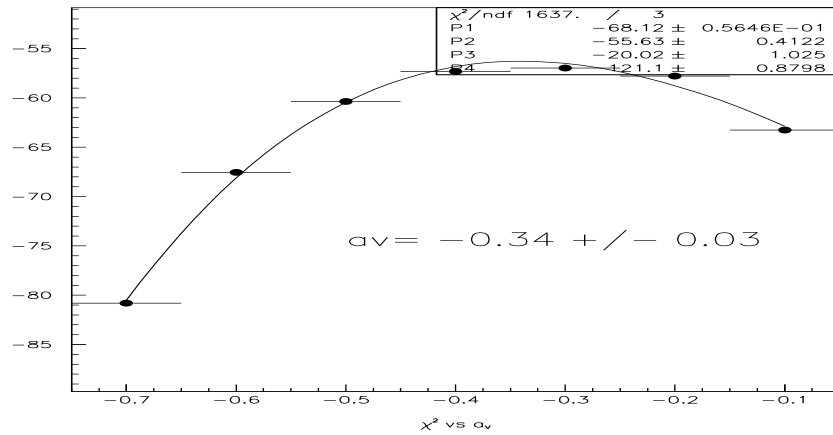


Figure 6.15: Using the background from Figure 6.13, a third-order polynomial fit provides  $a_V = -0.34$

In the Table 6.4, we show all of the systematic errors associated with the determination of  $a_V$ . The biggest error is caused by the variation of the single fusion and double fusion level which is 17%.

Table 6.4:  $a_V$  fitting systematic uncertainty

Source of the error	Error (%)
Photo veto cut	12.6
Z vertex cut	15.5
Fusion shape $\chi^2$	3.6
$3\pi^0$ background	10.9
Level uncertainty	6.9
Single and double fusion	8.5
Total	23.1

## 6.4 Summary

The major systematic uncertainties associated with this analysis result from uncertainty in the  $3\pi^0$  background. Some of these uncertainties are related to the simulation of the  $K_L \rightarrow 3\pi^0$  background, while others are due to the normalization of the background. The largest systematic is due to the uncertainty in simulating single and double fusion events. We find  $a_V$  to be:

$$a_V = (-0.31 \pm 0.05(stat) \pm 0.07(sys)). \quad (6.4)$$

## CHAPTER 7

### CONCLUSION

We analyzed our 1996, 1997 and 1999 data to measure the decay of  $K_L \longrightarrow \pi^0 \gamma \gamma$ . We have a better understanding of the main background  $K_L \longrightarrow \pi^0 \pi^0 \pi^0$  than the previous KTeV result[2]. We find the branching ratio for  $K_L \rightarrow \pi^0 \gamma \gamma$  to be

$$\text{BR}(K_L \rightarrow \pi^0 \gamma \gamma) = (1.29 \pm 0.03(\text{stat}) \pm 0.04(\text{sys})) \times 10^{-6}. \quad (7.1)$$

We also fit our data to extract the vector meson exchange parameter  $a_V$ . We measure

$$a_V = (-0.31 \pm 0.05(\text{stat}) \pm 0.07(\text{sys})). \quad (7.2)$$

Figure 7.1 shows these results compared to recent results from the NA48 experiment as well as the previous KTeV 1999 PRL result. The upper plot is the branching ratio of  $K_L \longrightarrow \pi^0 \gamma \gamma$ , and the lower plot is the measurement of  $a_V$ . In the branching ratio comparison plot, all the branching ratios are rescaled by the new  $K_L \rightarrow \pi^0 \pi^0$  branching ratio. In 1999  $K_L \rightarrow \pi^0 \pi^0$  branching ratio was  $(9.36 \pm 0.20) \times 10^{-4}$  [23], and in 2002, the it was  $(9.27 \pm 0.19) \times 10^{-4}$  [24]. So KTeV 99 PRL result is scaled to  $(1.56 \pm 0.06 \pm 0.07) \times 10^{-4}$ , while NA48 result is scaled to  $(1.27 \pm 0.03 \pm 0.03 \pm 0.03) \times 10^{-4}$ .

This result is a significant improvement over the previous KTeV result, with an improved understanding of the errors and backgrounds.

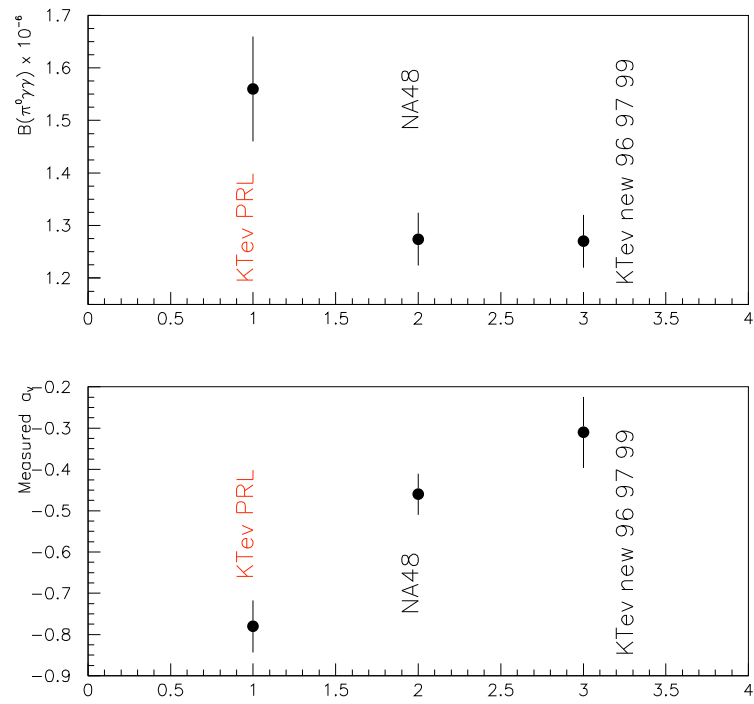


Figure 7.1: Comparison of results with KTeV 99 PRL and NA48 a) branching ratio and b) measured  $a_V$

The measure branching ratio confirms the ChPT prediction, and the ChPT + VMD confirms the  $M_{\gamma\gamma}$  distribution. Based on the measurement of  $a_V$ ,  $K_L \rightarrow \pi^0 e^+ e^-$  CP conserving contribution is [3] [5] [6] [7]:

$$K_L \rightarrow \pi^0 e^+ e^-|_{CP-conserving} = 2.14 \times 10^{-14}$$

which implies the direct CP violation dominates the decay  $K_L \rightarrow \pi^0 e^+ e^-$ .

## REFERENCES

- [1] J.H.Christenson, J.W.Cronin, V.L.Fitch, and R.Turlay, Phys. Rev. Lett. 13 (1964)138
- [2] A. Alavi-Harati et al., Phys. Rev. Lett 83, 917 (1999)
- [3] G. Ecker et al., Phys. Lett. B237 (1990) 481.
- [4] L. Cappiello et al, Phys. Lett. B298 (1993) 423
- [5] G. Ecker et al., Phys. Lett. B189 (1987) 363
- [6] J. Kambor et al, Phys. Rev. D49 (1994) 2346
- [7] A.G.Cohen G Ecker, et al, Phys. Lett. B304 (1993)347
- [8] G. D'Ambrosio and J. Portoles, *Nucl. Phys.*, **B492** (1997) 417.
- [9] J. F. Donoghue and F. Gabbiani, *Phys. Rev.*, **D56** (1997) 1605.
- [10] E731 Collab., V. Papadimitriou et al., Phys. Rev. Lett.63 (1989) 28
- [11] NA31 Collab., G.D. Barr et al., Phys. Lett. B242(1990) 523
- [12] E731 Collab., V. Papadimitriou et al., Phys. Rev. D44 (1991) R573
- [13] NA31 Collab., G.D. Barr et al., Phys. Lett. B284(1992) 440
- [14] NA48 A. Lai et al., Phys.Lett.B536 (2002)229

- [15] P.Heiliger, L.M Sehgal, Phys. Rev. D47, 4920(1993)
- [16] F..Gabbianni,G.Valencia Phys. Rev D64 094008(2001)
- [17] F.Gabbianni,G.Valencia Phys. Rev D66 074006(2002)
- [18] G.Buchalla, G.D'Abrosio, G.Isidori,Nucl. Phys. B672 387(2003)
- [19] S. Bright (1996, March). KTeV Internal Note#369.
- [20] Cheu, E., J. Hamm, and J. Wang (1999, February). KTeV Internal Note #606.
- [21] K.Arisaka,A.Barker et al.(1992) KTeV Design Report.Fermilab
- [22] W.-M. Yao et al., J. Phys. G 33, 1 (2006)
- [23] C. Caso et al, The European Physical Journal C3 (1998) 1
- [24] D.E. Groom et al., The European Physical Journal C15 (2000) 1
- [25] A. Alavi-Harati *et al.*, Phys. Rev **D67**, 012005 (2003).